Universität Bremen

Faculty 01: Physics / Electrical Engineering

Physics-based Data-driven Simulation of Debinding Failure and Sintering Deformation in Metal Binder Jetting

A Thesis by

M.Sc. Shahrooz Sadeghi Borujeni

Submitted in Partial Fulfillment of
the Requirements for the Degree of
Dr. rer. nat.

1. Gutachter:	Prof. Dr.-Ing. Vasily Ploshikhin
2. Gutachter:	Prof. Dr.-Ing. habil. Matthias Busse
Datum des Kolloquiums:	13. Februar 2024

Eigenständigkeitserklärung

Hiermit versichere ich, dass ich

1. die Arbeit ohne unerlaubte fremde Hilfe angefertigt habe,
2. keine anderen als die von mir angegeben Quellen und Hilfsmittel benutzt habe,
3. die, den benutzten Werken wörtlich oder inhaltlich entnommenen Stellen als solche kenntlich gemacht habe.

Unterschrift: Shahrooz Sadeghi Borujeni

Disclaimer

Die Ergebnisse, Meinungen und Schlüsse dieser Dissertation sind nicht notwendigerweise die der Volkswagen Aktiengesellschaft.

The results, opinions and conclusions expressed in this thesis are not necessarily those of Volkswagen Aktiengesellschaft.

The primary focus of the current thesis is on the development of numerical simulation for debinding failure and sintering deformation in metal binder jetting technology. Consequently, the experimental data are explained and interpreted to such an extent that they can be solely employed for observation, calibration, and validation.

Acknowledgments

I am profoundly grateful to Volkswagen AG for providing me with the invaluable opportunity to conduct this research as a Ph.D. candidate. I sincerely thank Ms. Ilnaz Emami for her support and motivation, encouraging me to embark on this journey.

For the exceptional guidance, supervision, and examination of my thesis, I am immensely thankful to Prof. Dr. -Ing. Vasily Ploshikhin. His invaluable insights and technical tips have been instrumental in shaping the quality of this work. I would also like to extend my appreciation to Prof. Dr. -Ing. habil. Matthias Busse, my examiner, for devoting his time and effort to reviewing my research.

A special appreciation goes to Dr. Anwar Shad, who patiently walked me through the metal binder jetting technology. Mr. Knut Schmidt deserves special recognition for his support throughout my research and his invaluable contributions to the corrections of my work. I am grateful to Dr. Frank von Lacroix for trusting and assisting me in completing my thesis. Additionally, I appreciate Mr. Daniel Fuchs for accompanying me during the writing sessions and providing companionship and encouragement.

I am genuinely grateful to my dear friend Mr. Yasin Bayzidi for his kind support during the challenging times I faced. Dr. Alexander Rütjes holds immense gratitude from me for his remarkable contributions to my academic and personal growth during this journey. He has played a vital role in expanding my knowledge, and his helpful feedback significantly enhanced the quality of my research.

Heartfelt thanks are extended to my parents, Mahin and Masoud, for their continuous support. Their love has served as the driving force behind my entire career.

Sadly, since the start of my thesis, numerous individuals in Iran have tragically lost their lives or been unjustly imprisoned simply for daring to pursue a life of liberty. I am deeply saddened that I cannot list all their names here. Despite the moments of doubt that brought me to the edge of giving up, I found solace in the realization that sharing these paragraphs with the academic and industrial community could potentially make a difference. Thus, with a mix of tears and frustration in one eye, and a gleam of hope for a more promising tomorrow in the other, I persevered, albeit slowly. This work is dedicated to the innocent passengers of flight PS752, whose lives were cut short before they could fully realize their dreams. It also serves as a tribute to the courageous women and young students in Iran who battle against superstition and oppression.

I am fortunate to have led a privileged life, been surrounded by a supportive family, received a proper education, and had exceptional friends and colleagues. Thanks to Volkswagen AG, I have been given the chance to begin my research and continue my career as an international employee. My greatest desire is to speak up for the millions of children and students in developing countries who have not been as fortunate as myself. I firmly believe that with the right opportunities and support, these individuals possess the potential to surpass my own achievements effortlessly. By increasing trust and allocating resources from the academic and industrial community, we can empower these young talents to significantly contribute to building a better world.

Contents

List of Acronyms

AM	Additive Manufacturing
CAD	Computer-Aided Design
CDF	Cumulative Distribution Function
CoG	Center of Gravity
CoV	Coefficient of Variation
DDNS	Data-Driven Numerical Simulation
DoE	Design of Experiments
DPC	Depowdering Protective Cage
DSC	Dynamic Scanning Calorimetry
EE	Elementary Effect
FE	Finite Element
FI	Failure Indicator
GPD	Green Part Density
GPP	Green Part Property
GPPF	Green Part Property Field
GS	Grain Size
ID	Inspection Dimension
IP	Inspection Point
IRD	Initial Relative Density
IT	International Tolerance
LFA	Laser Flash Analysis
LPBF	Laser Powder Bed Fusion
MA	Metallographic Analysis
MBJ	Metal Binder Jetting
MIM	Metal Injection Molding
MtV	Mass to Volume
PM	Powder Metallurgy
PoC	Proof of Concept
PSD	Powder Size Distribution
RD	Relative Density

RMS	Root Mean Square
RPS	Reference Point System
RT	Room Temperature
SAT	Sintering Activation Temperature
SEM	Scanning Electron Microscope
SHC	Specific Heat Capacity
SOVS	Skorohod Olevsky Viscous Sintering
SPD	Sintered Part Density
SS316L	Stainless Steel 316L
StD	Standard Deviation
TD	Thermal Diffusivity
TEC	Thermal Expansion Coefficient
TGA	Thermal Gravimetric Analysis
TOM	Thermo-Optical Measurement

Nomenclature

Greek Symbols

Symbol	Description	Units
α_d	thermal diffusivity	$\mathrm{m^2\,s^{-1}}$
α_{tec}	thermal expansion coefficient	$\mathrm{K^{-1}}$
β	material constant depending on surface energy for sinter stress	$\mathrm{N\,m^{-1}}$
$\dot{\delta}$	deflection rate of the arm in cross-shape and T-shape geometries	$\mathrm{m\,s^{-1}}$
$\dot{\epsilon}$	total strain rate	$\mathrm{s^{-1}}$
$\dot{\epsilon}_e$	elastic strain rate	$\mathrm{s^{-1}}$
$\dot{\epsilon}_{th}$	thermal strain rate	$\mathrm{s^{-1}}$
$\dot{\epsilon}_{vp}$	viscoplastic strain rate	$\mathrm{s^{-1}}$
ϵ_{cb}	shrinkage of the cylinders in diameter on the cross-shape geometry	%
ϵ_{ct}	shrinkage of the cylinders in height on the cross-shape geometry	%
η_0	apparent viscosity of a fully dense body	$\mathrm{N\,m^{-2}\,s}$
η_b	bulk viscosity	$\mathrm{N\,m^{-2}\,s}$
η_s	shear viscosity	$\mathrm{N\,m^{-2}\,s}$
γ_s	surface tension of powder	$\mathrm{J\,m^{-2}}$
κ_η	pre-exponential factor for apparent viscosity	$\mathrm{N\,m^{-2}\,s}$
λ_{os}	offset variable for sinter stress	-
λ_{ov}	offset variable for viscosity	-
$\omega_0, \omega_1, \omega_2$	transformations of parameters in the Weibull model	-
ϕ	element-wise importance factor	$\mathrm{m^3}$
ψ	failure indicator	-
Ψ_ρ	exponential factor for density in sinter stress	-
Ψ_G	exponential factor for grain size in sinter stress	-
Ψ_T	exponential factor for temperature in sinter stress	-
ρ	density	$\mathrm{kg\,m^{-3}}$
ρ_0	initial density	$\mathrm{kg\,m^{-3}}$
ρ_{ref}	material constant depending on green part properties for sinter stress	%
ρ_{rel}	relative density	%
σ	stress on a debinding sample	Pa
$\sigma^{'}$	deviatoric stress	Pa
$\sigma_1, \sigma_2, \sigma_3$	principle stresses	Pa
σ_u	stress threshold of a debinding sample	Pa
σ_0	material constant depending on surface energy for sinter stress	Pa

σ_m	hydrostatic stress	Pa
σ_{sp}	stress scale parameter of a debinding sample	Pa
σ_s	sinter stress	Pa
θ	porosity	%
θ_0	porosity of loose powder	%
θ_σ	absolute angle between the stress vector and the XY plane	°
ζ	exponential factor for sinter stress	-

Roman Symbols

Symbol	Description	SI Units
A_g	pre-exponential constant for grain growth	$\mathrm{m^2\,s^{-1}}$
a_η	temperature coefficient for apparent viscosity	$\mathrm{N\,m^{-2}\,s\,K^{-1}}$
A_e	members' angle in the 4-member part	°
a_{shc}	temperature coefficient for specific heat capacity	$\mathrm{J\,K^{-2}\,kg^{-1}}$
a_{td}	temperature coefficient for thermal diffusivity	$\mathrm{m^2\,s^{-1}\,K^{-1}}$
a_{tec}	quadratic term's temperature factor for thermal expansion coefficient	$\mathrm{K^{-3}}$
a_W	quadratic term's relative density coefficient for anisotropy factor	-
B	width of the reversed-U and bracket-like geometries	m
b_η	material constant for apparent viscosity	$\mathrm{N\,m^{-2}\,s}$
b_a	arm's width in the cross-shape and T-shape geometries	m
B_m	mass's width at the end of the self-stressing bending specimen	m
b_{shc}	material constant for specific heat capacity	$\mathrm{J\,K^{-1}\,kg^{-1}}$
b_{td}	material constant for thermal diffusivity	$\mathrm{m^2\,s^{-1}}$
b_{tec}	linear term's temperature factor for thermal expansion coefficient	$\mathrm{K^{-2}}$
b_W	linear term's relative density coefficient for anisotropy factor	-
c_0	specific heat capacity of a fully dense material	$\mathrm{J\,K^{-1}\,kg^{-1}}$
c_η	exponential temperature coefficient for apparent viscosity	$\mathrm{K^{-1}}$
c_{eff}	effective specific heat capacity	$\mathrm{J\,K^{-1}\,kg^{-1}}$
c_{tec}	material constant for thermal expansion coefficient	$\mathrm{K^{-1}}$
c_W	material constant for anisotropy factor	-
D_n	neck's diameter in the self-stressing tensile specimen	m
D_{arm}	arm's diameter in the self-stressing bending specimen	m
F_{sub}	substitute force on the bending and tensile specimens	N
G	grain size	m
g	gravitational acceleration	$\mathrm{m\,s^{-2}}$
H	height of the reversed-U and bracket-like geometries	m
h_t	height parameter in the self-stressing tensile specimen	m
H_t	height of the T-shape geometry	m
k_0	thermal conductivity of a fully dense material	$\mathrm{W\,K^{-1}\,m^{-1}}$
k_{eff}	effective thermal conductivity	$\mathrm{W\,K^{-1}\,m^{-1}}$
L	length of the reversed-U and bracket-like geometries	m
L_{arm}	arm's length in the self-stressing bending specimen	m
L_a	arm's length in the cross-shape and T-shape geometries	m
L_e	members' length in the 4-member part	m

m	shape parameter of a debinding sample	-
m_a	arm's mass in the cross-shape and T-shape geometries	kg
p	material constant for normalized bulk viscosity	-
P_f	probability of failure	-
p_s	material constant for normalized sinter stress	-
p_{tec}	linear term's porosity factor for thermal expansion coefficient	K^{-1}
q	material constant for normalized bulk viscosity	-
Q_g	activation energy for grain growth	$\mathrm{J\,mol}^{-1}$
R	universal gas constant	$\mathrm{J\,K}^{-1}\,\mathrm{mol}^{-1}$
S_e	side length of the tip masses in the 4-member part	m
T	temperature	K
t_a	arm's thickness in the cross-shape and T-shape geometries	m
T_{SAT}	sintering activation temperature	K
V	volume of a debinding sample experiencing stress	m^3
V_t	volumetric parameter in the self-stressing tensile specimen	m^3
V_m	mass's volume at the end of the self-stressing bending specimen	m^3
W	anisotropy factor	-
W_t	width of the middle pillar in the T-shape geometry	m
x_1	nonlinear transformation of stress in the Weibull model	-
x_2	print direction indicator in the Weibull model	-

Chapter 1

Introduction and Motivation

Metal Additive Manufacturing (AM) processes present the opportunity to fabricate products and components that were previously unattainable or economically unfeasible through other manufacturing technologies. Metal AM has been experiencing substantial growth potential, driven by the need for customized and complex products as well as shorter lead times, across various industries, including aerospace, automotive, and medical sectors [1–8].

As a metal AM technology, Metal Binder Jetting (MBJ) can print multiple parts layer-by-layer in a single print job, resulting in faster build rates than other metal AM technologies. The printed parts are subjected to debinding and sintering to achieve the desired material properties. The advantages of MBJ over other metal AM technologies include but are not limited to faster build rates, the absence of residual stress throughout the printing process, good surface quality, and supportless manufacturing. These benefits make MBJ well-suited for integrating optimized and functional-based designs into industrial components for small to medium-sized serial productions [9–12].

The debinding and sintering stages are faced with several technical challenges in MBJ. In general, Powder Metallurgy (PM) parts with binders typically undergo a strength reduction during debinding when a substantial portion of the binder is burned off, resulting in brittle parts. Improper debinding regimes, density variations, non-uniform temperature gradients, vibrations, and geometry effects may all contribute to debinding/sintering failures and the formation of cracks [13–19]. In MBJ, larger and more intricate parts are commonly produced, which increases the likelihood of damage and failure compared to other PM processes. Additionally, the relatively low green part density of MBJ components results in reduced green part strength, making them more susceptible to failure. In Fig. 1.1, an MBJ part exhibits cracks after the debinding and sintering.

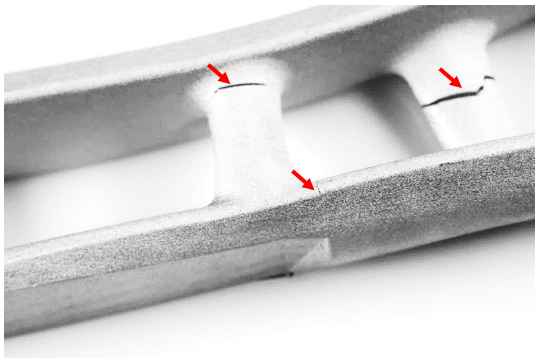

Figure 1.1 Cracks (marked with arrows) are observed after debinding/sintering of an MBJ part.

Moreover, the densification of printed parts during sintering is accompanied by significant shrinkage, resulting in a noticeable dimensional change. Anisotropic shrinkage and distortion can occur during sintering for various reasons, such as inhomogeneous density distribution, gravity, and friction. These factors pose a major challenge for manufacturing MBJ parts with high dimensional accuracy, which is crucial for industrial applications [10, 11, 20–28]. Fig. 1.2 depicts a sintered geometry exhibiting distortions due to its unique shape versus the intended target shape of the geometry.

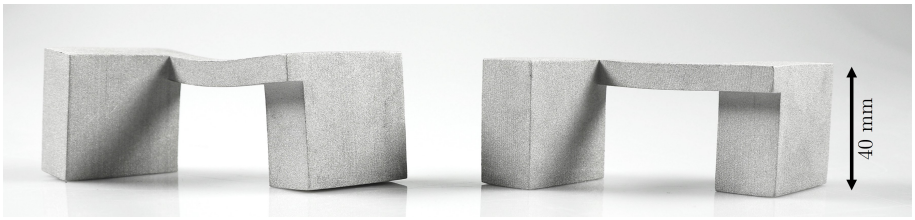

Figure 1.2 Left: A distorted MBJ part after sintering, and right: the desired shape of the same geometry.

The present study focuses on addressing the challenges related to debinding/sintering failures and sintering deformations in MBJ technology with the aim of advancing its technological readiness level. Hence, new approaches are investigated for predicting debinding/sintering failures and compensating for sintering deformations in MBJ components.

Chapter 2

State of the Art

2.1 Metal Binder Jetting

In the process chain of MBJ, Computer-Aided Design (CAD) files of the intended products are first provided to a slicing software, which then, along with the printing parameters, enables the printing process. The metal powder particles are usually spread onto the printing chamber from a powder reservoir or material feeder using a roller during printing. Subsequently, the binder is selectively applied through print heads to bond the powder particles within each layer. This process is repeated until the complete part geometry is generated layer by layer. Depending on the type of printer or binder used, the binder may require different curing techniques after printing to provide adequate bonding strength in the finished parts. The resulting cured powder-binder-void skeleton, as shown in Fig. 2.1, is referred to as the green part and is then extracted from the loose powder in a depowdering stage, requiring careful handling [12, 25, 29–33].

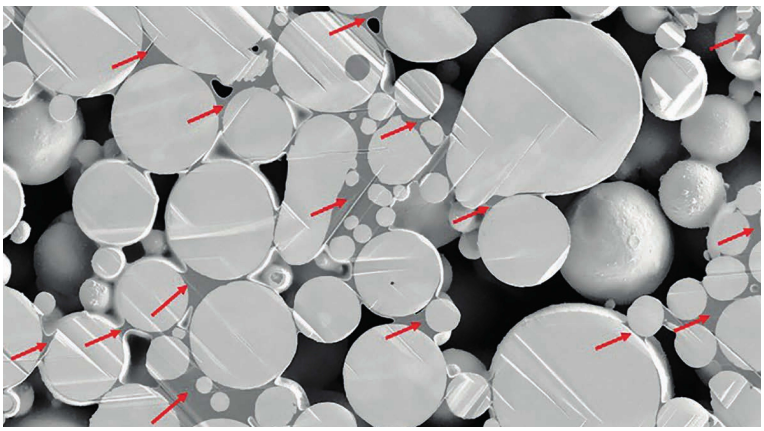

Figure 2.1 The cross-section of a green part shows the interaction between powder (gray particles), cured binder (marked with red arrows), and void (black) [34].

The Relative Density (RD)[1] of green parts in MBJ is reported to be in the range of 50 % to 64 % [28, 35–43]. To increase this low density to nearly full density, the green parts are placed on a ceramic plate, commonly known as a sintering setter, and subjected to a sintering process in a furnace. However, performing a debinding stage before sintering is crucial to eliminate residual binder from the green parts and prevent carbonization at high sintering temperatures [37, 44–46].

[1] RD refers to the ratio of a porous material's density to that of the same material in a fully dense state.

For high-melting-point materials like steels, debinding and sintering are typically carried out in a single furnace under a controlled atmosphere such as vacuum, nitrogen, or hydrogen. Dependent on the binder employed in the production of green parts of Stainless Steel 316L (SS316L), the binder typically burns off at temperatures below 600 °C. Sintering of SS316L parts is conducted at temperatures between 1200 °C and 1400 °C, with the holding time being determined by the desired final density [11, 33, 37, 47, 48]. Fig. 2.2 displays the process chain of MBJ schematically.

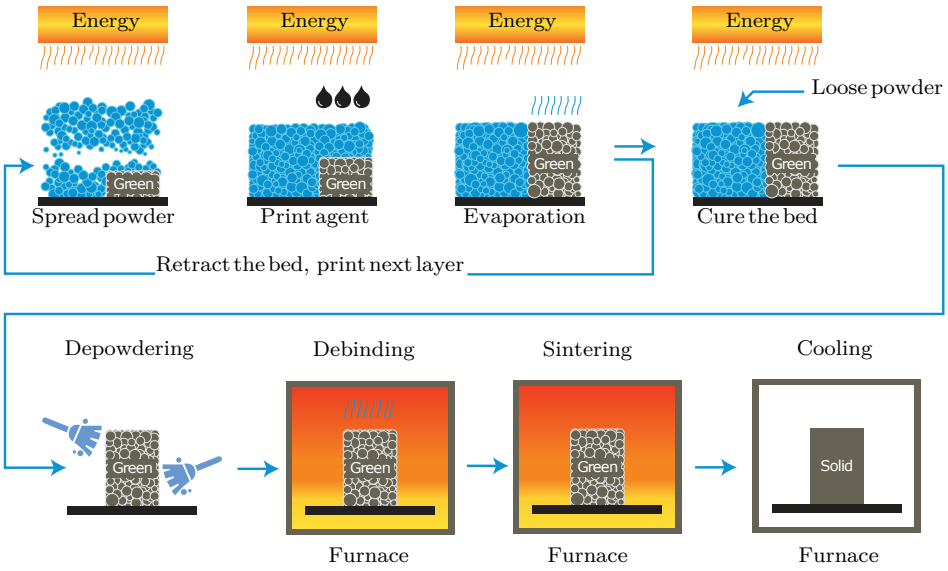

Figure 2.2 The process chain of the MBJ; the figure is adopted from [34].

The densification of green parts during sintering is influenced by various factors, including Powder Size Distribution (PSD), powder morphology, Green Part Density (GPD), and sintering parameters [23, 47, 49–55]. The densification process is accompanied by significant shrinkage, resulting in a noticeable dimensional change. The shrinkage in MBJ parts is anisotropic, where the green parts usually experience a larger dimensional change in the powder stacking direction (build direction) due to the available gaps between the layers [10, 11, 24–26].

In addition to shrinkage, sintering can distort MBJ parts. At high temperatures where the material is presenting a viscous behavior, distortion (interchangeably referred to as ”warpage” in this thesis) can occur due to various reasons, such as gravity, friction between green parts and sintering setter, inhomogeneous density distribution within green parts, anisotropic shrinkage, and non-uniform shrinkage of green parts due to their geometry [20–23, 26–28].

2.2 Sintering Theory

Sintering is a heat treatment process that irreversibly bonds particles in porous materials, resulting in the densification of materials. During the sintering process, the reduction of surface energy and surface area, as well as the minimization of curvature gradients, lead to the growth and strengthening of the interparticle bonds. The bonding of particles is initiated through forming and growing the so-called sintering necks between them. During the early stages of neck growth between particles, the primary driving force is the curvature gradients. The sinter driving force or stress on curved surfaces is inversely proportional to its curvatures. Upon heating, atoms undergo motion along these gradients.

The temperature required to initiate atomic motion depends on both the material properties and the particles' size [19, 56–58].

The neck region of the particles transforms into a concave shape, which further expands to reduce tension in the structure. Conversely, the surrounding convex region experiences opposing stresses, causing atoms to migrate away from this region towards the neck region. This results in filling the gaps between particles, reducing overall stress gradients, and promoting the formation of sinter bonds. As the sinter bonds grow, the surface area and curvature gradients of the particles decrease, which slows down the rate of sintering [15, 19, 49, 56, 58, 59].

During solid-state sintering, atomic movements happen through different transport mechanisms. These mechanisms can be classified into two main categories: surface and bulk transport. Surface transport mechanisms, such as surface diffusion, lattice diffusion from the surface, and evaporation-condensation, lead to the neck formation between particles without substantial densification. In contrast, bulk transport mechanisms, such as plastic flow, grain boundary diffusion, and volume diffusion, result in the material's neck formation and densification [59–63].

In polycrystalline materials, the reduction of interfacial energy due to minimizing free surface area results in not only densification but also grain growth through the movement of grain boundaries and consumption of other grains. Grain boundaries play a significant role in determining the shape of grains and pores, as well as influencing material transport during sintering. The growth rate of grains is influenced by factors such as initial Grain Size (GS), sintering time, and temperature [64–70].

Classical sintering theories, based on phenomenological observations, propose that the sintering process can be divided into three distinct stages: initial, intermediate, and final (See Fig. 2.3 and assume each particle in the figure has a single crystal or grain. For polycrystalline materials, each particle contains several grains). In the initial stage, neck formation and growth occur, but there is limited densification. Moreover, grain growth is negligible [15, 19, 49, 71]. Fig. 2.4a illustrates the neck formation of the particles during the initial stage at porosity values of about 38 %.

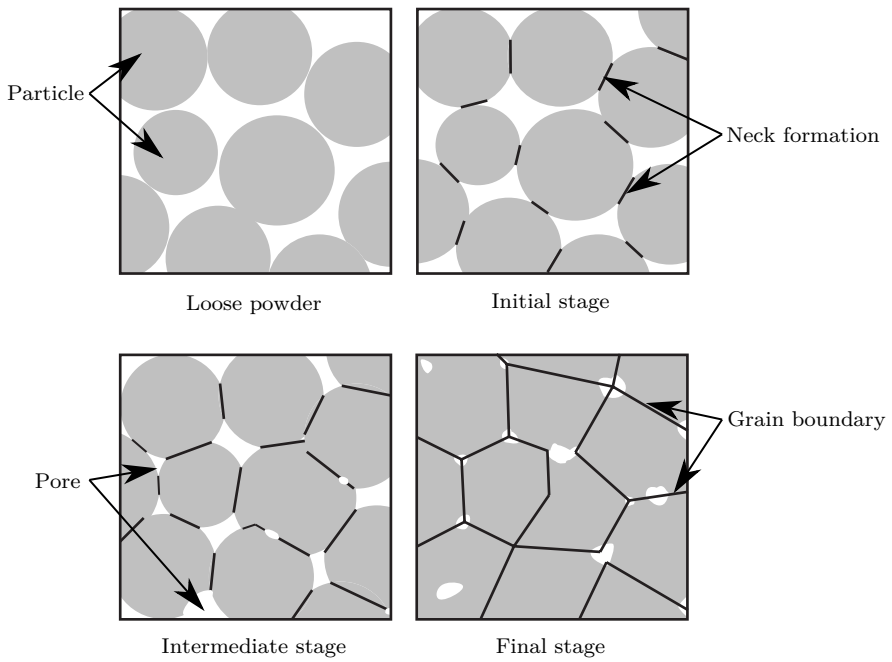

Figure 2.3 Densification process, pore, particle, and grain changes at different stages [59].

In the intermediate stage, the pores transform into smoother and interconnected tubular shapes. Densification progresses rapidly, but the rate slows as the degree of curvature and surface area decreases. In the later phase of the intermediate stage, grains start to grow [19, 49, 71–73]. The transformation of the pore structure and the diffusion between particles can be observed in Fig. 2.4b.

Upon reaching the final stage of the sintering process, which occurs at porosity levels of approximately 8 %, growth of the grains can be observed. Furthermore, the pores undergo a transformation in which they become elongated and decrease in diameter, ultimately collapsing into spherical, isolated, and closed shapes. As a result of the increasing densification and grain growth, the available surface energy decreases significantly, leading to the eventual cessation of the sintering process towards the end of the cycle [19, 49, 71–73]. At the final stage, the grain morphology changes into idealized tetrakaidecahedron, 14-sided geometries consisting of squares and hexagons (See Fig. 2.4c) [59].

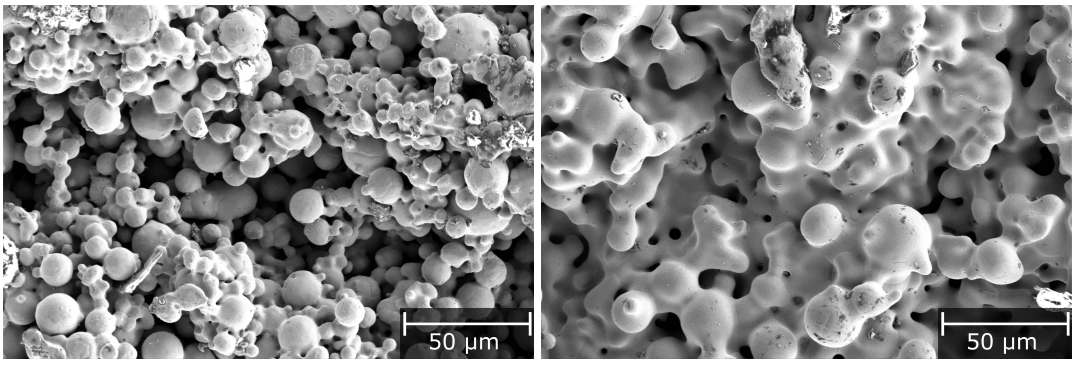

(a) **(b)**

(c)

Figure 2.4 The evolution of sintering in different stages, (a): the initial stage, (b): the intermediate stage, and (c): the final stage.

2.3 Debinding/Sintering Damage

One of the significant challenges in the production of PM components is the occurrence of cracks and damages that may be first detectable after the sintering process. The literature survey indicates that cracks primarily originate during the formation, handling, and debinding of green parts [13, 14, 16–18, 74–78]. The root cause of these cracks and damages is attributed to inadequate interparticle bonding.

Zenger et al. have classified the possible causes of cracks into four categories: improper material composition, interparticle sliding action, improper release of elastic strain, and high tensile/shear stresses [16]. During the debinding process, the interparticle bonds become weaker, and a backbone polymer structure primarily holds the particles together. The weakened bonding structure is vulnerable to damage during debinding and the initial stage of sintering due to various factors, such as the part's geometry, thermal shocks and expansions, non-uniform density distribution, and external loads or vibrations [46, 75, 76, 78].

For viscoplastic porous materials, a deterministic microstructure-based model is presented to describe the interaction between the creep behavior and fracture [79, 80]. The model can be utilized to predict damage of porous media at high temperatures, where material shows a viscous and ductile behavior comparable to sintering.

In the course of debinding, on the other hand, the material is brittle. Due to the sensitivity of brittle materials to the existing cracks, defects, and stress concentrations, as well as the heterogeneous nature of green parts, deterministic damage models are not recommended [81, 82]. In fused filament fabrication, BASF introduced a guideline to avoid debinding failure of SS316L by setting a stress threshold [83]. According to the method, the stress of the parts under their own weight is calculated by Finite Element (FE) simulations, and in case of exceeding the stress threshold, redesign is suggested. The effect of different print directions is also considered in the guideline. The method presented by [83] is also implemented in a study by Rosnitschek et al. to predict debinding failures [84]. Rosnitschek et al. also propose that the accuracy of failure predictions can be increased with the use of Weibull statistics, as proved by [85, 86] for brittle materials.

Weibull Distribution

According to the Weakest Link Theory introduced by Weibull, a system made up of multiple single links fails when the weakest link fails [87]. The theory can be applied to brittle materials to estimate the probability of failure [88–90].

A Cumulative Distribution Function (CDF), which includes uniaxial uniform tensile stress σ, is defined by Weibull:

$$P_f(\sigma) = 1 - exp\left[-V\left(\frac{\sigma}{\sigma_{sp}}\right)^m\right], \tag{2.1}$$

where P_f is the probability of failure, V is the volume of the specimen suffering from stress σ, m is the shape parameter, and σ_{sp} is the scale parameter [88].

For brittle materials, a three-parameter (3-p) Weibull CDF with uniaxial uniform tensile stress σ is formulated by adding a stress threshold to the standard Weibull distribution:

$$P_f(\sigma) = \begin{cases} 1 - exp\left[-V\left(\frac{\sigma - \sigma_u}{\sigma_{sp}}\right)^m\right], \sigma > \sigma_u \\ 0 \qquad\qquad\qquad\qquad\qquad\quad , \sigma \leq \sigma_u, \end{cases} \tag{2.2}$$

where σ_u is a stress threshold for failure [88]. In case of uniaxial non-uniform stress, the 3-p Weibull CDF is defined by [88]:

$$P_f(\sigma) = 1 - exp\left[-\int_V \left(\frac{max\left(\sigma - \sigma_u, 0\right)}{\sigma_{sp}}\right)^m dV\right]. \tag{2.3}$$

Based on the Principle of Independent Action, which accounts for each principal stress independently, and by neglecting the threshold σ_u, the Weibull distribution can be expanded to a 3-p Weibull CDF with multi-axial non-uniform tensile stress σ as presented by:

$$P_f(\sigma) = 1 - exp\left\{-\int_V \left[\left(\frac{\sigma_1}{\sigma_{sp}}\right)^m + \left(\frac{\sigma_2}{\sigma_{sp}}\right)^m + \left(\frac{\sigma_3}{\sigma_{sp}}\right)^m\right] dV\right\}, \tag{2.4}$$

where σ_1, σ_2, and σ_3 are the principle stresses [89, 91, 92].

Maximum Likelihood Estimation is an effective approach to fit the data with the Weibull distribution [93]. By maximizing a likelihood function, which is a composition of a probability distribution function at each data point, data fitting is performed. Using the simplest form of the Weibull model (Eq. 2.1), the probability distribution function is defined by taking the derivative of σ:

$$f(\sigma) = \frac{dP_f(\sigma)}{d\sigma} = V\frac{m}{\sigma_{sp}}\left(\frac{\sigma}{\sigma_{sp}}\right)^{m-1} exp\left[-V\left(\frac{\sigma}{\sigma_{sp}}\right)^m\right]. \tag{2.5}$$

For the collected experimental data, stress σ and its distribution is known. The points of experimental data are then

$$(\sigma_n, f(\sigma_n)),$$
$$0 < n \leq N,\ n \in \mathbb{Z},$$

where N is the number of collected data in the experiment. The likelihood of each data point is

$$\Lambda_n(m, \sigma_{sp}) = f(\sigma_n) = V\frac{m}{\sigma_{sp}}\left(\frac{\sigma_n}{\sigma_{sp}}\right)^{m-1} exp\left[-V\left(\frac{\sigma_n}{\sigma_{sp}}\right)^m\right]. \tag{2.6}$$

The corresponding likelihood function Λ is consequently explained by:

$$\Lambda(m, \sigma_{sp}) = log\prod_{i=1}^{n}\Lambda_i(m, \sigma_{sp}) = \sum_{i=1}^{n} log(\Lambda_i(m, \sigma_{sp})). \tag{2.7}$$

By taking partial derivations of Λ with respect to m and σ_{sp} and by setting each derivative to 0, the corresponding m and σ_{sp} can be found.

2.4 Sintering Numerical Models

Numerous experiments have been carried out to examine the mechanical properties and dimensional accuracy of objects produced through sintering in MBJ [38, 50, 53–55, 94–96]. However, due to the impact of various influential factors, such as uneven distribution of pores, gravity, and friction, it is difficult to achieve the desired outcomes through experiments alone [21, 22, 94, 97–101]. As a result, numerical simulations can be used as they provide a cost-effective way to overcome these challenges and gain valuable insights into sintered components' mechanical properties and dimensional accuracy [102–109].

2.4.1 Sintering Models Over Scales

The mathematical techniques used for simulating the sintering process or sinter-induced deformation can be classified into four categories: atomic scale, mesoscopic (particle) scale, macroscopic (component) scale, and multi-scale models. Atomic-scale models analyze a particle cluster at the atomic level, accounting for chemical composition and atomic arrangement to obtain information about atom trajectories and diffusion coefficients. Mesoscopic-scale simulations, such as Monte Carlo methods, can model microstructural changes such as grain growth and diffusion mechanisms in different stages of sintering. However, the computational limitations associated with atomic-level and mesoscopic-scale simulations constrain their ability to scale up in size and time, despite providing a comprehensive understanding of the sintering process [110–124].

Atomic-scale and mesoscopic-scale simulations are utilized to investigate the mechanisms of interparticle interaction in sintering, with a particular focus on local kinetics. These simulations enable the description of the densification process, which should then be generalized for macroscopic porous bodies. Using a multi-scale approach is advantageous for studying sintering processes, as it allows for combining various scales. By incorporating diffusion parameters and densification kinetics at a higher scale, multi-scale models can build a representation of the continuum mechanics of porous media in a macroscopic state. This allows for the prediction of distortion and densification of sintering bodies. However, these models heavily depend on precise modeling of lower scales, the initial Green Part Property (GPP), and other macroscopic factors such as the sintering furnace and atmosphere [102, 110, 112, 115, 118, 123–131].

GPP is mainly determined by powder characteristics, printing, and curing in binder jetting [25, 33, 36–39, 41, 96, 132, 133]. Numerical methods have been employed in different studies to investigate different material and process parameters to determine the properties of powder compaction and green parts in powder-based AM. Nevertheless, these studies have been conducted mainly on a representative volume element and need to be scaled on a component scale [11, 134–140].

2.4.2 Continuum Mechanics Sintering Models

Phenomenological macroscopic models, which require fewer parameters and have lower computational costs than multi-scale approaches, are commonly used in the industry to predict sintering deformation; despite their inability to consider microstructural evolution [112, 118]. The continuum theory of sintering posits that sintered bodies are composed of a two-phase structure comprising a skeleton and voids. The skeleton of a porous material is made up of particles that exhibit nonlinear, viscous, and incompressible behavior. The pores are assumed to be evenly distributed throughout the material, resulting in an overall isotropic response. Porous materials exhibit deformation under hydrostatic stress, unlike fully dense materials. Therefore, the continuum theory assumes that sintering results from the structure's response to the inherent hydrostatic potential, commonly referred to as sinter stress, sinter potential, or sinter driving force [110, 141–146].

The continuum theory of sintering enables the modeling of sintering deformation in porous materials by applying an appropriate rheological framework capable of describing the viscoplastic behavior of such materials. A thermo-elasto-viscoplastic material model can capture the thermally induced creep deformation and volume swelling that occur during free-sintering. The viscoplastic portion of the model accounts for these effects, while the thermo-elasto part models elastic and thermal deformations that occur at lower temperatures. [67, 103, 147, 148].

The total strain rate $\dot{\epsilon}$ is explained by:

$$\dot{\epsilon} = \dot{\epsilon}_e + \dot{\epsilon}_{th} + \dot{\epsilon}_{vp}, \tag{2.8}$$

where $\dot{\epsilon}_e$ is the elastic strain rate, $\dot{\epsilon}_{th}$ is the thermal strain rate, and $\dot{\epsilon}_{vp}$ is the viscoplastic strain rate. Defined by the Hooke's law, elastic strain rate $\dot{\epsilon}_e$ is calculated through elastic compliance matrix $\boldsymbol{C_e}$ and stress rate $\dot{\sigma}$:

$$\dot{\epsilon}_e = \boldsymbol{C_e}\dot{\sigma}. \tag{2.9}$$

The thermal strain rate $\dot{\epsilon}_{th}$ can be expressed by:

$$\dot{\epsilon}_{th} = \alpha_{tec}\, \dot{T}\boldsymbol{I}, \tag{2.10}$$

where α_{tec}, $\dot{T}$, and $\boldsymbol{I}$ are the Thermal Expansion Coefficient (TEC), temperature change rate, and the identity matrix, respectively.

During the sintering of SS316L, grain boundary diffusion is one of the prevalent mechanisms for bulk transport [64, 66, 149]. At a macroscopic level, the sintering process can be modeled using continuum mechanics-based constitutive sintering models, which accounts for grain boundary diffusion. Among the available models described by [110, 142, 150, 151], the Skorohod Olevsky Viscous Sintering (SOVS) model, using the FE method, can effectively characterize the densification and viscous behavior of porous SS316L bodies during sintering. This effectiveness is attributed to the model's reliance on fewer phenomenological parameters that are physically interpretable [144, 146]. According to SOVS, the viscoplastic strain rate is calculated by the following equation:

$$\dot{\epsilon}_{vp_{ij}} = \frac{\sigma^{'}_{ij}}{2\eta_s} + \frac{\sigma_m - \sigma_s}{3\eta_b}\delta_{ij}. \tag{2.11}$$

In the first term of the right-hand side of Eq. 2.11, which captures the creep deformation, $\sigma^{'}_{ij}$ is the deviatoric stress, and η_s is the shear viscosity. The second term denotes the volumetric shrinkage, where σ_m is the hydrostatic stress, σ_s is the sinter stress, δ_{ij} is the Kronecker delta, and η_b is the bulk viscosity [110, 144].

In free-sintering, the elastic strains are several orders of magnitude smaller than thermal and viscoplastic strains, and therefore, they can be neglected [144, 152]. Densification of the powder skeleton is calculated by

$$\rho = \rho_0\ \exp[-\epsilon_{vp_{ii}}], \tag{2.12}$$

where ρ_0 is the initial density, and $\epsilon_{vp_{ii}}$ is the trace of the viscoplastic strain tensor.

To put it briefly, macroscopic densification during sintering, which is the result of microscopic morphological changes, can be modeled by explaining grain growth mechanism, viscosity, and sinter stress phenomenologically [153, 154]. Below, the explanation and phenomenological modeling of these physical parameters are given.

Grain Growth

Definition: The minimization of available interfacial energy describes the densification of sintering bodies, which is accompanied by grain growth in polycrystalline materials. Through grain growth, smaller grains turn into bigger ones, resulting in overall surface area reduction, leading to lower available surface energies for sintering [64, 66–68, 70, 155].

Phenomenological modeling: Grain growth for the austenitic polycrystalline steels can be described in an Arrhenius-type expression as a function of temperature T, current grain size G, and activation energy for grain growth Q_g as follows:

$$\frac{dG}{dt} = \frac{A_g \exp\left[\frac{-Q_g}{RT}\right]}{G}, \tag{2.13}$$

where $\frac{dG}{dt}$ is the rate of grain growth, A_g is a pre-exponential constant, and R is the universal gas constant [64, 144].

Viscosity

Definition: Viscosity is the resistance of a material to densification and distortion during sintering, relying on material porosity, GS, and temperature [20, 156–160]. Shear and bulk viscosity of materials play a central role in theories of viscoplasticity.

Phenomenological modeling: Previous studies have suggested different models for porous materials to determine shear and bulk viscosity [20, 110, 145, 161]. For instance, for bulk viscosity η_b, a summary of the models is given by Olevsky as presented in Tab. 2.1.

Model	Norm. Bulk Viscosity	Model	Norm. Bulk Viscosity
[162]	$\frac{(q+1)(1+\theta)(1-\theta)^{\frac{2}{q+1}}}{3\theta}$	[20]	$\frac{1-\theta}{2G\theta^p}$
[163] [1^{st} stage]	$(1-\theta)^{5.26}$	[163] [2^{nd} stage]	$\frac{(1-\theta)^{5.26}}{G\theta^p}$
[164, 165] [166, 167]	$\frac{2}{3}\left(\frac{1-\theta^q}{q\theta^q}\right)^{\frac{2}{q+1}}$	[168]	$\frac{3(1-\theta)^2(\theta_0-\theta)}{\theta_0}\left[\frac{16\sqrt{3\theta_0}}{27\pi\sqrt{\theta_0-\theta}}\right]^q$
[169, 170] [1^{st} stage]	$\frac{(1-\theta)(\theta_0-\theta)^2}{G{\theta_0}^2}$	[169, 170] [2^{nd} stage]	$\frac{1-\theta}{G\sqrt{\theta}}$
[171]	$\frac{27(1-\theta)^{\frac{2}{q+1}}}{8\theta}$	[172]	$(1-\theta)\exp[-2\theta]$
[173]	$\frac{2(1-\theta)^3}{3\theta}$	[174]	$\frac{\ln\theta+0.5(1-\theta)(3-\theta)}{G(\theta-1)}$

Table 2.1 Derived equations for normalized bulk viscosity as a function of porosity of loose powder θ_0, current porosity of sintering body θ, material constant p, q, and grain size G from different researches [110].

Due to diversity and the large number of empirical model constants in the equations introduced by these studies, several experiments are required, making these studies hard to use. Using an elastic-viscous analogy, Olevsky explained shear and bulk viscosity, respectively by:

$$\eta_s = \eta_0\, \rho_{rel}^2, \tag{2.14}$$

and

$$\eta_b = \frac{4}{3}\,\eta_0\,\frac{\rho_{rel}^3}{(1-\rho_{rel})}, \tag{2.15}$$

where η_0 is the apparent viscosity of a fully dense body and ρ_{rel} is RD [110]. According to Eq. 2.14 and Eq. 2.15, the apparent viscosity and density evolution should be determined. Density evolution or porosity values with respect to time and temperature can be easily measured by different experimental approaches, such as sintering dilatometry. On the contrary, the determination of apparent viscosity requires laborious experiments.

To measure apparent viscosity, Rahaman et al. and Zuo et al. used sinter-forging (loading dilatometry) experiments to determine the shear and bulk viscosity of porous soda-lime-silica and Al_2O_3, respectively [158, 172]. In sinter-forging experiments, a constant load is applied to the dilatometry specimen to study the creep and densification of the porous material at the same time. Since the specimen remains under a permanent load in this experiment, the density and the microstructure evolutions differ from those in free-sintering. Furthermore, the specimens shrink anisotropically under the effect of the constant load [158, 172, 175, 176]. The impacted density, microstructure, and anisotropy in sinter-forging experiments result in an overestimated viscosity as of that in free-sintering [175].

It is possible to measure free-sintering strain and loaded strain using cyclic loading dilatometry. An external force is repeatedly applied to and removed from the specimen in the cyclic loading sintering. Therefore, the occurred free shrinkage due to free-sintering can be measured in the unloading steps, while viscosity can be determined in the loading steps [156, 175, 176].

Another approach to measure viscosity is the 3-point bending creep test using simply supported beams. The viscosity is measured using the deflection of the middle point on the specimens. It is assumed in the test that the middle point deflects purely downwards due to viscosity changes without any lateral movement. Song et al. performed creep tests on Metal Injection Molding (MIM) green specimens in consecutive sinter runs at different temperatures for two heating rates ($5\,\mathrm{K/\,min}$ and $10\,\mathrm{K/\,min}$) [106]. Every time a specimen was heated to a specific temperature and then cooled down. The deflection of the beam in the middle was measured at Room Temperature (RT) after each sinter run. To find the corresponding densification (porosity amount), separate dilatometry experiments were performed in their research. Since the specimens could freely slip on their supports due to densification and because of possible vibrations (displacements) while loading/unloading the specimens in the furnace, deflection measurements could be influenced. On the other hand, measuring at discontinuous temperatures increases the degree of non-repeatability in the study by Song et al.

To tackle the mentioned problems, Lee et al. measured the beam deflections on ZrO_2 samples in a tube furnace using a camcorder with $5\,^{\circ}\mathrm{C}$ intervals [157]. The measurements were made for different pre-sintered samples to investigate the effect of density on viscosity. They also studied the effect of the grain sizes and reported that the viscosity is the function of relative density and GS.

Sinter Stress

Definition: Sintering of a porous body generates capillary forces from its surface energy, leading to inherent stress termed "sinter stress". In other words, mechanical stress must counterbalance the internal surface tension forces arising during sintering to achieve equilibrium. Sinter stress is the mechanical stress that counteracts capillary forces originating from surface tension and ensures total energy equilibrium of the porous media during sintering [59, 153, 177, 178].

Phenomenological modeling: Similar to the efforts made in determining viscosity, a significant amount of research has been dedicated to developing expressions for determining sinter stress. Tab. 2.2 presents a summary of these expressions as compiled by [110].

By taking GS evolution into account, Olevsky proposed the following expression for sinter stress:

$$\sigma_s = \frac{6\gamma_s\,\rho_{rel}^2}{G}, \tag{2.16}$$

where γ_s is the surface tension of the powder, and G is the GS [110].

Model	Norm. Sinter Stress
[169] [1^{st} stage]	$(1-\theta)^2 \left[\frac{2(1-\theta)-(1-\theta_0)}{\theta_0}\right]$
[169] [2^{nd} stage]	$\sqrt[3]{\frac{6(1-\theta)}{\theta}}$
[168]	$(1-\theta)^{\frac{5}{3}}$
[179]	$(\sqrt[3]{1-\theta})\left(\frac{p_s}{\sqrt[3]{\theta}}+G\right)$
[173]	$(1-\theta)^2$

Table 2.2 Derived equations for normalized sinter stress as a function of porosity of loose powder θ_0, current porosity of sintering body θ, material constant p_s, and grain size G from different studies [110].

2.4.3 Conservation Laws

Despite the volume change of sintering bodies, mass is conserved during sintering by assuming that the binder is totally removed before the start of the sintering. After the complete debinding of sintering bodies and neglecting the mass of air confined in pores, mass conservation is guaranteed by density evolution. The momentum conservation is also fulfilled by considering the free-sintering boundary conditions, leading to the formation of the Cauchy stress tensor [152]. By neglecting the dissipated energy as the result of viscoplastic work, the conservation of energy is described by:

$$\rho\, c_{eff}\, \dot{T} - \mathrm{div}(k_{eff}\, \nabla T) = 0, \tag{2.17}$$

where ρ is the density, c_{eff} is the effective specific heat capacity, and k_{eff} is the effective thermal conductivity of the sintering body. T and $\dot{T}$ are the temperature and the temperature rate, respectively. The effective specific heat capacity and thermal conductivity of porous bodies are functions of the density [152, 180–184] and have been empirically calculated from those of fully dense material, respectively, as given by:

$$c_{eff} = c_0\, \rho_{rel}^2, \tag{2.18}$$

and

$$\frac{k_{eff}}{k_0} = \frac{1-\theta}{1+11\,\theta^2}, \tag{2.19}$$

where c_0 and k_0 are the specific heat capacity and thermal conductivity of a fully dense material. The specific heat capacity of a fully dense material is determined experimentally. Thermal conductivity is extracted by:

$$k_0 = \alpha_d\, \rho\, c_0, \tag{2.20}$$

where α_d is the thermal diffusivity of a fully dense material and is measured experimentally.

2.4.4 Implementation of Sintering Simulations

Several research works have developed and employed constitutive equations to simulate the sintering of ceramics and metals at the component scale, specifically for MIM parts [102, 103, 106, 110, 142, 144, 148, 185, 186].

In MBJ, to investigate the sintering behaviors of SS316L parts, Zhang et al. have developed a macroscopic FE model based on a phenomenological approach inspired by the SOVS model. The essential material properties, including viscosity, surface tension, and grain growth, were gathered primarily from literature related to other PM technologies. The study demonstrated that the FE model could predict the experimental deformation of cantilever and bridge-shaped coupons produced by MBJ with acceptable accuracy. However, they identified the need for more precise material properties, particularly at high temperatures, to improve the accuracy of sintering models [161]. Moreover, the research by Zhang et al. did not address issues such as reproducibility and part complexity in metal AM [26, 28, 187, 188].

2.5 Deformation Compensation

To achieve dimensional accuracy, manufacturing distortions should be either removed or compensated. Following design guidelines [189–191] and developing reactive binders [192] can mitigate sintering distortion. To compensate for distortions, experimental-based methods are used in Selective Laser Sintering [187, 193] and Laser Powder Bed Fusion (LPBF) [194] technologies. Experimental-based methods are utilized in MBJ as well. In a study by Zhago et al., a model is introduced to predict the dimensional accuracy of parts printed in different directions [94]. However, such methods are only able to compensate for sintering shrinkage but not for distortions. Numerical-based methods are used in LPBF and directed energy deposition to compensate for manufacturing distortions. FE analysis is employed to calculate deformations, and the distortion directions are inverted to achieve dimensional accuracy [195–197].

Chapter 3

Objectives

Given the complex nature of industrial MBJ parts, the product development phase can be both complicated and costly. To mitigate the expense of trial-and-error experimentation and facilitate the economical development of new industrial designs, there is a need for prompt probabilistic approaches that can predict the likelihood of product failure. These approaches can serve as guidelines during product development to minimize failure rates. As a result, further development of the probabilistic models presented in Sec. 2.3 to predict debinding/sintering damage of MBJ parts is essential for reducing lead times.

Numerical modeling of sintering deformations based on phenomenological macroscopic models is performed for manufacturing technologies such as MIM in different studies. However, compared to PM components processed by compaction techniques, green part densities in MBJ are lower, typically ranging from 50 % to 64 % of a fully dense body [11, 43, 198]. As a result, MBJ parts experience higher shrinkage and distortion during sintering. In contrast to sintered parts produced by other PM processes, which generally range from 10 mm to 100 mm in size [15, 18], or MIM parts with an average mass of 15 g [199], MBJ parts exhibit the potential for greater dimensional extents and intricate geometries including channels, lattice structures, undercuts, and overhang areas. These attributes of MBJ components result in increased effects of gravity, friction, and non-uniform shrinkage during sintering, leading to significant distortion and reduced dimensional accuracy. Moreover, due to interlayer gaps in the build direction, shrinkage occurs inhomogeneously, particularly along the build direction in MBJ [10, 11, 94, 192, 200, 201].

Due to the distinctive characteristics of MBJ parts compared to other PM components, it is crucial to validate the use of phenomenological macroscopic models, such as the SOVS model used in MIM, for MBJ to accurately predict the sintering-induced deformation. The assumption of isotropic pore distribution in the SOVS model for sintering bodies should be carefully studied due to evidence from previous studies on MBJ components, indicating that pores are distributed non-uniformly, especially in the build direction [10, 11, 40, 94, 110, 140, 202, 203].

Although the thermal elastic-viscoplastic constitutive law presented by Zhang et al. demonstrated satisfactory agreement with experimental results for simple geometries, it is suggested that the material model be calibrated with MBJ-specific specimens to enhance model accuracy [161]. Moreover, the existing models do not account for the unique challenges posed by MBJ technology, such as reproducibility, part complexity, anisotropic shrinkage, and variations in green part properties. Thus, it is necessary that these issues are investigated and incorporated to ensure accurate prediction of sintering-induced deformation in MBJ technology.

Furthermore, a method to estimate the GPP should be included in the material models. However, there is a lack of research to determine GPP. The sensitivity of the initial packing density on the final predictions has been investigated in the literature. In particular, studies have suggested that accurate assumptions of GPP are crucial for predicting the shrinkage of sintering bodies [28, 96, 161].

Currently, there is a lack of sufficient research to validate the accuracy and efficacy of sintering deformation models in compensating for deformations in industrial MBJ parts. As such, it is necessary to develop a framework that can compensate for the sintering deformation of MBJ parts to fabricate parts that meet the dimensional accuracy required by industrial tolerances.

In summary, this research aims to address the aforementioned challenges of MBJ technologies by pursuing the following three objectives:

1. development of a probabilistic model to predict the likelihood of debinding/sintering failure,
2. development of a macroscopic-scale phenomenological material model that incorporates the interstice characteristics of MBJ parts to predict their sintering deformation,
3. establishment of a systematic framework to compensate for the sintering deformation of industrial-related MBJ parts, which ensures compliance with industrial-required tolerances.

Fig. 3.1 outlines the main objectives of the present research.

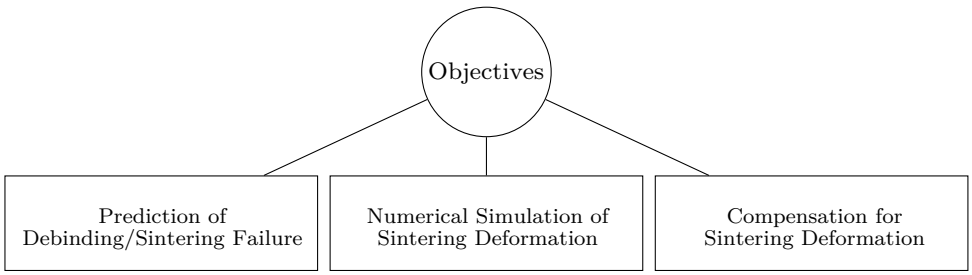

Figure 3.1 The main objectives of the thesis.

Chapter 4

Methodology

This chapter describes the methods employed in this study to realize the objectives. The first section introduces the utilized manufacturing machines, conventions, and measurement devices. The second section presents the procedure for developing a debinding failure model. The third section gives the implemented approach for the numerical simulation of sintering deformation. Finally, the last section introduces the method for compensation of sintering deformations.

4.1 Measuring Devices, Manufacturing Machines, and Material

Unless stated otherwise, the following measuring devices and standards are used for the experiments in this work.

Measuring Devices

PSD is determined according to ISO 13322-2 using a Camsizer XT PSD analyzer from Microtrac Retsch GmbH [204]. 3D-scanning is performed with the optical 3D-scanner VL-550 from Keyence Corp [205]. Metallographic analyzes are inspected with the optical digital microscope VHX-5000 of Keyence Corp [206]. Horizontal dilatometry experiments are conducted with the DIL L75 apparatus manufactured by Linseis Messgeräte GmbH [207]. Using a DSC404C Pegasus calorimeter from Netzsch GmbH, Dynamic Scanning Calorimetry (DSC) is performed [208]. Laser Flash Analysis (LFA) is carried out by LFA 427 apparatus from Netzsch GmbH [209].

Powder and Binder-Jetting Printer

At the time of writing this thesis, a pre-production series model of MetalJet printer manufactured by HP Inc. is used to produce specimens [210]. The pre-production series model is tested by Volkswagen AG within a cooperation project. Fig. 4.1 illustrates the employed print chamber dimensions of the printer and the convention used in this work for the different directions. The X direction is assigned to the moving direction of the printheads, while Y represents the recoater direction. The Z direction refers to the build or stacking direction.

In the present study, the development process is performed for SS316L, equivalent to stainless steel 1.4404 in DIN EN 10088-1 [211]. Tab. 4.1 provides the specifications for the printer, PSD, printing layer thickness, and curing temperature utilized in the experiments outlined in this thesis.

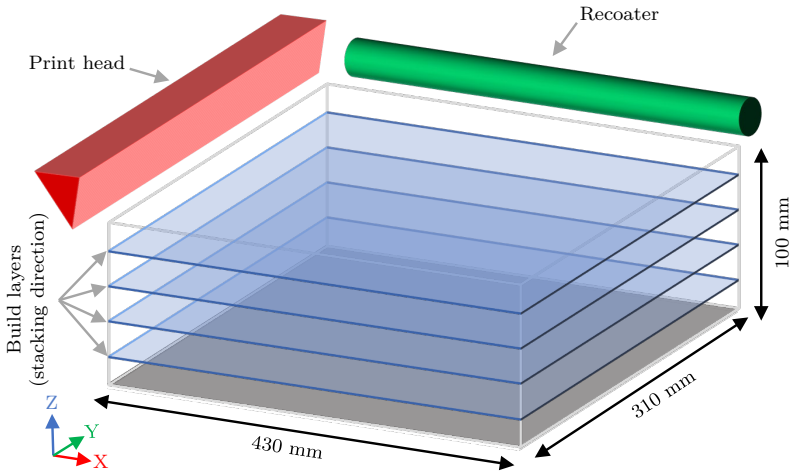

Figure 4.1 The used convention to define, recoater, print head, and build directions, as well as the utilized print chamber dimensions in this research.

Printer	PSD [µm]	Layer thickness [µm]	Curing Temp. [°C]
HP Metal Jet	7 (D_{10}), 15 (D_{50}), 27 (D_{90})	50	130

Table 4.1 The used PSD and printing parameters.

Sintering Furnace

For heat treatment processes, two furnaces are available: a NABERTHERM VHT 40/16-MO with a temperature limit of 1600 °C and a NABERTHERM NR 50/11 with a limit of 1150 °C [212]. Due to the required temperature range for the sintering process of SS316L, the VHT 40/16-MO (marked as F1) can be used for both debinding and sintering, while the NR 50/11 (marked as F2) is employed solely for debinding in this thesis. Fig. 4.2 displays the furnaces and the levels of each furnace, which can be filled with appropriate ceramic or molybdenum trays containing specimens.

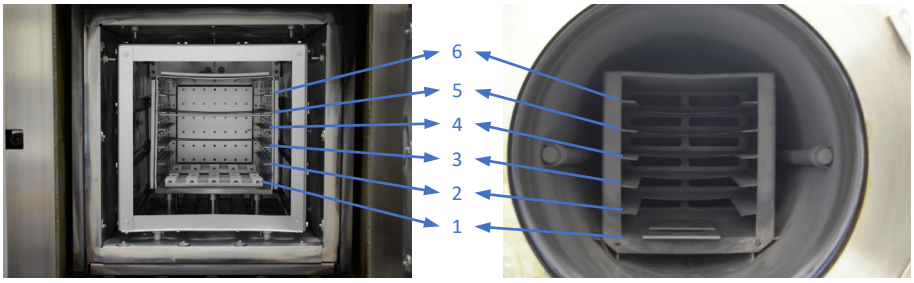

Figure 4.2 The furnaces and their loading levels.

4.2 Prediction of Debinding/Sintering Failure

To develop a reliable debinding/sintering failure model, it is essential to determine at which stage of the process damage occurs. This can be achieved through Thermal Gravimetric Analysis (TGA), enabling observation of the point at which the binder is completely burnt off from the powder skeletons. It is hypothesized that debinding/sintering failure typically occurs when the binder is removed from the green parts. To confirm this hypothesis, in-situ thermo-optical observations are conducted on self-loading specimens during debinding/pre-sintering, and any instances of failure are carefully documented. This approach will provide valuable insights into the underlying mechanisms of failure and allow for the development of more accurate debinding/sintering failure models.

In the next step, a Design of Experiments (DoE) is required to identify the most influential factors on failures. Print direction, furnace, position in furnace, debinding/sintering atmosphere, and stress are chosen as the study factors. A remarkable number of samples should be produced to investigate the effect of study factors in detail. However, considering the manufacturing costs and the production line capacity, random sampling and positioning are chosen for producing the specimens. Two types of self-loading specimens, bending and tension samples, are printed. Due to the design flexibility of AM technology, different stress values can be imposed on the samples. The samples are printed and debound in two furnaces under an N_2 or H_2 atmosphere. The damaged specimens are documented, and a sensitivity analysis is performed to rank the importance of study factors in debinding/sintering failure.

The failure probability during debinding/sintering is predicted using the Weibull equation based on the collected data. To calculate stress distributions for arbitrary geometries, static FE simulations are conducted, and a simulation-based Weibull model is proposed for predicting the probability of debinding/sintering failure. The accuracy of the model is assessed through validation with various geometries.

4.3 Numerical Simulation of Sintering Deformation

The methodology to model sintering deformation is described in the present section. At first, the SOVS approach is explained. The second subsection introduces a data-driven simulation framework based on SOVS.

4.3.1 Skorokhod and Olevsky Viscous Sintering

As discussed in Sec. 2.4, SOVS phenomenological model has been used for the prediction of sintering deformation of parts manufactured by MIM or die-casting technologies. Considering the major differences between MBJ technology and the other mentioned manufacturing processes, the SOVS model should be evaluated for MBJ parts. To make use of the SOVS model, several material model parameters should be calibrated. Firstly, GPD is considered a constant value and estimated by averaging between measured densities of previously manufactured parts. Dilatometry sintering is carried out for a given thermal cycle to model the TEC and the sintering stress. Eq. 2.14 and Eq. 2.15 show that another important physical property to capture the sintering deformation of power aggregate is apparent viscosity. At this stage, a cyclic loading experiment is performed to measure apparent viscosity.

With DSC, the Specific Heat Capacity (SHC) of a fully dense material is determined with respect to temperature. Eq. 2.20 shows that Thermal Diffusivity (TD) should be known to measure thermal conductivity. TD of a fully dense material is determined by LFA. Using the calibrated material model, two specimens are simulated, and the final sintering deformations are compared with experiments. Additionally, a sensitivity analysis of the physical parameters in the model is performed to detect and rank the influence of the parameters on simulation results, with a focus on deformation and density. The results from sensitivity analysis and the comparison between simulation and experiments enlighten the required research areas for optimizing the model.

4.3.2 Data-driven Simulation of Sintering Deformation

Considering the technological readiness level of MBJ and the spotted research areas from in-depth analysis of the SOVS approach, a Data-Driven Numerical Simulation (DDNS) approach is developed to predict the deformation and density of MBJ components during/after sintering. The introduced constitutive equations in Sec. 2.4.2 employed for the SOVS model remain the governing equations for the DDNS approach. However, the determination of GPP, TEC, sinter stress, and apparent viscosity is accomplished through a wider range of laboratory measurements. Moreover, a method to measure sintering anisotropy is introduced and integrated into the material model.

Pure experimental data can be used to anticipate the density and dimension of green pars. In this respect, standard cubes are printed with two different distributions across the print chamber. The cubes are distributed in such a way that they cover nearly the entire print chamber. After printing, the mass and dimensions of the cubes are measured. The collected data at various locations are treated as individual nodes for calculating the variation of green part density and dimensions across the print chamber. A continuous field is then created through 3D interpolation between the nodes, which is termed the Green Part Property Field (GPPF) in this study.

Dilatometry experiments with specimens printed in two directions (build and print head directions) are performed with seven distinct sinter cycles. These experiments are used to develop a more general material model. For determining apparent viscosity, the design flexibility of AM is exploited, and apparent viscosity is indirectly measured by beam deflection analysis.

Even though the proposed material model is constructed on experimental data, and the accuracy of the model generally increases with the number of collected data, the following facts should be noticed: Primarily, time and economic constraints limit the number of experiments that can be conducted. Additionally, laboratory machines may have different capacities, nature, and functionality, which could lead to results that differ from those in the workshop. Therefore, the model created based on laboratory measurements will be further refined with experimental data gathered from the workshop. Finally, the accuracy of the proposed model will be evaluated by simulating two specimens.

4.4 Compensation for Sintering Deformation

In order to achieve precise dimensional accuracy in MBJ parts, it is necessary to develop a compensation procedure for sintering deformations. The first step of this process involves introducing an algorithm that utilizes numerical simulations to compensate for predicted deformations iteratively.

The algorithm should be both computationally efficient and compatible with the developed simulation methods of sintering deformation. Specifically, the algorithm utilizes the predicted deformations from simulations to invert the deformation vectors, creating a pre-deformed configuration. This pre-deformed configuration is then simulated once again, and the results are compared with the target geometry, with the process continuing until a convergence criterion is met.

However, considering the numerous influencing factors on sintering deformation and the potential limitations of FE simulations (such as their degree of precision being dependent on assumptions, simplifications, boundary conditions, and element size and type [213, 214]), numerical-based compensation methods may not be sufficient on their own. Therefore, an experimental-based approach can also be employed to achieve tighter dimensional tolerances. This approach involves utilizing deviation vectors from the numerical simulations to refine the experimental procedure. This minimizes the impact of external factors that may influence the final product and are not captured in numerical models. Finally, MBJ samples are produced and tested to validate the effectiveness of these two approaches.

The methodology proposed for achieving the stated objectives is presented in Fig. 4.3. A detailed explanation of the procedure for each objective is provided in distinct sections, with Sec. 5 describing the model for predicting debinding/sintering failure, Sec. 6 elaborating on the numerical simulation of sintering deformation, and Sec. 7 outlining the framework for compensating for sintering deformation.

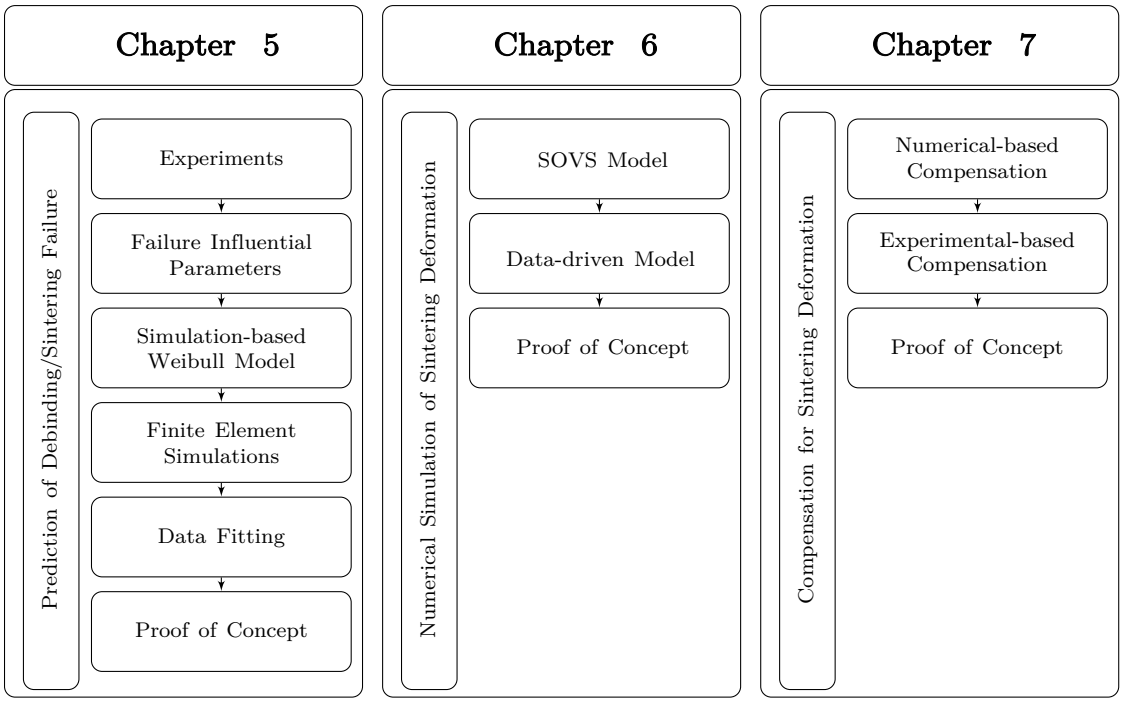

Figure 4.3 The proposed methodology for achieving the objectives of the thesis.

Chapter 5

Prediction of Debinding/Sintering Failure

The first section of this chapter outlines the experimental procedures used to identify the stage of the debinding/sintering process at which failure occurs. Subsequently, experiments with self-stressing samples are conducted to identify factors that influence failures. The second section presents an analysis of the results obtained from self-stressing specimens, through which parameters that significantly affect failure are identified with a sensitivity analysis. The third section expands on the triaxial form of the Weibull equation to consider the effect of process parameters. The fourth section develops a modified Weibull model to be compatible with the extracted stresses from numerical simulations. Stress values are determined through FE simulations for specimens available in the dataset, and the Weibull model parameters are subsequently derived. In the proof of concept section, the effectiveness of the proposed method is tested using two different geometries, followed by a concluding statement.

5.1 Experiments

5.1.1 Identification of Failures' Stage

Thermo-Optical Measurement (TOM) experiments are conducted to monitor and detect the time/temperature at which failures occur during debinding. Subsequently, TGA experiments are performed on green parts to confirm whether the identified failures correspond to the removal of the binder.

Insitu Thermo-optical Observations

A bending geometry (See Fig. 5.3b) is chosen for TOM and debound in a graphite furnace under H_2 with a 2 K/ min heating rate. Fig. 5.1a depicts the specimen at RT in a furnace equipped with thermo-optical recording. Owing to constraints related to the size of the recording tunnel, only one of the specimen's arms is entirely visible. In contrast, only the base of the arm and its connection with the middle bar can be captured for the other arm. During the heating process, one of the arms is broken at 204 °C, while the other fails at around 300 °C (See Fig. 5.1b and Fig. 5.1c, respectively).

Thermal Gravimetric Analysis

A small portion of a green part with a starting mass of 98.42 mg is prepared for TGA. Fig. 5.2 illustrates the mass change during a sintering cycle with an included debinding stage. The sintering cycle is also superimposed in the figure.

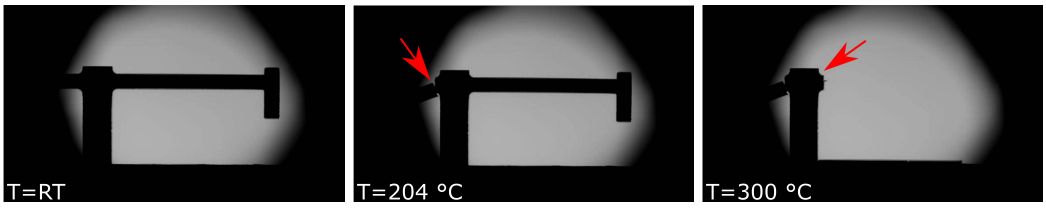

(a) (b) (c)

Figure 5.1 In-situ TOM observation of a bending geometry with $D_{arm} = 2\,\text{mm}$, $L_{arm} = 25\,\text{mm}$, and $B_m = 3\,\text{mm}$, (a): at RT, (b): broken left arm at 204 °C and, (c): broken right arm at 300 °C.

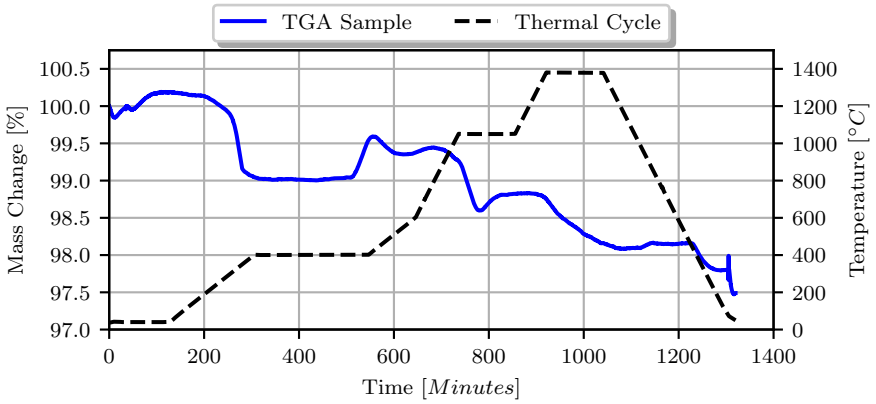

Figure 5.2 Mass change of a green part with respect to time, superimposed with a sintering cycle.

The presented data illustrates that the tested specimen undergoes a mass loss of approximately 1 % before reaching a temperature of 400 °C. A further notable mass drop occurs at the isothermal sintering stage, with the final mass loss of the sample being around 2 %. One theory to explain the failures observed in Fig. 5.1 is the reduction in strength of the green parts during debinding, making the parts more prone to damage [45, 78, 215, 216]. The TGA results can confirm this theory by indicating the mass loss values that occur around 400 °C, which is primarily attributed to the removal of the binder.

Based on the analysis of TGA and TOM observations, it has been inferred that failures take place during the debinding stage, prior to the commencement of sintering. As a result, henceforth, the term ”debinding/sintering failure” will be replaced by ”debinding failure” in this thesis.

5.1.2 Self-stressing Specimens

The upcoming goal of this section is to identify the effect of selected process parameters on part defects due to debinding. Two types of geometries are designed for this study: a tensile-type specimen and a bending-type specimen. Four process parameters: print direction, sintering furnace, debinding/sintering atmosphere, and furnace level are considered. Part stress induced by self-weight is added as an additional parameter. The input parameters are further explained below.

Stress

Different stress values can be designed by varying the self-weight by changing the samples' geometrical size and attribution. No external load is applied to the geometries. The specimens are designed as follows:

- **Tensile specimen:** The attributes and dimensions of the tensile specimen are shown in Fig. 5.3a. Two geometrical parameters, the diameter of the smallest neck D_n and the volumetric parameter V_t, can be set to create different stress values. The normal stress on the neck area is calculated by:

$$\sigma = \frac{\rho g V_t}{\pi (0.5 D_n)^2}, \tag{5.1}$$

  where ρ is the green density, g is the gravitational acceleration, and $V_t = \pi\, h_t\, (0.009)^2$ [217]. The considered GPD is $4570\,\mathrm{kg\,m^{-3}}$, which is the average GPD of experiments, presented later in Sec. 6.2.1. By assigning values between 2 mm and 4 mm to D_n and changing V_t between $650\,\mathrm{mm^3}$ to $7800\,\mathrm{mm^3}$, 18 different stress values from 2 kPa to 70 kPa on the neck area are generated.
- **Bending specimen:** The bending specimens are designed to form a more complex uniaxial stress state to expand the data set. The bending specimen possesses two cantilever-like arms with hanging masses at the end of the arms to impose the bending moment. By controlling three geometrical parameters shown in Fig. 5.3b, a wide range of stress values can be generated at the connecting points of each arm. The diameter of the arm D_{arm}, the length of the arm L_{arm}, and the width of the hanging mass B_m are the geometrical parameters. The maximum normal stress caused by the bending moment is analytically calculated by:

$$\sigma_{max} = \frac{32\rho g [L_{arm} - 0.004][\frac{V_{arm}}{2} + V_m]}{\pi D_{arm}^3}, \tag{5.2}$$

  with

$$V_m = 0.002 \cdot \left[0.005 B_m + 0.5\pi (0.5 B_m)^2\right],$$

  and

$$V_{arm} = \pi (0.5 D_{arm})^2 (L_{arm} - 0.004),$$

  where V_m is the volume of the hanging mass at each end of the arm, and V_{arm} is the volume of the arm [217]. 22 various bending specimens are produced, by changing D_{arm} between 2 mm and 5 mm, varying L_{arm} between 10 mm and 20 mm, and B_m between 0 mm and 8 mm. With these combinations, the maximum stress at the root of the arms alternates between 1 kPa and 60 kPa.

Part Orientation

The properties of binder jetting parts (e.g., bending strength [202], shrinkage [94], and dimensional accuracy [28]) are dependent on the part orientation and, therefore, anisotropic. The anisotropic behavior of green parts in the course of debinding is also reported by [83] and [84]. Therefore, part orientation is considered to be one of the process parameters in this study. However, the disparity in the property of MBJ parts between the X and Y directions is relatively small compared to the difference observed between the parts printed in X and Z directions [40, 94, 203, 218]. This allows to limit the number of parameters, and it is assumed that the green part property is the same in X and Y directions; thus, the specimens are manufactured just in X and Z directions (Refer to Fig. 4.1 to see the used convention). The orientations for tensile and bending specimens are shown in Fig. 5.4a and Fig. 5.4b, respectively. All specimens are printed with an integrated Depowdering Protective Cage (DPC) to minimize the risk of potential damage during the depowdering procedure [219].

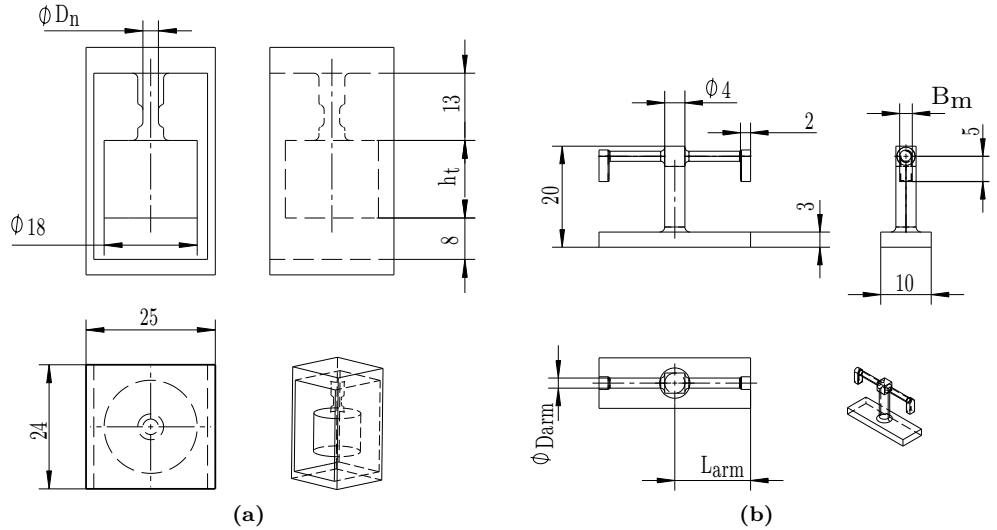

Figure 5.3 Technical drawing of (a): tensile specimen and (b): bending specimen. For each specimen, the provided isometric view is displayed at a scale that is half the size of the other three given views. All dimensions are given in mm.

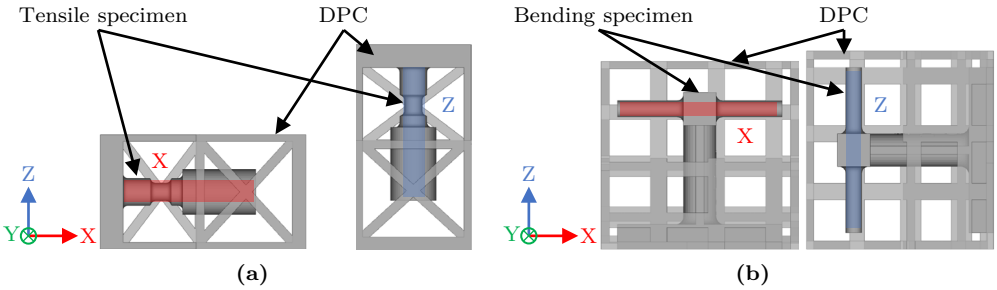

Figure 5.4 The convention used to define the orientation of (a): tensile specimens and (b): bending specimens.

Sintering Furnace and Debinding Atmosphere

The described F1 and F2 furnaces in Sec. 4.1 are utilized for the debinding experiments. In the workshop, F1 can be operated under 100-Vol.% H_2 or 100-Vol.% N_2, while F2 works only with 100-Vol.% N_2.

The sintering cycle for debinding failure experiments is chosen to be shorter than the normal sintering cycle (See Fig. 5.5). As observed in Sec. 5.1.1, the failures are expected to occur at temperatures below and around 400 °C, where the main portion of the binder is burnt off. Therefore, analog to the regular sintering cycles, the furnace is heated up to 400 °C and held for two hours. After the holding time, the debound green parts (so-called brown parts) are extremely fragile. In the case of unloading the brown parts directly after debinding, there is a high risk of damaging the parts and influencing the experiments. Thus, the parts are directly heated up to 1050 °C, at which initial particle-particle bonds take place, and the strength of the specimens increases. Without any holding time, the furnace is then cooled down immediately.

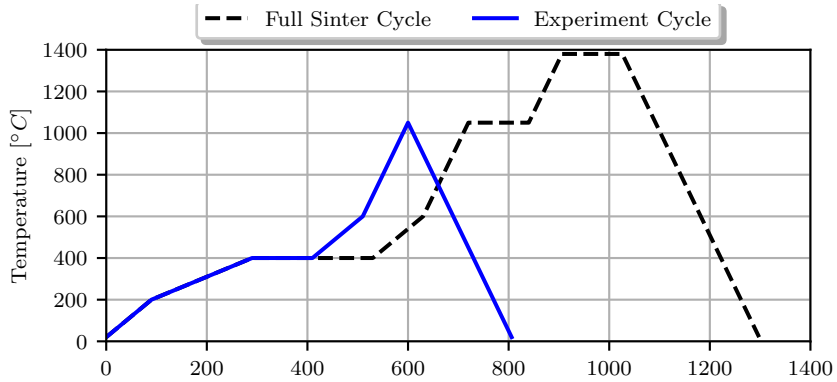

Figure 5.5 The used debinding cycle vs. a typical sintering cycle for SS316L parts in MBJ.

Level of Furnace

To evaluate whether the temperature gradient inside the furnaces has any effect on debinding failures (if any temperature gradient is present at all), the specimens are placed on different levels of the interior chamber of the furnaces. Each furnace has six levels, equidistantly distributed at height with the same surface area for part positioning. Three levels, i.e., 1, 3, and 5, are chosen for the failure experiments (See Fig. 4.2).

Results

In total, 853 specimens have been prepared for the debinding failure analysis. Each specimen has five input parameters mapped into a numerical range (See Tab. 5.1). After recording the failure status of the specimens, a binary failure indicator is assigned to the specimens: +1 for the failed specimens and 0 for the intact ones.

Input parameter	Variable type	Range of values	Mapped values
Stress	Continuous	[0, +70] kPa	[0, 1]
Direction	Discrete	X, Z	{0, 1}
Furnace	Discrete	F1, F2	{0, 1}
Atmosphere	Discrete	H_2, N_2	{0, 1}
Level of furnace	Discrete	1, 3, 5	{0, 0.5, 1}

Table 5.1 Variable type and value range of the input parameters.

For example, Fig. 5.6 illustrates two failed tensile and bending specimens. The Scanning Electron Microscope (SEM) images of the broken cross-sections of two bending and tensile specimens, depicted in Fig. 5.7, display evident particle bonds and neck formation. Thus, the assumption that failure occurs before the onset of sintering is validated, and the observed brittle fracture can be associated with the weak interparticle bonds that exist before sintering [220–222].

(a) **(b)**

Figure 5.6 Two broken specimens (a): a tensile specimen and (b): a bending specimen.

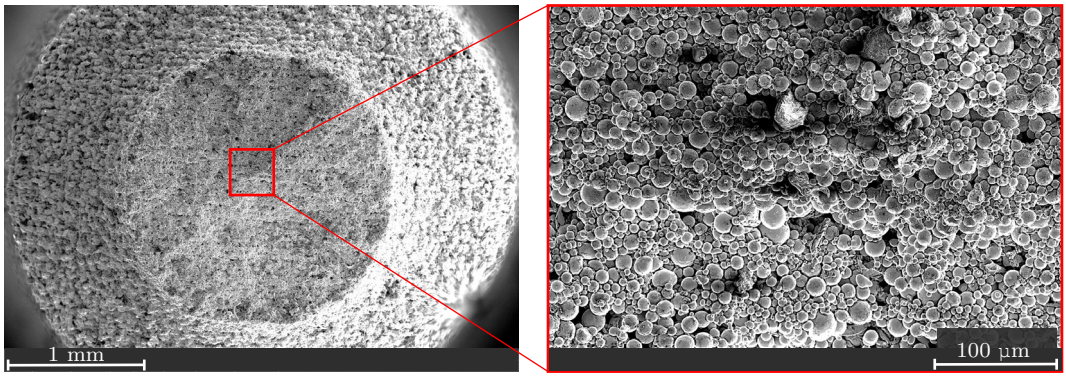

(a)

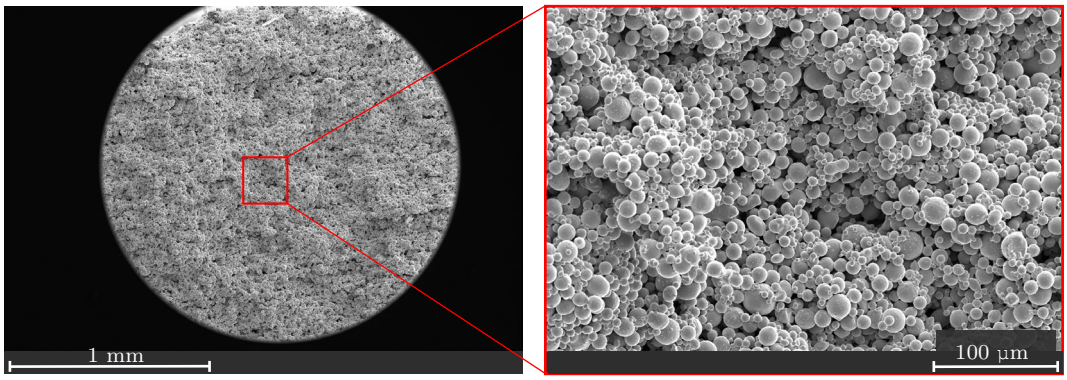

(b)

Figure 5.7 Fracture surface of (a): a tensile specimen and (b): a bending specimen.

Fig. 5.8 plots the distribution of the collected data, excluding stress. To interpret the distribution, the number of specimens distributed with respect to each process parameter can be compared directly with any desired parameter on off-diagonal plots of the matrix. The diagrams on the matrix's main diagonal show the total number of specimens sorted by the values of a single parameter. For instance, in total, 469 specimens are manufactured in the X direction, while 384 in the Z. 450 specimens are debound under H_2, whereas 418 parts with N_2. Among the produced parts in the X direction, 296 remain intact.

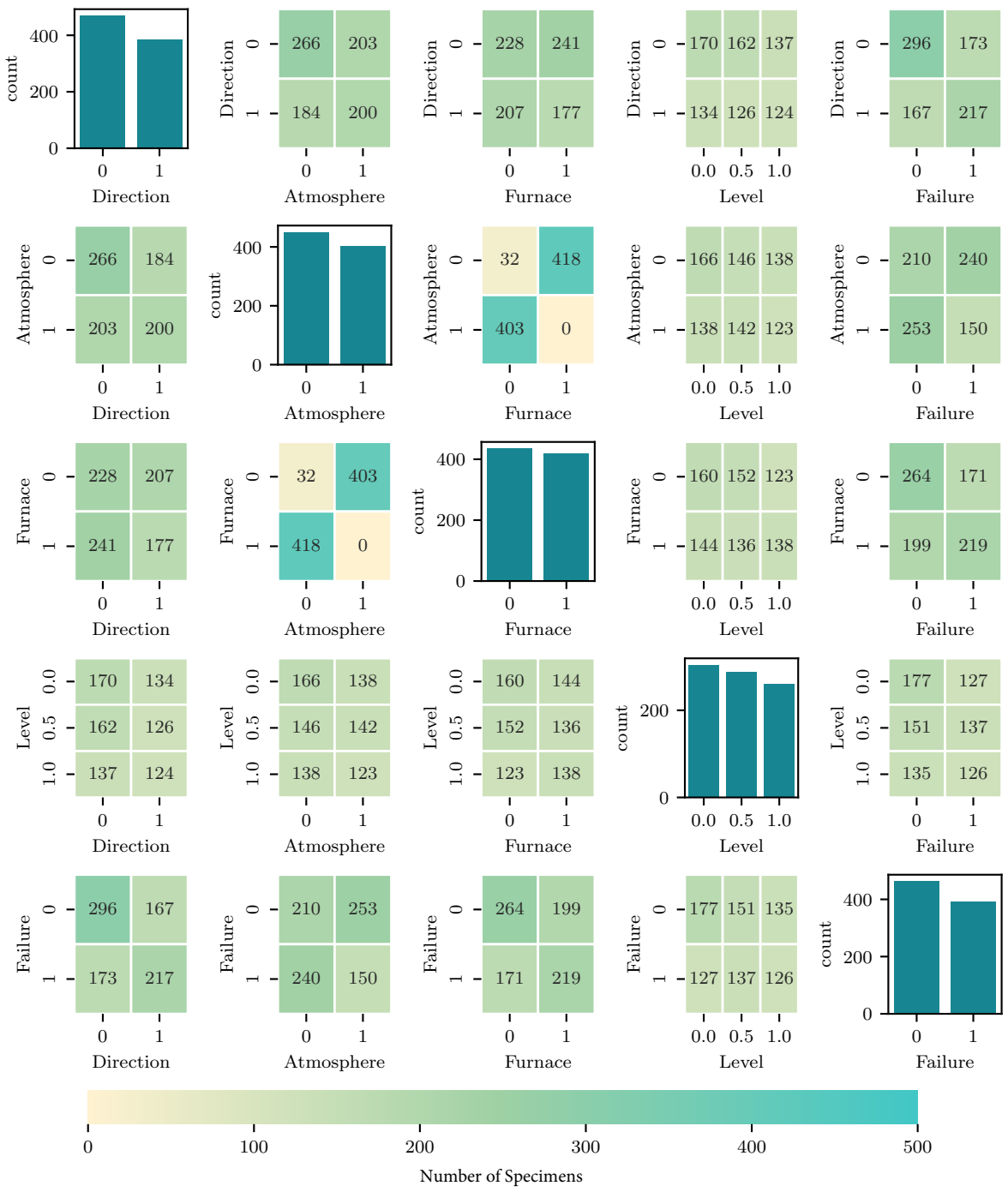

Figure 5.8 Symmetric matrix illustration for the distribution of specimens with respect to each input parameter and the number of broken/intact parts sorted by the parameters.

An unbalanced distribution between the furnace and the atmosphere is observed. Because of the following reasons, the distribution is not uniform:

- The collected data shows a strong dependency between the furnace and the atmosphere. Since F2 is solely operating with N_2, to balance the data, the main portion of specimens in F1 is debound under H_2.

- The design exploration and sampling are done with respect to the available capacity of the machines in the workshop. In this study, the samples are randomly chosen and tried to be evenly distributed. Furthermore, the specimens with higher stresses are more prone to fail during depowdering, leaving fewer specimens for further debinding. Consequently, re-balancing nonuniform distribution is complex, and using typical sampling methods such as Latin Hypercube is not plausible [223, 224].

5.2 Failure Influential Parameters

Tab. 5.2 reveals the correlation ρ_{cor} between the input parameters and the debinding failure. However, the conventional correlation analysis is generally valid for properly distributed samples. On the contrary, Elementary Effect (EE) method, or Morris's one-at-a-time method, can deliver global sensitivity results, even with an unbalanced distribution of the collected data [225, 226]. To rank the input parameters by their importance, the parameters are assessed by the absolute value of EE sensitivity $\hat{\mu_i}$. Taking the $\hat{\mu_i}$ values and the strong relation between "Furnace" and "Atmosphere" into account, stress and print direction are considered the most vital factors for debinding failure.

Input parameter	**Values**	ρ_{cor}	$\hat{\mu_i}$
Uniaxial normal stress	[0, +70] kPa	0.50	4.47
Direction	X, Z	0.20	0.44
Furnace	F1, F2	0.13	-0.14
Atmosphere	H_2, N_2	-0.16	-0.35
Level of furnace	1, 3, 5	0.05	0.03

Table 5.2 The sensitivity of debinding failure to the input parameters.

Fig. 5.9 plots the failure rate of specimens with respect to stress and grouped by the print direction. The specimens printed in the X direction show a more clear pattern of failure rate with increasing stress.

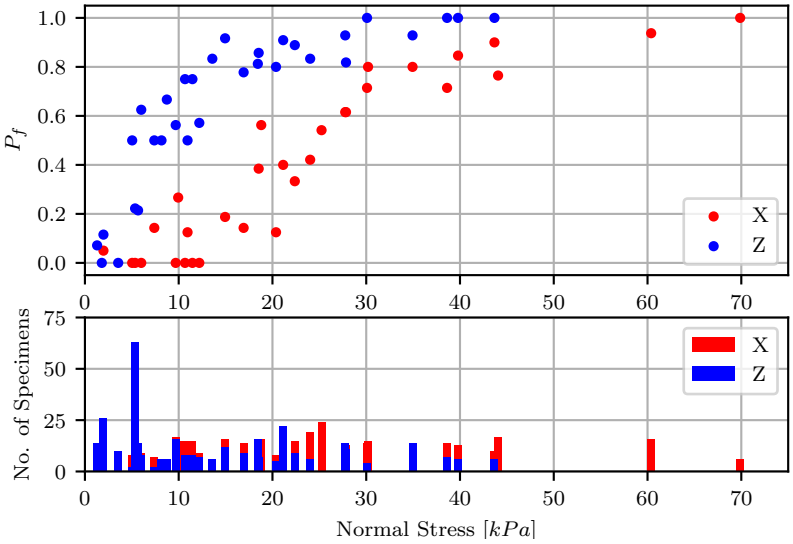

Figure 5.9 The failure rate (above) and number of studied specimens (below), grouped by print direction.

5.3 Simulation-based Weibull Model

As seen in Sec. 5.1.2, besides stress, other process parameters show an impact on the failure rate of specimens. However, the conventional Weibull only considers stress as the input and allows data fitting by three parameters (σ_{sp}, m, σ_u). Nonetheless, by rewriting the conventional form of the 2-p Weibull CDF into a linear combination form, more input parameters can be inserted into the function. Let

$$\begin{cases} x_1 = ln(\sigma) \\ m = \omega_1 \\ \sigma_{sp} = exp\left[-\dfrac{\omega_0}{\omega_1}\right], \end{cases} \tag{5.3}$$

then Eq. 2.1 can be rewritten as:

$$P_f = 1 - exp\,[\,-V(\,exp[\omega_0 + \omega_1 x_1]\,)\,]\,, \tag{5.4}$$

where x_1 is the nonlinear transformation of stress σ, while ω_0 and ω_1 represent the combination and transformations of m and σ_{sp}. In a vector form Eq. 5.4 can be presented as:

$$P_f = 1 - exp\left[\,-V(\,exp\left[\omega^{\mathbf{T}}\mathbf{x}\right]\,)\right], \tag{5.5}$$

where $\omega = [\omega_0, \omega_1]^T$ and $\mathbf{x} = [1, x_1]^T$. The vector form is preferable since further input parameters can be added to input vector $\mathbf{x}$ as additional weights in ω. The result of debinding experiments indicates that the print direction of the specimens should be considered the second most important input parameter for the prediction of debinding failure. This input parameter contains two discrete values $\{"X", "Z"\}$, which are mapped to $\{0, +1\}$. The mapped values $\{0, +1\}$ can be regarded as an indicator of the angle between the stress vector and the XY plane (See Fig. 5.10). The print direction indicator x_2 is defined as:

$$x_2 = \frac{\theta_\sigma}{\frac{\pi}{2}},\ x_2 \in [0, 1],$$

where $\theta_\sigma \in [0, \frac{\pi}{2}]$ is the absolute angle between the stress vector and the XY plane. $x_2 = 0$ refers to the stress vector which lies in the XY plane, while $x_2 = 1$ means that the stress vector is the same as or opposite to the Z direction.

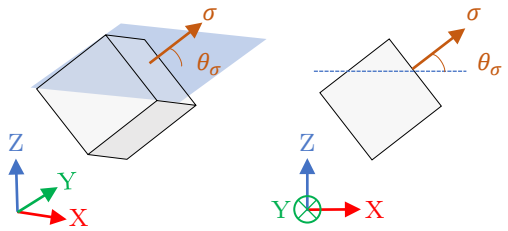

Figure 5.10 Three-dimension and two-dimension visualization of θ_σ for one principal stress in a differential volume.

Eq. 2.3 proposes to include a stress threshold, above which there is a possibility of failure. Thus, the smallest normal stress of specimens with a failure rate of higher than 10 % is probed from Fig. 5.9. It is observed that the stress threshold for the specimens printed in the XY plane is around 7.4 kPa, while for those in the Z direction, the threshold drops to 2 kPa. The input parameter x_1 can then be formulated as

$$x_1 = \begin{cases} ln(\sigma - \sigma_u),\ \sigma > \sigma_u \\ -\infty \qquad\quad ,\ \sigma \leq \sigma_u, \end{cases}$$

where the threshold stress σ_u is defined by:

$$\sigma_u = 7.4(1 - x_2) + 2.0,\ x_2 \in [0, 1],$$

which enables a linear change between the threshold within the XY plane and in the Z direction. The threshold performs as another layer of nonlinear transformation of stresses, representing the effect of print direction.

Due to the complex shape of MBJ components, the stress states should be obtained by FE simulation. Hence, the prediction model should be developed based on simulations. By assuming that the stress is uniformly distributed within each element, the integral form Eq. 2.4 is presented as:

$$P_f = 1 - exp\left[-\sum_{i=1}^{K} v_i \left\{\left(\frac{\sigma_{1_i}}{\sigma_{sp}}\right)^m + \left(\frac{\sigma_{2_i}}{\sigma_{sp}}\right)^m + \left(\frac{\sigma_{3_i}}{\sigma_{sp}}\right)^m\right\}\right], \tag{5.6}$$

where K is the number of elements for each specimen. The σ_{1_i}, σ_{2_i}, and σ_{3_i} are the averaged principal stresses, read in the centroid of the ith element. By transformation of input parameters, Eq. 5.6 can be rewritten as:

$$P_f = 1 - exp\left[-\sum_{i=1}^{K} v_i \left\{exp[\omega \mathbf{x}_{1_i}] + exp[\omega \mathbf{x}_{2_i}] + exp[\omega \mathbf{x}_{3_i}]\right\}\right], \tag{5.7}$$

where $\mathbf{x}_{1_i}$, $\mathbf{x}_{2_i}$, and $\mathbf{x}_{3_i}$ are the input vectors corresponding to the averaged principal stresses, while v_i is the volume in the ith element. By introducing $\phi_i = v_i \left(\sum_{j=1}^{3} exp[\omega \mathbf{x}_{j_i}]\right)$ as an element-wise importance factor, Eq. 5.7 is compacted with:

$$P_f = 1 - exp\left[-\sum_{i=1}^{K} \phi_i\right]. \tag{5.8}$$

The element-wise importance factor ϕ_i is used to help identify failure-prone zones. This factor varies in a range of [-inf, 0], making interpretation difficult. Given in Eq. 5.9, the equivalent element-wise importance factor ψ_i is presented as a general form of ϕ_i which varies within the range of [0, 1]:

$$\psi_i = 1 - exp[-1000\phi_i]. \tag{5.9}$$

ψ_i is introduced as Failure Indicator (FI) for an equivalent part with a volume of 1 cm^3.

5.4 Finite Element Simulations

The tensile and bending specimens are discretized and simulated with the commercial FE solver Abaqus/CAE 2020. The stress states on the elements are extracted and can be regarded as input parameters for data fitting. To reduce the computational cost, only the area of interest in the parts is modeled. For the tensile specimens (See Fig. 5.11a for example), only the neck of the specimens is simulated. The mass under the neck is substituted by force F_{sub} at the lower surface of the neck.

Similarly, for the bending specimens (See Fig. 5.11b), only one arm of each specimen is modeled, and the symmetry boundary condition is applied. The weights causing the bending moment at the end of the arms are replaced by an equivalent force F_{sub}.

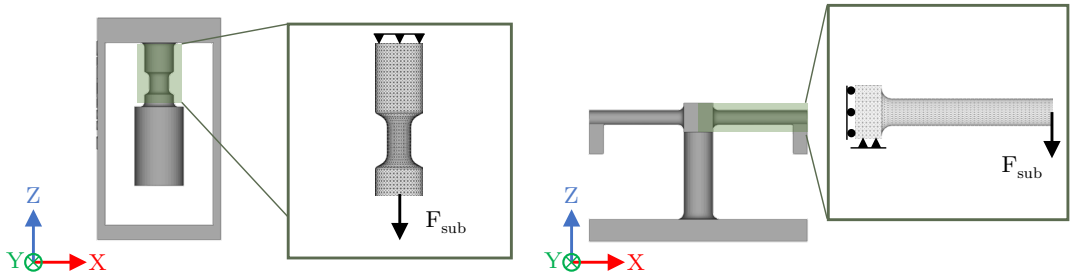

(a) (b)

Figure 5.11 The FE model of a typical (a): tensile specimen and (b): bending specimen.

The varied surface loads on the specimens are calculated with the determined GPD of $4570\,\mathrm{kg\,m^{-3}}$. Apart from the substitute load of the weights and the self-weight of the specimens, no other load is considered. To avoid stress calculation inaccuracies due to the element sizes, the adaptive re-meshing technique is utilized by enabling the Mises stress error indicator MISESERI in ABAQUS/CAE [227, 228]. Second-order tetrahedral elements with an initial seed size of 0.3 mm are used for meshing.

Analog to the manufactured parts, 40 types of specimens (18 tensile and 22 bending specimens) are simulated. For each simulation, the stress tensor $\boldsymbol{\sigma}_i$ at the centroid of each element i $(i = 0, 1, ..., K)$ is calculated. Principal stresses σ_{1_i}, σ_{2_i}, and σ_{3_i} and their angle to the XY plane $\theta_{i\sigma_1}$, $\theta_{i\sigma_2}$, and $\theta_{i\sigma_3}$ are then derived from $\boldsymbol{\sigma}_i$. Together with the volume v_i of each element, the principal stresses and the angle values are exported to the Weibull model as input parameters.

5.5 Data Fitting

To determine the ω weights and data fitting, the negative log loss function can be utilized, considering the nature of the probability prediction problem [229]. For a prediction model $P_f(\mathbf{x})$, its point-wise error at point $(\mathbf{x}_n, y_n)$ is:

$$e_n = e(\mathbf{x}_n, y_n) = -\left\{y_n\, ln\left[P_f(\mathbf{x}_n)\right] + (1 - y_n)\, ln\left[1 - P_f(\mathbf{x}_n)\right]\right\}. \tag{5.10}$$

Its loss function is then

$$\begin{aligned} E &= \frac{1}{N}\sum_{n=1}^{N} e_n \\ n &= 1, 2, ..., N, \end{aligned} \tag{5.11}$$

where N is the number of data points collected. By plugging Eq. 5.8 to Eq. 5.11, the log loss function for simulation-based Weibull is given as:

$$E(\mathbf{w}) = -\frac{1}{N}\sum_{n=1}^{N}\left\{y_n\, ln\left[1 - exp\left[-\sum_{i=1}^{K}\phi_i^n\right]\right] + (1 - y_n)\left(-\sum_{i=1}^{K}\phi_i^n\right)\right\}. \tag{5.12}$$

The principal stresses, their angle with XY plane, and the volume of the elements from the simulations, along with the print directions of the specimens, construct the input vectors **x**. The information about the failure rate of each specimen is also available in the experimental dataset. Finally, the ω weights are determined by the minimization of Eq. 5.12 with the minimize function in SCIPY [230].

In order to mitigate the influence of potential outliers during the optimization process, the dataset is restricted to specimens that have been produced at least five times. The resulting weights, ω, are obtained as a solution to the optimization problem and are presented in Tab. 5.3.

ω_0	ω_1	ω_2
[−]	[−]	[−]
-6.0	0.8	1.2

Table 5.3 The determined weights ω of the input parameters in the optimization problem.

5.6 Proof of Concept

The validation process is performed with two geometries: a bending part with four inclined elements and a manifold geometry. The technical drawing of the 4-member part is shown in Fig. 5.12, and its dimensions are provided in Tab. 5.4. The members are marked from one to four, and each member experiences a different stress field at its root due to dissimilar lengths, angles, and masses at the tips. With the design, it is possible to collect more data within a single part and validate the failure probability with higher accuracy.

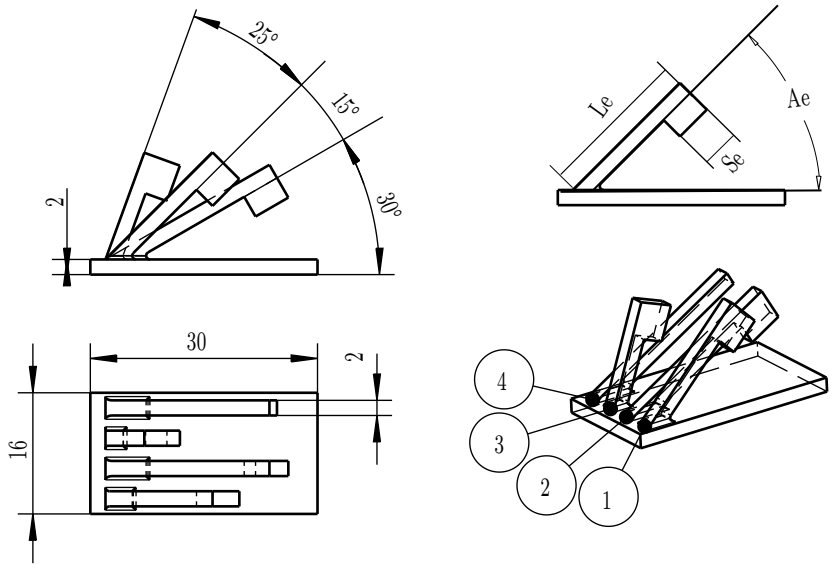

Figure 5.12 The 4-member part with dimensions. All dimensions are given in mm.

Member	**Length** L_e [mm]	**Angle** A_e [°]	**Side length** S_e [mm]
Member-1	20	45	5
Member-2	25	30	5
Member-3	15	70	5
Member-4	25	30	0

Table 5.4 The parametric dimensions of the 4-member part.

The FE model of the 4-member part is prepared as prescribed in Sec. 5.4. The resulting principal stresses along with the volume of the elements, are fed into the failure probability function Eq. 5.8. As shown in Fig. 5.15a, the part should be printed in two directions: in X and Z. Fig. 5.13 illustrates, the failure-prone zones identified by the equivalent element-wise importance factor ψ_i as well as the expected failure rate of each member, printed in the X and Z directions.

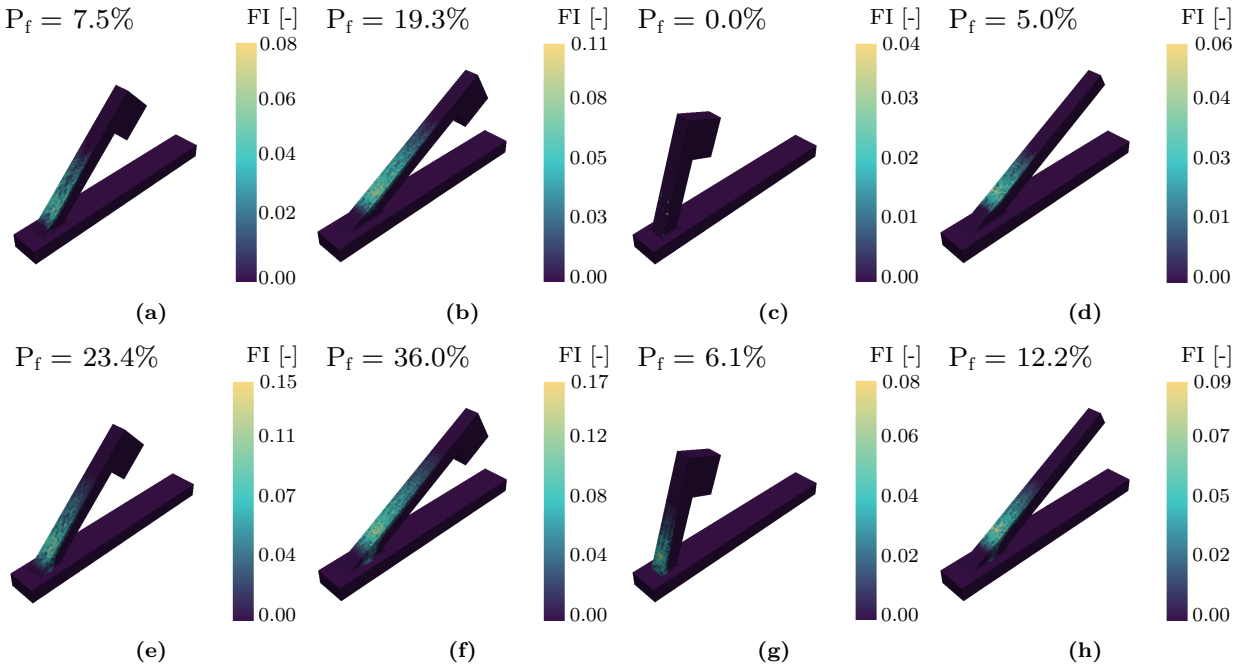

Figure 5.13 The failure probability as well as the detected failure-prone zones of each member, predicted by the simulation-based Weibull model for (a): member-1 printed in X, (b): member-2 printed in X, (c): member-3 printed in X, (d): member-4 printed in X, (e): member-1 printed in Z, (f): member-2 printed in Z, (g): member-3 printed in Z, (h): member-4 printed in Z direction.

As part of a further validation, the manifold geometry is studied to evaluate the accuracy of predictions on complex parts (See Fig. 5.14). The failure probability is calculated after simulating the geometry for both X and Z directions (See Fig. 5.15b for the print orientations). Fig. 5.16 shows the expected failure likelihood and the failure-prone zones.

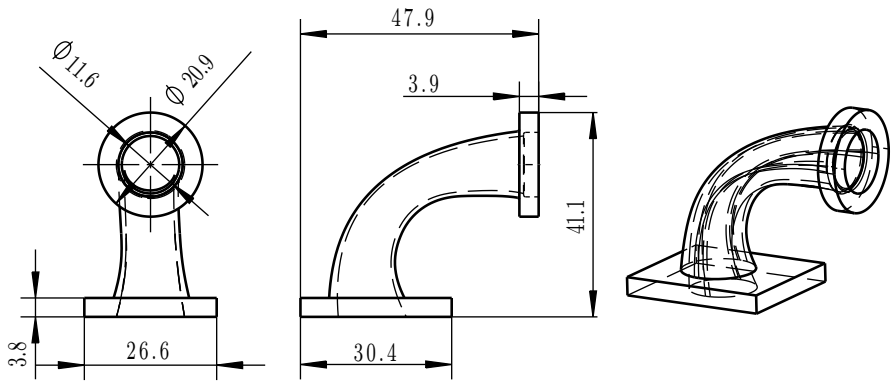

Figure 5.14 The manifold part with dimensions. All dimensions are given in mm. The isometric view presented is displayed at a scale of 2/3 compared to the other two provided views.

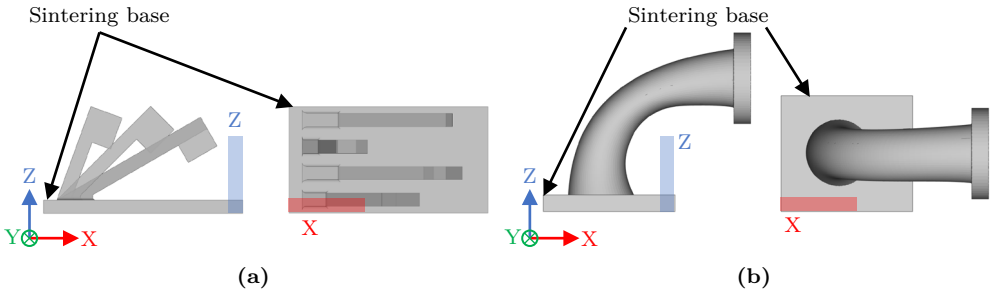

(a) **(b)**

Figure 5.15 The print direction of (a): 4-member specimen and (b): manifold specimen.

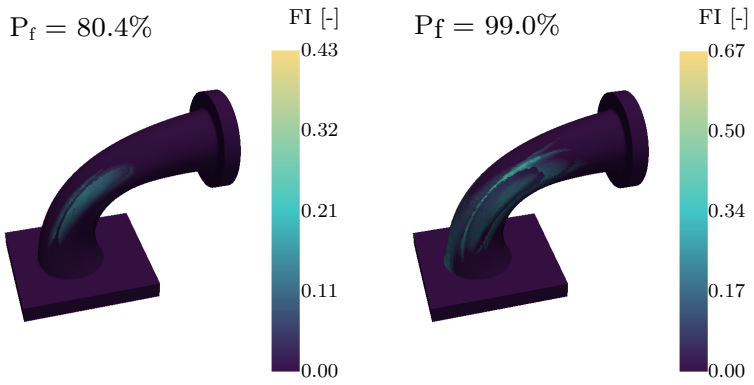

(a) **(b)**

Figure 5.16 The failure probability by the detected failure-prone zones predicted by the simulation-based Weibull model for the manifold printed (a): in the X direction and (b): in the Z direction.

To validate the simulation predictions, in total, 40 of the 4-member parts, 20 in Z and 20 in X, are printed. Due to the part's complexity, a limited number of specimens are manufactured for the manifold geometry. Ten manifold parts are printed in the X and Z directions (evenly distributed). All the parts are debound with the given cycle in Fig. 5.5 with H_2 atmosphere in Furnace F1 by positioning the parts on the designed sintering bases.

The broken members/parts are recorded after the heating cycle. Fig. 5.17a shows a sample with the broken member-2, whereas a broken manifold is shown in Fig. 5.17b. Tab. 5.5 weighs the observed failure rate against the anticipated failure likelihood by simulations.

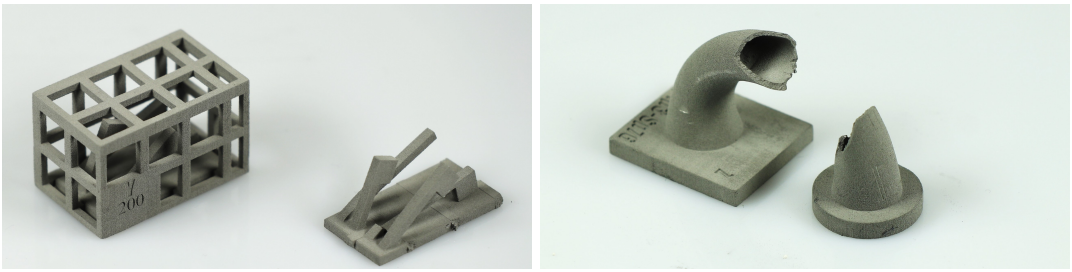

(a) **(b)**

Figure 5.17 (a): A bending 4-member part, with the broken member-2 (Left: a part in DPC, Right: a part after manually removing the DPC for better visibility) and (b): a broken manifold part printed in the Z direction.

Part	**Print direction**	**Predicted failure likelihood** [%]	**Reported failure rate** [%]
Member 1	X	7.5	0.0
	Z	23.4	10.0
Member 2	X	19.3	10.0
	Z	36.0	25.0
Member 3	X	0.0	0.0
	Z	6.1	0.0
Member 4	X	5.0	0.0
	Z	12.2	0.0
Manifold	X	80.4	60.0
	Z	99.0	100.0

Table 5.5 The documented failure rate of 4-member and manifold parts, compared with the predictions by the simulation-based Weibull model.

The comparison of prediction results from the simulation-based Weibull model with the experimental data illustrates that the model generally predicts a higher failure likelihood than observed in experiments. Specifically, no failure is reported in the experiments for the members with low expected failure probability ($P_f < 15\,\%$). However, for the manifold geometry printed in the Z direction, the expected and reported failure rates are in good agreement. Notably, the simulation-based Weibull model successfully identifies the failure-prone zones in cases where failures occur.

5.7 Conclusion

An in-situ TOM study was conducted on T-shape geometries, which revealed that failures occur during the early stages of the debinding process, even at temperatures as low as 200 °C. TGA measurements confirmed that a significant proportion of the binder burnt off at temperatures around 400 °C, resulting in the reduction of the green part's strength. Before achieving the initial stage of sintering (approximately 950 °C), weak inter-particle bondings and the remaining backbone from the binder keep the powder-void-skeletons together. When accompanied by high stresses, the poor strength of the brown parts endangers the failure-free debinding of MBJ components.

A DoE was implemented to determine the influencing factors on debinding failure. Stress state and intensity, print direction, furnace, position in the furnace, and the debinding atmosphere were identified as possible parameters which may affect debinding damage. Considering the limitations imposed by the manufacturing capacity and the required number of experiments, a random sampling method was used according to the available resources. Self-stressing specimens with varying uniaxial tensile stresses and bending stresses were printed in two different directions. Distributed on three levels in two different furnaces, the specimens were debound under two atmospheres: N_2 and H_2. After recording the debinding damage as binary values, the sensitivity analysis indicated that after stress, print direction plays a critical role in debinding failure. The Z direction specimens exhibited lower green part strength due to gaps in the build direction, making them more susceptible to failure when exposed to stress. A strong correlation was observed between the furnace and the atmosphere in the DoE, which complicated the interpretation of the sensitivity analysis.

To account for stress and print direction, a simulation-based Weibull model was developed. The manufactured geometries used in the DoE were modeled statically in a FE solver with gravity, and the resulting principal stresses and volume of each element were fed into the simulation-based Weibull model. The weight factors required for predicting failure likelihood in the model were determined by fitting to the experimental data.

The weight factors were employed to predict the failure likelihood of both simple self-stressing specimens and a manifold geometry. The experimental results showed that the simulation-based Weibull model overestimated the failure likelihood but correctly identified the failure-prone zones and expected regions of failure. To further validate the accuracy of the model, a larger number of validation experiments should be conducted to analyze the failure likelihood statistically. Furthermore, additional input parameters, such as the impact of the furnace and atmosphere, could be incorporated into the model to improve the accuracy of the predictions.

Chapter 6

Modeling of Sintering Deformation

This chapter is dedicated to developing an approach for the simulation of the sintering deformation of MBJ parts. In the first section, the SOVS model is employed, and its applications and accuracy are analyzed. Building on the analysis results, the second section introduces a data-driven approach based on the SOVS model.

6.1 Olevsky Sintering Deformation Model

This section begins with experiments to determine the material constants of the SOVS model. Subsequently, the SOVS material model is implemented in a FE framework, and two geometries are analyzed using the model. A sensitivity analysis is performed to identify significant material model parameters. Finally, an evaluation of the model is presented to specify the critical areas for the advancement of sintering deformation models.

6.1.1 Experiments

Considering the given equations in Sec. 2.4.2, dilatometry measurement, metallographic analysis, TOM, DSC, and LFA are crucial to determine the empirical material constants of the SOVS model. Each experiment is explained separately. The employed printer, PSD, print layer thickness, and curing temperature for the experiments of this section are listed in Tab. 6.1.

Printer	**PSD** [µm]	**Layer thickness** [µm]	**Curing Temp.** [°C]
ExOne Innovent	17 (D_{10}), 38 (D_{50}), 53 (D_{90})	50	180

Table 6.1 PSD and printing parameters, used for the SOVS experiments.

Dilatometer

The thermal expansion coefficient and the shrinkage behavior of MBJ cylindrical samples are measured by horizontal dilatometry. Two dilatometry experiments are carried out under 100-Vol.% H_2 atmosphere. The green part cylindrical samples are printed with their axes of symmetry parallel to the build direction with the dimension of $\varnothing$ 12 mm x 20.0 mm. The density of the green parts is measured by the Mass to Volume (MtV) method. The volume is calculated from the 3D-scan of each specimen. The average density is about 4820 kg m^{-3}. After a debinding stage, the samples are heated to 1385 °C and kept for 180 minutes. The heating and cooling rates after the debinding stage are 5 K/ min. The dimension change of specimens superimposed with the thermal regime is shown in Fig. 6.1 [188].

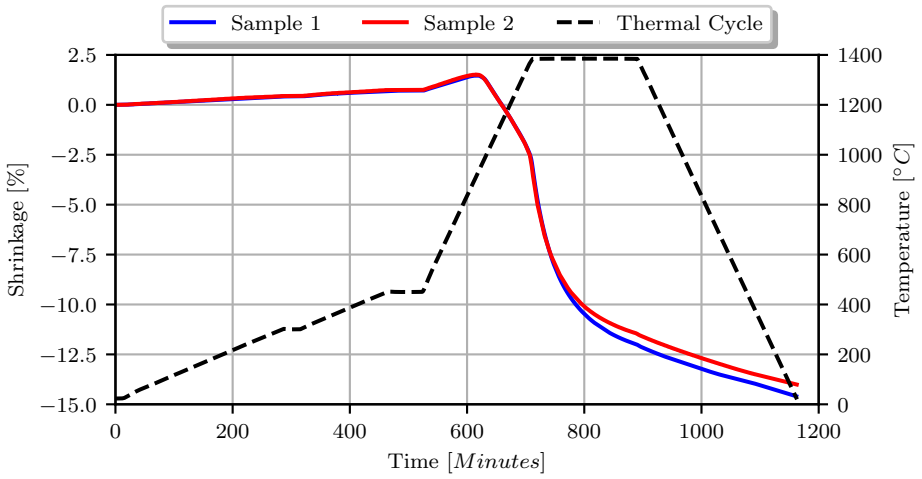

Figure 6.1 Shrinkage behavior of the printed cylinder specimens with the thermal cycle superimposed [188].

Metallographic Analysis

In order to capture the densification behavior and grain size evolution of sintering bodies in the course of sintering, further dilatometry experiments are performed under 100-Vol.% H_2 atmosphere. Cylindrical samples with the same size, printing direction, debinding cycle, and heating rate as those mentioned in 6.1.1 are heated to 1100 °C, 1200 °C, 1300 °C, and 1385 °C. After that, the samples are quickly cooled down to RT with a rate of 40 K/ min without any holding time.

First, the density of the samples after sintering dilatometry is determined by a MtV method. The volume is calculated from the 3D-scan of each specimen. For observing the porosity of the samples, Metallographic Analysis (MA) is performed. Proceeded by cutting, grinding, and polishing, the porosity/density of the samples is measured under a microscope. GS analyses are performed on the same specimens. After etching with Nital (5 %) solution, samples are inspected under the microscope. Using the linear line interception method prescribed by DIN EN ISO 643 [231], GS is calculated from the average of five measurements on each specimen. For the GS of the virgin powder at RT, an SEM is used [188] (See Fig. 6.2). The GS evolution with respect to temperature is demonstrated in Fig. 6.3.

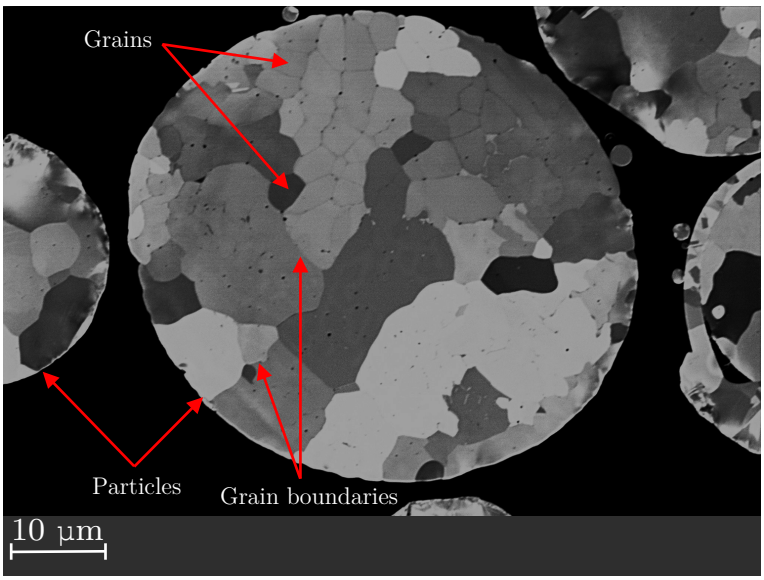

Figure 6.2 The grain structures inside the virgin powder particles.

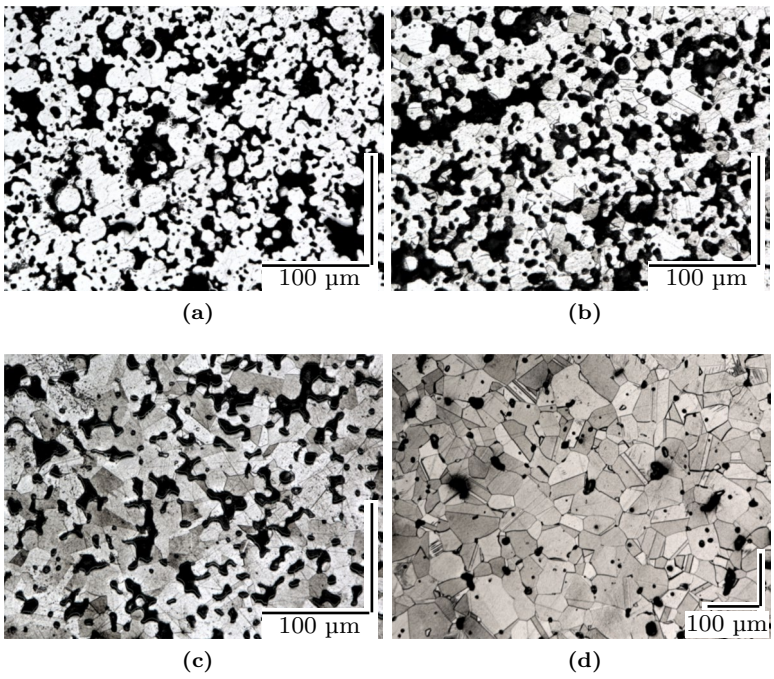

Figure 6.3 Microstructure evolution at (a): 1100 °C, (b): 1200 °C, (c): 1300 °C, and (d): 1385 °C [188].

Viscosity

Using a cyclic loading approach in a TOM apparatus, the uniaxial viscosity of the material is determined [156, 160, 175, 232]. For this purpose, with a heating rate of 5 K/ min, a cylindrical MBJ specimen (with a density of 4794 kg m^{-3}) is heated to 1395 °C; and a load of 1.15 N is applied and released on the specimen in cycles of 5 minutes. After measuring the shrinkage in radial and axial directions, the uniaxial (apparent) viscosity is determined, which is plotted in Fig. 6.4. Occurring liquid phase sintering and sudden densification complicate the calculations for temperatures above 1390 °C.

Temperature [°C]	GS [µm]	Porosity by MA [%]	Porosity by MtV [%]	Holding time [min]
21	5.0	40.0	40.8	0
1100	6.1	31.0	30.2	0
1200	20.5	29.0	30.0	0
1300	25.6	11.5	17.0	0
1385	44.6	11.1	15.3	0
1385	86.0	3.0	2.5	180

Table 6.2 The measured GS and porosity of the samples at different temperatures.

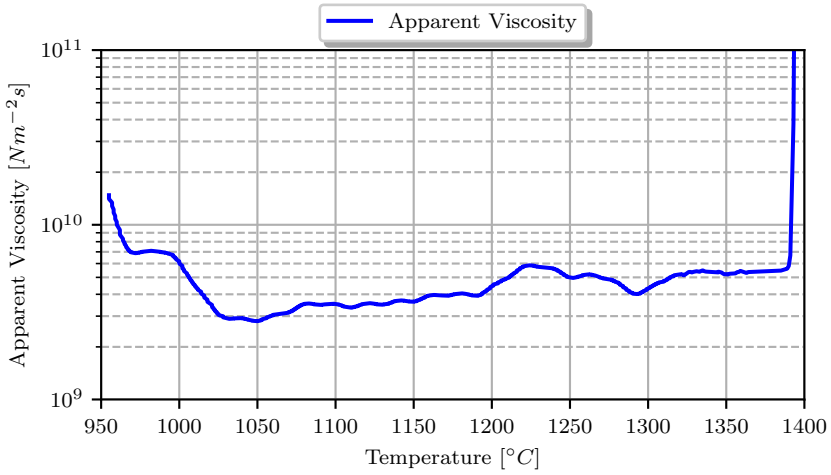

Figure 6.4 The measured apparent viscosity with temperature for SS316L [188].

Specific Heat Capacity

DSC is used to determine SHC with respect to temperature for fully dense materials. Five samples are heated up to 1000 °C with a rate of 15 K/ min under argon. By machining, the cylindrical sintered samples are sized to ⌀ 5 mm x 1 mm. The density of the specimens is measured by Archimedes' principle at RT, according to DIN EN ISO 2738 [233]. The average density is equal to 7810 kg m^{-3}. Fig. 6.5 shows the measured values. Due to the heating dynamics of the furnace in the range below 100 °C, the SHC values in this range were extrapolated to RT. Slight discoloration is observed on the surface of the samples after heating, which is a sign of an oxidation reaction. Because of the existing limitations for measurements above 1000 °C, SHC values are extrapolated later for simulation studies.

Thermal Diffusivity

TD is measured with LFA. Three sintering samples are machined to the size of ⌀ 12.8 mm x 2.2 mm. Using Archimedes' principle at RT (DIN EN ISO 2738), the average density is found to be 7770 kg m^{-3}. The TD values are determined for the samples at RT, 400 °C, 800 °C, 900 °C, 1000 °C, 1100 °C, 1200 °C, and 1300 °C. Fig. 6.6 shows the measured TD values.

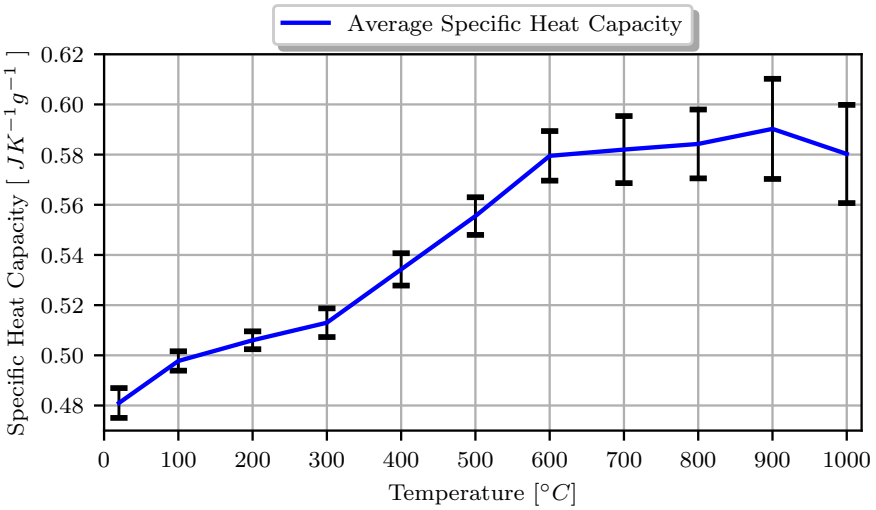

Figure 6.5 The average of the measured SHC, together with the standard deviation shown in black bars with respect to temperature.

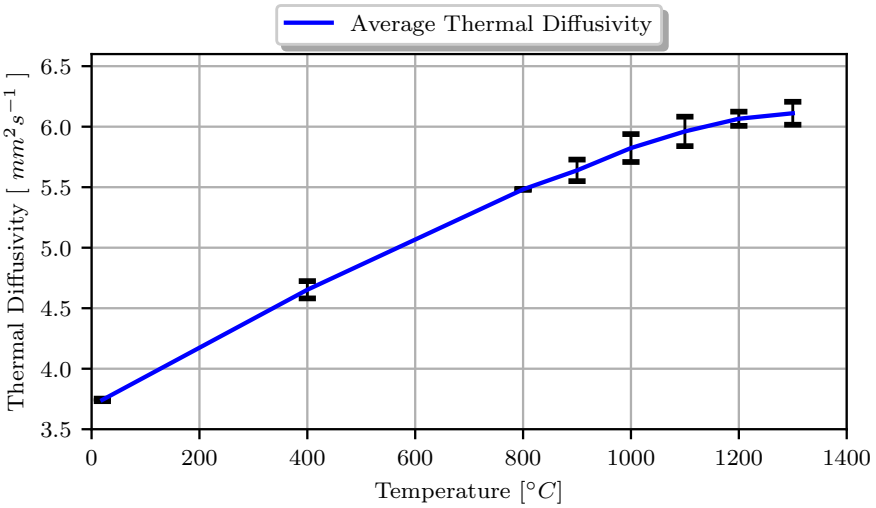

Figure 6.6 The average and the standard deviation of the measured TD values with respect to temperature.

6.1.2 Material Model Calibration

The experimental data given in the previous section is used to calibrate the SOVS model. Each material model parameter is separately explained in the following subsections.

Thermal Expansion Coefficient

Dilatometry experiments shown in Fig. 6.1 are used to approximate TEC. The expansion portion of the displacement behavior (temperatures below 950 °C) is considered for this purpose. A second-degree polynomial function can estimate TEC with respect to temperature as below:

$$\alpha_{tec} = a_{tec}\,T^2 + b_{tec}\,T + c_{tec}, \tag{6.1}$$

where the calibrated values of material constants a_{tec}, b_{tec}, and c_{tec} are given in Tab. 6.3.

a_{tec} [°C^{-3}]	b_{tec} [°C^{-2}]	c_{tec} [°C^{-1}]
2.159×10^{-11}	2.012×10^{-8}	1.339×10^{-5}

Table 6.3 The calibrated material constants to determine TEC with respect to temperature.

Apparent Viscosity

The experimentally measured apparent viscosity η_0 in Fig. 6.4 is estimated with a linear model and is defined as below:

$$\eta_0 = a_\eta \, T + b_\eta \tag{6.2}$$

where a_η and b_η are material constants. The calibrated values of the material constants for different temperatures are listed in Tab. 6.4.

Temperature [°C]	a_η [10^7 Nm^{-2}s°C^{-1}]	b_η [10^{10} Nm^{-2}s]
$T < 950$	0.0	1.4
$950 \leq T < 1100$	-4.0	5.1
$1100 \leq T < 1230$	2.0	-1.5
$1230 \leq T < 1390$	0.0	0.5

Table 6.4 The calibrated material constants to determine apparent viscosity with respect to temperature.

Grain Growth

Grain growth model parameters defined by Eq. 2.13 are calibrated with the experimentally measured grain sizes with respect to temperature, listed in Tab. 6.2. The calibrated parameters are presented in Tab. 6.5.

Temperature [°C]	Q_g [kJ mol^{-1}]	A_g [10^{-13} m^2 s^{-1}]
$T < 1100$	316	11.4
$T \geq 1100$	20	11.4

Table 6.5 The calibrated material constants to determine grain size with respect to temperature.

Sinter Stress

To facilitate and enable the calibration process of sinter stress in three stages according to the classical theories of sintering, Eq. 6.3 is modified and given by

$$\sigma_{\boldsymbol{S}} = \frac{\beta \left(\frac{\rho_{rel}}{\rho_{ref}}\right)^{\zeta}}{G} + \sigma_0, \tag{6.3}$$

where ρ_{ref} is introduced as a material constant depending on green part properties and printing parameters such as layer thickness and PSD. β and σ_0 are material constants dependent on the surface energy of the material, and ζ is an exponential factor. To determine the material constants in Eq. 6.3, the experimental data introduced in Sec. 6.1.1 is used. The calibration of parameters is conducted with respect to the actual density of the sintering body, i.e., RD lower than 65 %, between 65 % and 92 %, and higher than 92 %, representing the initial, intermediate, and final stages of sintering, respectively. Tab. 6.6 shows the calibrated values for each parameter.

Relative density [%]	β [$\mathrm{N\,m^{-1}}$]	ζ [–]	σ_0 [MPa]
$RD < 65$	0.6	15	0.10
$65 \leq RD < 92$	0.1	15	0.45
$92 \leq RD$	25.0	2	0.10

Table 6.6 The calibrated material constants to determine sinter stress in the SOVS model.

Specific Heat Capacity

By a linear fit to the average of the measured SHC given in Sec. 6.1.1 and introducing a_{shc} and b_{shc} as material constants, specific heat capacity c is defined as below:

$$c = a_{shc}\, T + b_{shc}, \tag{6.4}$$

where a_{shc} and b_{shc} are given in Tab. 6.7.

a_{shc} [$\mathrm{J\,K^{-2}\,g^{-1}}$]	b_{shc} [$\mathrm{J\,K^{-1}\,g^{-1}}$]
1.210×10^{-4}	4.877×10^{-1}

Table 6.7 The calibrated material constants to determine SHC with respect to temperature.

Thermal Conductivity

A linear relation between temperature and TD is formulated by:

$$\alpha_d = a_{td}\, T + b_{td}, \tag{6.5}$$

where a_{td} and b_{td} are material constants. By the fit to the average of the TD values plotted in Fig. 6.6, a_{td} and b_{td} values are determined and given in Tab. 6.8.

a_{td} $[\mathrm{mm^2\,s^{-1}\,K^{-1}}]$	b_{td} $[\mathrm{mm^2\,s^{-1}}]$
1.920×10^{-3}	3.840

Table 6.8 The calibrated material constants to determine TD with respect to temperature.

By plugging Eq. 6.5 into Eq. 2.20, thermal conductivity is achieved by:

$$k = (a_{td}\,T + b_{td})\,\rho\,c. \tag{6.6}$$

6.1.3 Model Implementation and Accuracy Analysis

By modeling the viscous behavior of sintering deformation with Hypela2 user-defined material model in MSC Marc solver [234, 235], the calibrated SOVS model is studied in this section. At first, the dilatometry specimen is modeled and simulated with the sintering cycle shown in Fig. 6.1, excluding the debinding stage. The resulting shrinkage with respect to temperature in the simulation is compared with dilatometry experiments in Fig. 6.7, showing a good agreement.

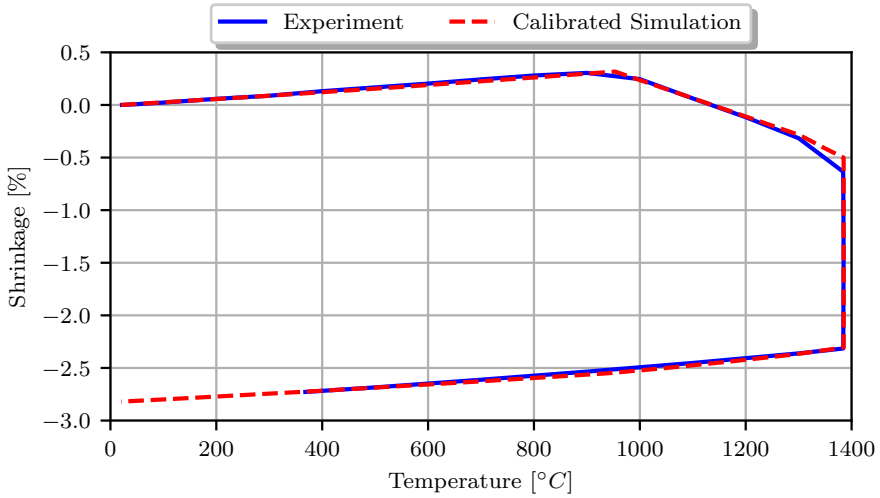

Figure 6.7 The measured and calibrated shrinkage on the sinter dilatometry specimen [188].

The densification evolution of the specimen in the simulation and the revealed experimental results in Tab. 6.2 are plotted in Fig. 6.8. Although the final density matches well with experimental evidence, the simulation underestimates density values at temperatures between 1300 °C and 1385 °C.

To analyze the prediction accuracy of the model, two samples (a double-cone and a bracket model) are chosen. Fig. 6.9 shows the samples and their dimensions. The double-cone model is meshed with an average element size of 4 mm and the bracket with 2 mm. The thermal cycle (the same as the dilatometry experiment) is applied on all the nodes to facilitate the simulation process by omitting the heat transfer analysis.

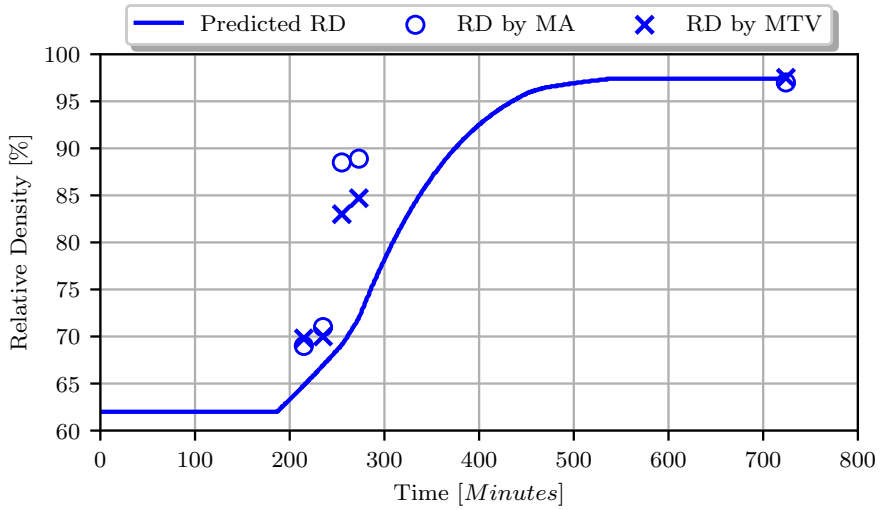

Figure 6.8 RD evolution, model predictions and experimentally measured values [188].

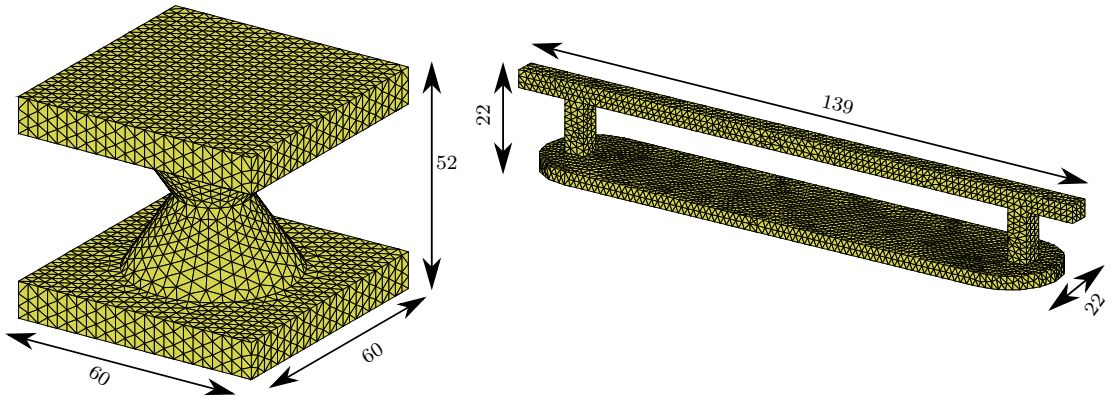

(a) **(b)**

Figure 6.9 FE mesh and dimensions (in mm) of the (a): double cone and (b): bracket model [188].

The sintering substrate is modeled as a rigid baseplate for positioning the sintering body and to capture the contact behavior between the sample and the sintering substrate. The contact is represented by a bilinear Mohr-Coulomb method and a friction coefficient of 0.2. Other than gravity, no other boundary condition is considered. The deformation results, as well as the final density distribution of the double-cone and the bracket models, are seen in Fig. 6.10 and Fig. 6.11, respectively [188].

To assess the accuracy of the simulations and by considering the manufacturing reproducibility of the technology, both models are manufactured seven times. Fig. 6.12 shows the final deformed shapes of the specimens after sintering. All samples are scanned and compared with the final deformed shapes extracted from the simulations. Preceded by an initial 3-point alignment on the basement of the models, the best-fit method is used to align the scanned surface of each experiment with the simulation result in GOM Inspect V8. Next, the surface deviation of the simulation result from each sintered sample is determined.

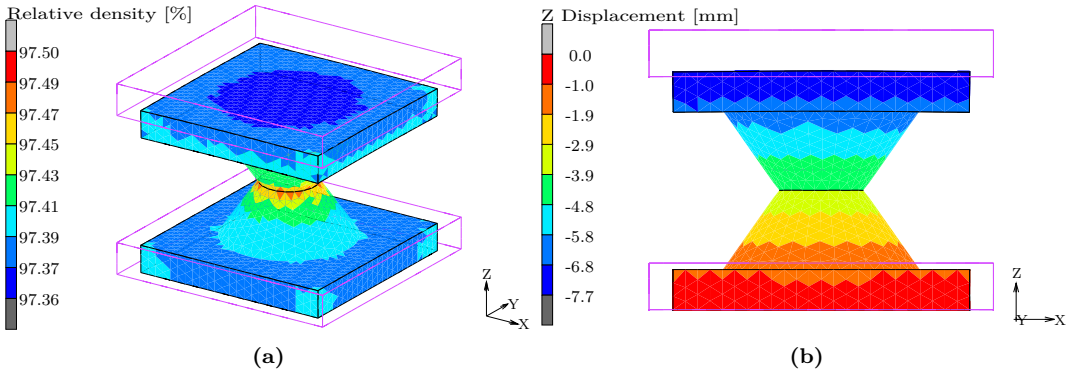

Figure 6.10 (a): The final RD and (b): deformation in Z of the double-cone model [188].

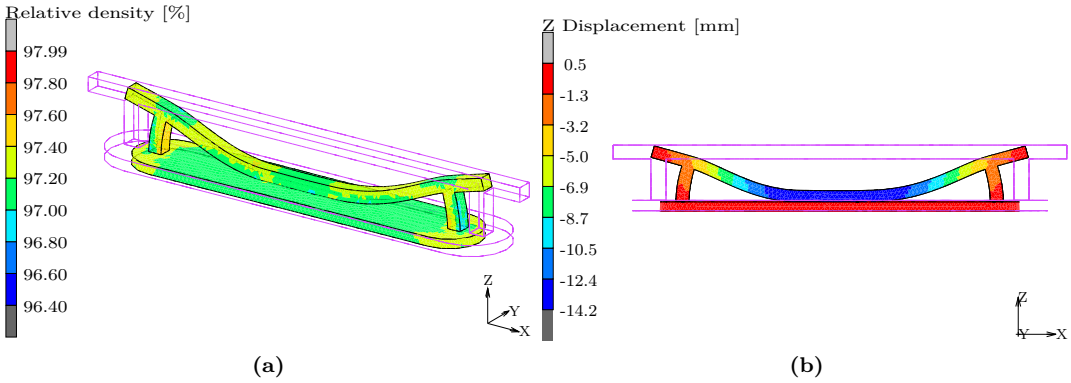

Figure 6.11 (a): The final RD and (b): deformation in Z of the bracket model [188].

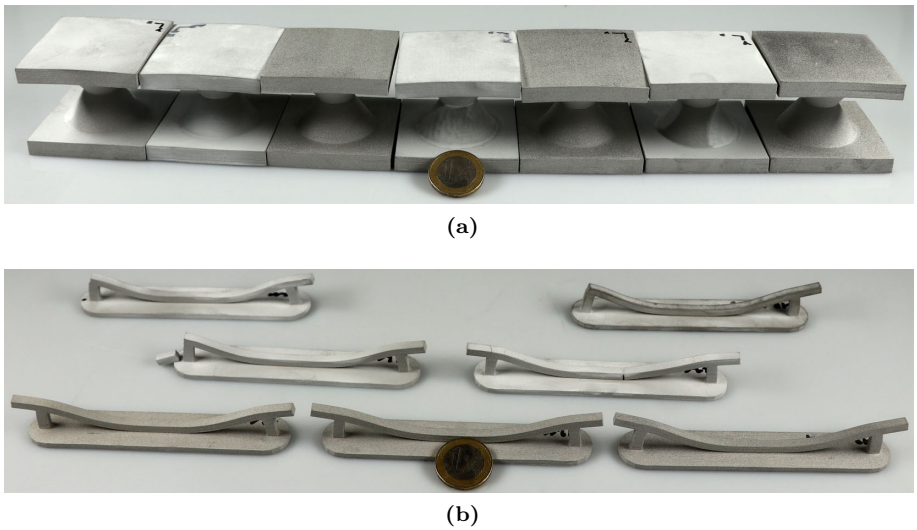

Figure 6.12 The final sintered specimens (a): double-cone and (b): bracket [188].

By setting a tolerance span of 1 mm, the total area of the surfaces that lay within the tolerance is measured. Averagely, the simulation prediction is in-tolerance with 76.4 % of the surface envelope in the double-cone specimens. This value increases to 96.9 % for the bracket samples. The standard deviation of in-tolerance surfaces is 5.3 % for the double-cone samples, whereas 3.15 % for the bracket specimens.

The surface deviation of simulations from the sample, with the best agreement (the highest in-tolerance percentage), is demonstrated in Fig. 6.13a and Fig. 6.13b for the double-cone and bracket, respectively. Furthermore, the metallographic analysis on different sections of the samples proves the predicted final density by simulations, which is around 97.4 % for both geometries [188].

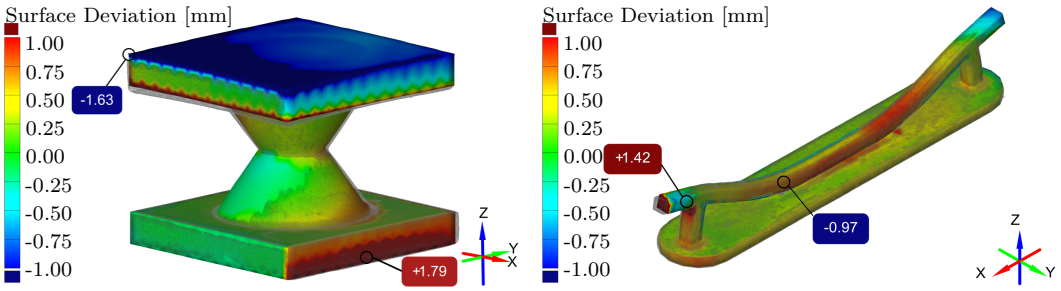

Figure 6.13 Comparison of predicted and measured deformation for the sample, with the highest in-tolerance area of (a): the double-cone and (b): the bracket model [188].

6.1.4 Sensitivity Analysis

To study the effect and importance of each material model parameter on shrinkage, warpage, and density predictions of simulations, a sensitivity analysis is required. This step is crucial to appraise the effect of any possible inaccuracy or uncertainty quantitatively originating from experimental errors and limitations, simplifications, assumptions, extrapolations, or data fittings. All the independent material model parameters, which are directly determined by experiments, are considered study-parameters.

The study-parameters are relative density, thermal expansion coefficient α_{tec}, apparent viscosity η_0, specific heat capacity c, and thermal diffusivity α_d. Furthermore, sinter stress is calibrated indirectly and is composed of several material constants. For the sake of simplicity, sinter stress is considered an independent parameter in the sensitivity analysis. As mentioned in Sec. 6.1.2, grain size is also determined experimentally. However, this parameter is only involved in the calculation of sinter stress, which is already considered in the sensitivity study.

For the sensitivity analysis, using response surface methodology, a design surface is fitted to the response values of a predefined set of design points. All the mentioned study-parameters are considered to build a combination set of design points i, chosen by the D-Optimal approach. 172 design points with different values for the study-parameters are specified, and the numerical simulations are run for each set of the design points. A bracket-like geometry is designed for this study, as shown in Fig. 6.14. The dimensions and areas to measure shrinkage (marked with L_{br}) and warpage (marked with W_{br}) of the bracket-like model are also shown in the figure. The warpage is measured on the middle point of the bracket's bridge. The final density is computed by averaging the final density of all elements.

The values for each study-parameter assigned by the D-Optimal sampling approach are distributed within a minimum and maximum range. For the RD, the lower limit is set to 52 %, whereas the upper is 60 %, as reported by [28, 236] for SS316L in MBJ. For the other study-parameters, the introduced approximation functions given in Sec. 6.1.2 are kept unchanged, and therefore an offset variable is considered. The offset variable can change by a margin of 10 % from the respective calibrated function for each study-parameter.

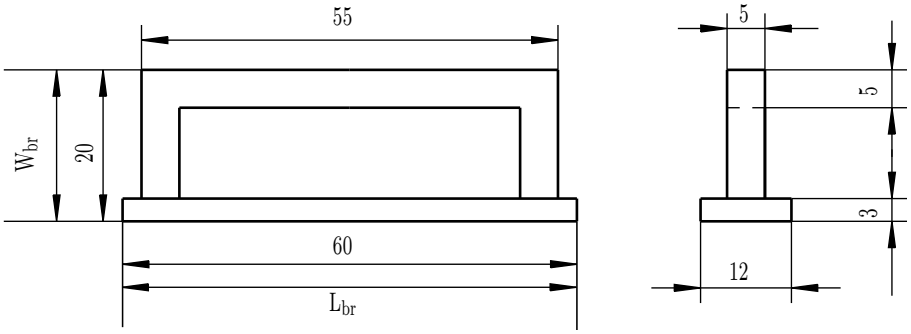

Figure 6.14 The bracket-like geometry for sensitivity analysis (all dimensions in mm).

By introducing a general offset variable λ^i at any design point i, an offset to the function $f(x)$ is made through:

$$f(x)^i = (1 + \lambda^i)\ f(x), \tag{6.7}$$

where $f(x)^i$ is the value of the offset function at design point i.

Analogous to Eq. 6.7, the determining equations for TEC (6.1), sinter stress (6.3), apparent viscosity (6.2), SHC (6.4), and TD (6.5) are transformed to the following equations to set the value of the study-parameters at any design point, respectively:

$$\begin{cases} \alpha^i_{tec} = \left(1 + \lambda^i_{\alpha_{tec}}\right)\ [a_{tec}T^2 + b_{tec}T + c_{tec}] \\ \sigma^i_{\boldsymbol{S}} = \left(1 + \lambda^i_{\sigma_{\boldsymbol{S}}}\right)\ \left[\dfrac{\beta\left(\frac{\rho_{rel}}{\rho_{ref}}\right)^{\zeta}}{G} + \sigma_0\right] \\ \eta^i_0 = \left(1 + \lambda^i_{\eta_0}\right)\ [a_\eta T + b_\eta] \\ c^i = \left(1 + \lambda^i_{\boldsymbol{C}}\right)\ [a_{shc}T + b_{shc}] \\ \alpha^i_d = \left(1 + \lambda^i_{\boldsymbol{\alpha}_d}\right)\ [a_{td}T + b_{td}]. \end{cases} \tag{6.8}$$

The bracket-like model is simulated with the same sintering cycle and material model introduced in Sec. 6.1.2 and Sec. 6.1.3 by replacing the calibrated values of the study-parameters with the chosen values from the 172 design points. To consider heat transfer analysis and investigate the relevance of SHC and TD, the thermal cycle is applied just on the surface nodes. As an example, Fig. 6.15 illustrates the sintering deformation of the bracket-like model for two design points, with the given study parameters on the figures.

The response values, i.e., shrinkage, warpage, and density, are extracted from each simulation run. Next, a polynomial metamodel with quadratic order is constructed on the given design points and the extracted responses. Finally, to assess the effects of each parameter, Sobol global sensitivity analysis is performed. LS-OPTVersion 6.0 is used for the sensitivity analysis [237, 238]. The Sobol analysis result is introduced in Fig. 6.16. It can be observed that RD, sinter stress, and the apparent viscosity have the most significant influence on the response values (shrinkage, warpage, density). In contrast, the contribution of SHC, TD, and TEC is almost zero.

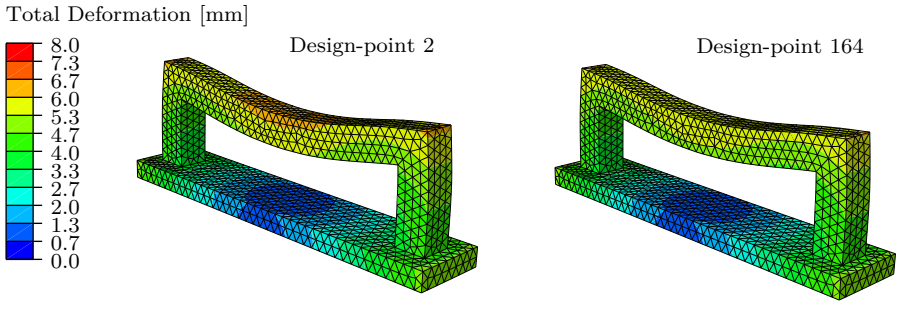

GPD [%]	λα-tec [-]	λσ-s [-]	λη-0 [-]	λC [-]	λα-d [-]
0.57	-0.1	-0.1	0	0	0

GPD [%]	λα-tec [-]	λσ-s [-]	λη-0 [-]	λC [-]	λα-d [-]
0.575	0	0.02	0.06	0	0

Figure 6.15 The deformation behavior of the bracket-model, left: at design-point 2 and right: at design-point 164.

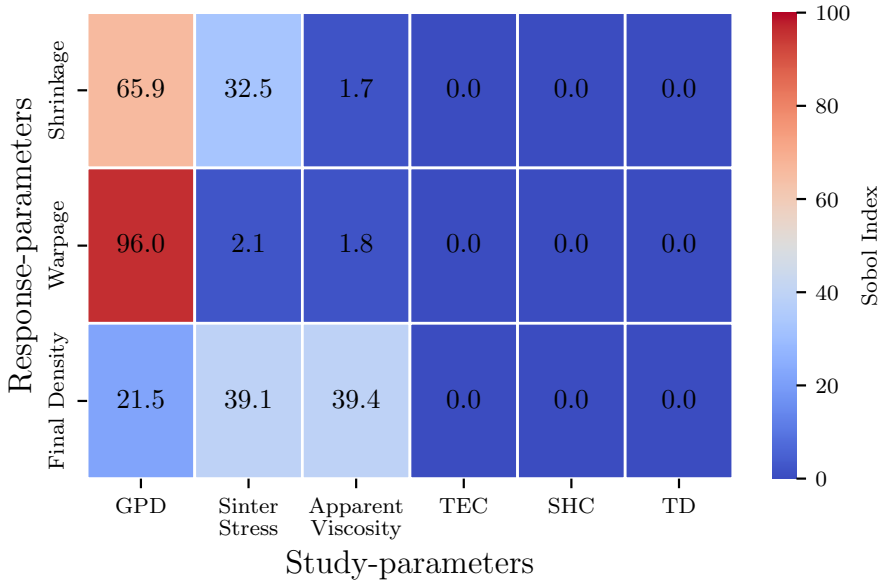

Figure 6.16 The influence of each study-parameter on shrinkage, warpage, and final density.

6.1.5 Evaluation of the SOVS Model

The validation study for the calibrated SOVS model reveals that the approach is able to capture the sintering deformation/densification of MBJ samples. However, the simulations exhibit a deviation of more than 1 mm from experimental results in some cases. In addition, it was observed that the density evolution predicted by simulations did not exhibit good agreement with the experimental measurements during the intermediate stage of sintering. Furthermore, the validation studies with the SOVS model have identified several characteristics of MBJ parts:

- The anisotropic properties of the printed parts result in non-uniform shrinkage, leading to uneven deformation during sintering [28].
- The validation experiments involving bracket and double-cone geometries reveal that the sintered shape of the geometries differs, despite using the same geometry and manufacturing parameters for all samples. This highlights the lack of reproducibility in the MBJ process.

- Variations in GPD within print jobs can decrease prediction accuracy, especially if the assumed GPD in simulations differs from the actual parts. In addition, the accuracy of predicting final deviations can also be affected by deviations between as-print and CAD models when simulating geometries.

Hence, besides the above-mentioned MBJ characteristics, the most influential properties on sintering deformation identified by the sensitivity analysis (sintering stress, apparent viscosity, and GPD) should be further studied to increase the accuracy of simulations. In addition to improving the accuracy, developing a general sintering deformation model would help minimize the impact of dissimilarities between labor and workshop machines, which can lead to different results for calibration and implementation.

6.2 Data-driven Simulation of Sintering Deformation

A generic computational framework will be introduced in this section. Experiments are performed to determine green part properties and to model a universal sintering model for MBJ parts. After performing experiments, an approach is developed to predict GPP. The MBJ sintering deformation framework is developed and implemented in a FE code. To tune the material model and adapt it for any set of manufacturing parameters, an adjustment method is proposed.

6.2.1 Experiments

The required samples and parts for the development of the DDNS method, presented in this section, are printed with the given parameters in Tab. 4.1. A substantial amount of experimental data is necessary for the development of the DDNS approach. Because the manufacturing elements for the investigation of the SOVS method are different from those for the DDNS approach development (Compare Tab. 6.1 with Tab. 4.1), the experiments previously presented in Sec. 6.1.1 cannot be utilized and must be repeated. This is crucial to avoid any possible inconsistencies due to different manufacturing parameters. The performed experiments are introduced in this section.

Green Part Properties

Cubes with the target dimensions of 22 mm, 20 mm, and 18 mm in the X, Y, and Z directions are considered to evaluate the GPD and dimensional accuracy. At first, 84 cubes are distributed within the print chamber in two levels, i.e., 42 cubes positioned at the bottom and 42 cubes stacked directly on top, with a gap of 12 mm. To reduce the experimental costs, a maximum print height of 48 mm is studied here (See the print chamber's dimension in Fig. 4.1). For higher printer jobs, it is assumed that the performance remains similar to that of the second level. Since it is not plausible to cover the whole print chamber with the mentioned cubes, one further job is printed with 60 cubes distributed in the vacancies of the previous print job in the same rows. Fig. 6.17a and Fig. 6.17b depict the distribution of the cubes for both jobs.

The printed cubes are weighed and 3D-scanned for the determination of current (as-print) dimensions. The obtained data is divided into two series based on the Z coordinate of the samples, namely the first and second levels. These data sets are considered nodes that contain values for GPD and dimensions. To interpolate the values between the nodes, a cubic interpolation function is employed using the SCIPY package [239]. This interpolation method is used to determine the respective values at each level. Additionally, a further cubic interpolation is performed within and among all the nodes at both levels to estimate the field for the whole print job.

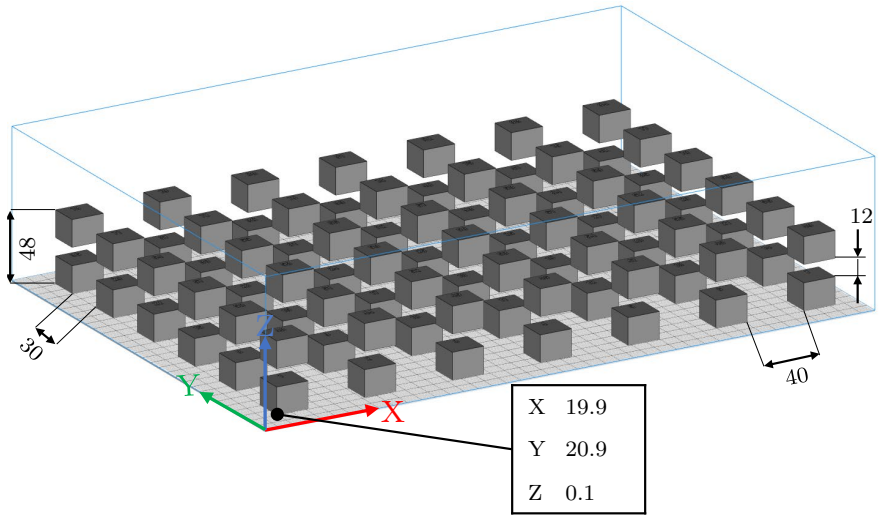

(a)

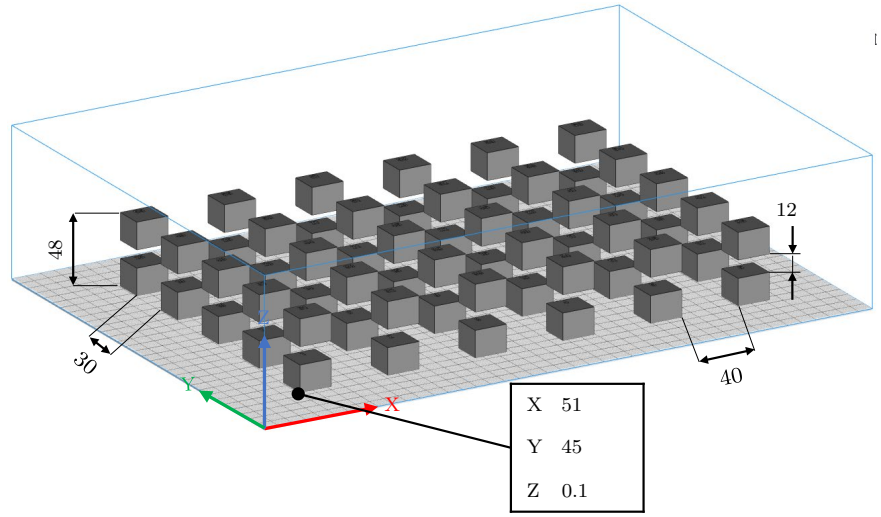

(b)

Figure 6.17 The distribution of the cubes in the print chamber for (a): the first configuration with 84 cubes and (b): the second configuration with 60 cubes. (dimensions in mm)

Density

Fig. 6.18 illustrates the green part density distribution within the print chamber with respect to the X-Y coordinates in the two levels. The average GPD equals 57.85 % with a standard deviation of 0.53 %. The density values vary between 55.7 % and 58.5 % at the first level. At the second level, densities lay mainly between 57.0 % and 58.6 %; therefore, a lower discrepancy is seen.

Dimension

The dimension deviation of green parts is analyzed by comparing the as-print dimensions with their respective nominal dimensions in all three directions. The same methodology as the GPD analysis is utilized to determine the dimension deviations with respect to the print chamber coordinates. The deviations of the first and second levels for the X, Y, and Z dimensions are illustrated in Fig. 6.19.

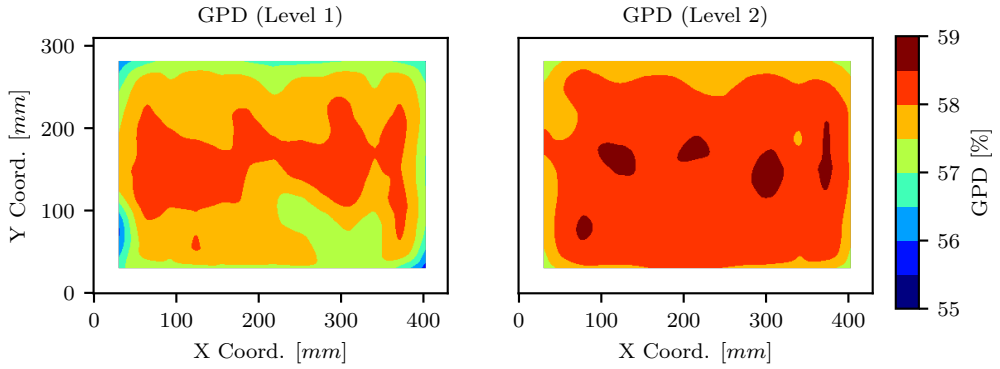

Figure 6.18 The green part density distribution in the first and the second levels, shown in the XY plane.

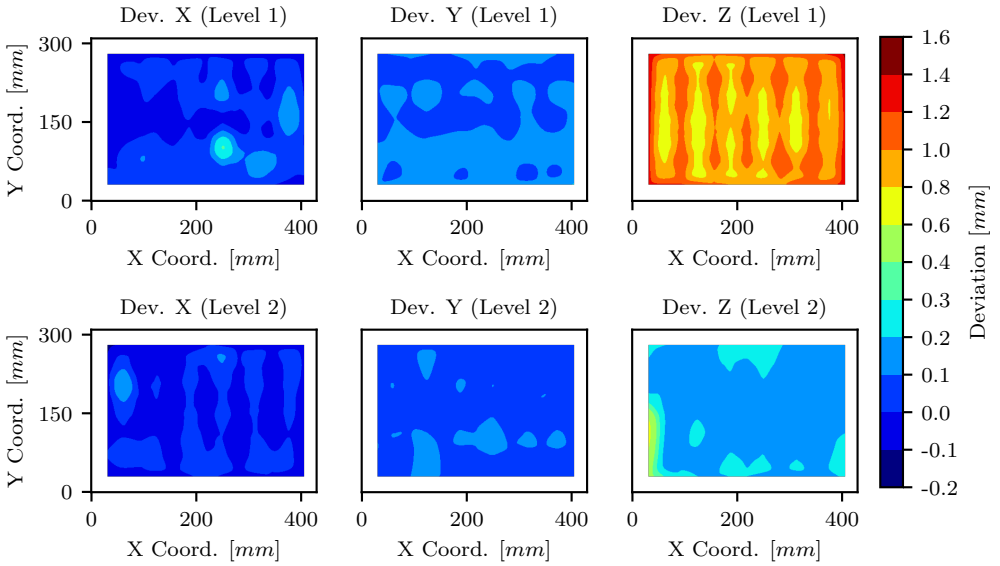

Figure 6.19 The deviation between as-print and nominal X, Y, and Z dimensions with respect to the X-Y coordinates at the first and second levels.

The dimensional accuracy and quality of the printed parts are mainly affected by printing elements such as powder characteristics, print orientation, binder application, printing speed, and curing [11, 218, 240–242]. Thus, it is assumed that the deviations do not depend on the parts' dimensions and cannot be determined relatively. So, deviations should be given in the unit of length. The observed deviations in the Z direction are between 0.11 mm and 1.48 mm, which is significantly higher than that of in the X and Y directions. Tab. 6.9 contains the average and Standard Deviation (StD) of the measured values for each direction. As also seen in Fig 6.19, for dimensions in Z, the first level shows a much higher deviation in comparison to the second level.

Dilatometer

To define a generic sintering model independent from a specific thermal cycle, a noticeable amount of dilatometry experiments is required. However, considering the available resources, seven different cycles are designed by changing the heating rate, intermediate holding stage, maximum temperature, and holding time at maximum temperature.

Direction	Average [mm]	StD [mm]
X	0.001	0.059
Y	0.091	0.041
Z	0.595	0.439

Table 6.9 The green part dimensional deviation from nominal dimensions.

Tab. 6.10 summarizes the main characteristics of each cycle. For each cycle, two dilatometry specimens are studied, one manufactured in the Z direction and the other in X. The specimens are initially debound for four hours at 400 °C and then sintered with the respective cycles under an H_2 atmosphere. In total, 14 samples are sintered and measured. The thermal cycles and the corresponding dimension changes of the X and Z specimens are shown in Fig. 6.20.

Cycle	Heating rate [K/ min]	Holding time at 1050 °C [min]	Max. temp. [°C]	Holding time at max. temp. [min]	Figure
Cycle-1	5.0	120	1380	120	6.20a
Cycle-2	5.0	120	1385	120	6.20b
Cycle-3	5.0	0	1380	120	6.20c
Cycle-4	5.0	0	1380	210	6.20d
Cycle-5	2.0	120	1380	120	6.20e
Cycle-6	2.0	0	1380	120	6.20f
Cycle-7	5.0	120	1400	120	6.20g

Table 6.10 The characteristics of the sinter cycles.

Metallographic Analysis

To determine the grain size and density evolution, five samples printed in the Z direction are heated to 1050 °C, 1100 °C, 1200 °C, 1300 °C, and 1350 °C; they are held for 120 minutes at these temperatures and cooled down to RT. The cycles are called A, B, C, D, and E, respectively. The porosity of each sample is measured by the MA method, and grain size is specified according to DIN EN ISO 643. GS and porosity are inspected using two cuts on the samples: one parallel and one perpendicular to the print direction of the samples. Then, on each cut, three images are taken, and the analysis is performed on each image. Finally, the average measured values on each specimen define the GS and porosity. The average, StD, and Coefficient of Variation (CoV) of the values are given in Tab. 6.11. The evolution of densification and GS for the mentioned cycles are demonstrated in Fig. 6.21.

Looking at Fig. 6.21a, it is observable that at 1050 °C, still the separate particles are easily recognized, and therefore no grain growth can be detected. First, at 1100 °C, inner-particle grains form bigger grains (See Fig 6.21a).

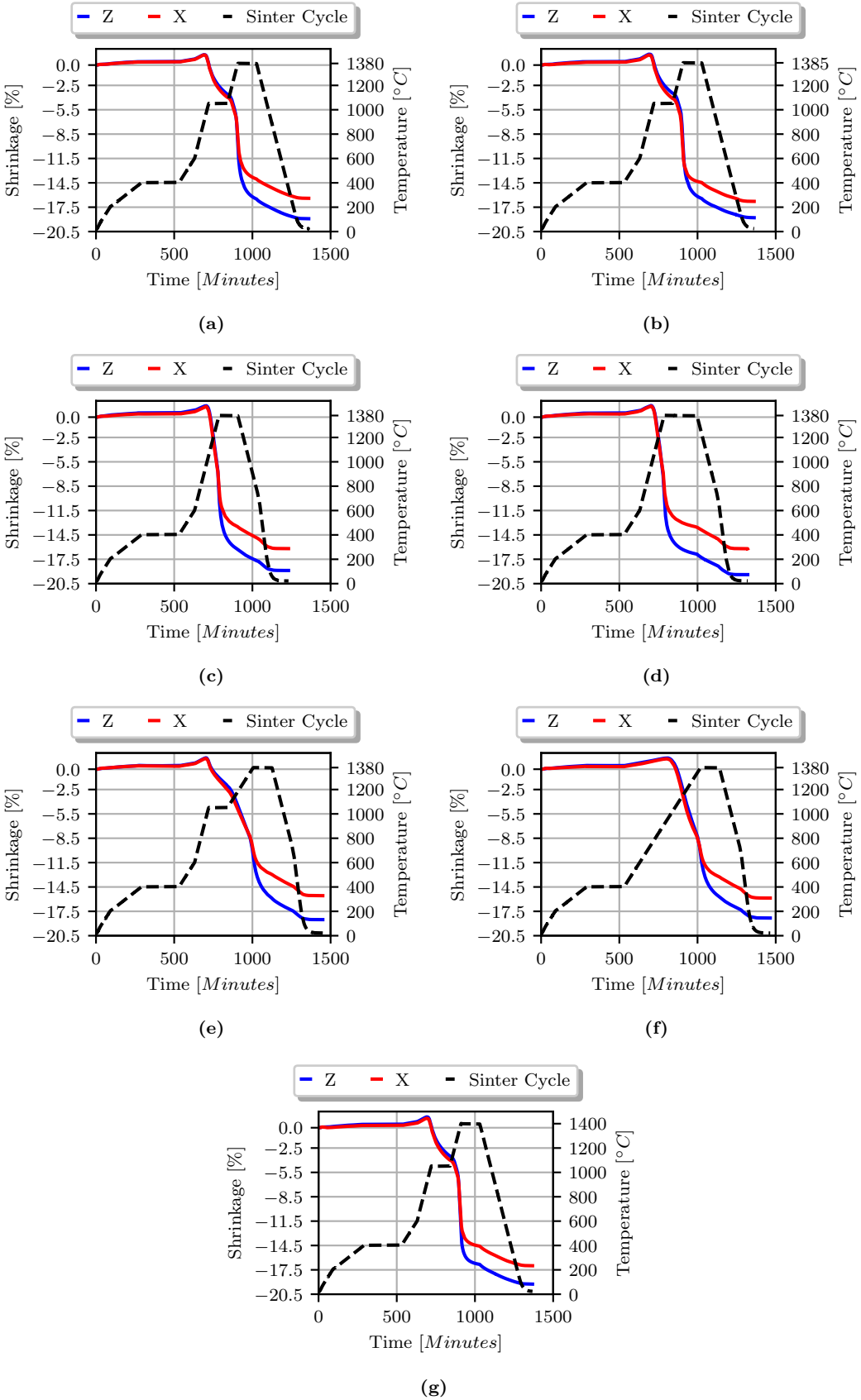

Figure 6.20 The shrinkage behavior of X and Z samples for (a): Cycle 1, (b): Cycle 2, (c): Cycle 3, (d): Cycle 4, (e): Cycle 5, (f): Cycle 6, (g): Cycle 7.

Sinter cycle	Max. temp.	Porosity			Grain size		
		Average	StD	CoV	Average	StD	CoV
	[°C]	[%]	[%]	[%]	[µm]	[µm]	[%]
Cycle A	1050	34.2	1.7	5.0	-	-	-
Cycle B	1100	26.8	1.5	5.6	17.4	3.8	21.8
Cycle C	1200	23.2	0.7	3.0	26.6	4.9	18.4
Cycle D	1300	18.4	0.6	3.3	29.9	3.0	10.0
Cycle E	1350	8.8	0.3	3.8	39.3	2.4	6.1

Table 6.11 The porosity and grain size studies with respect to temperature.

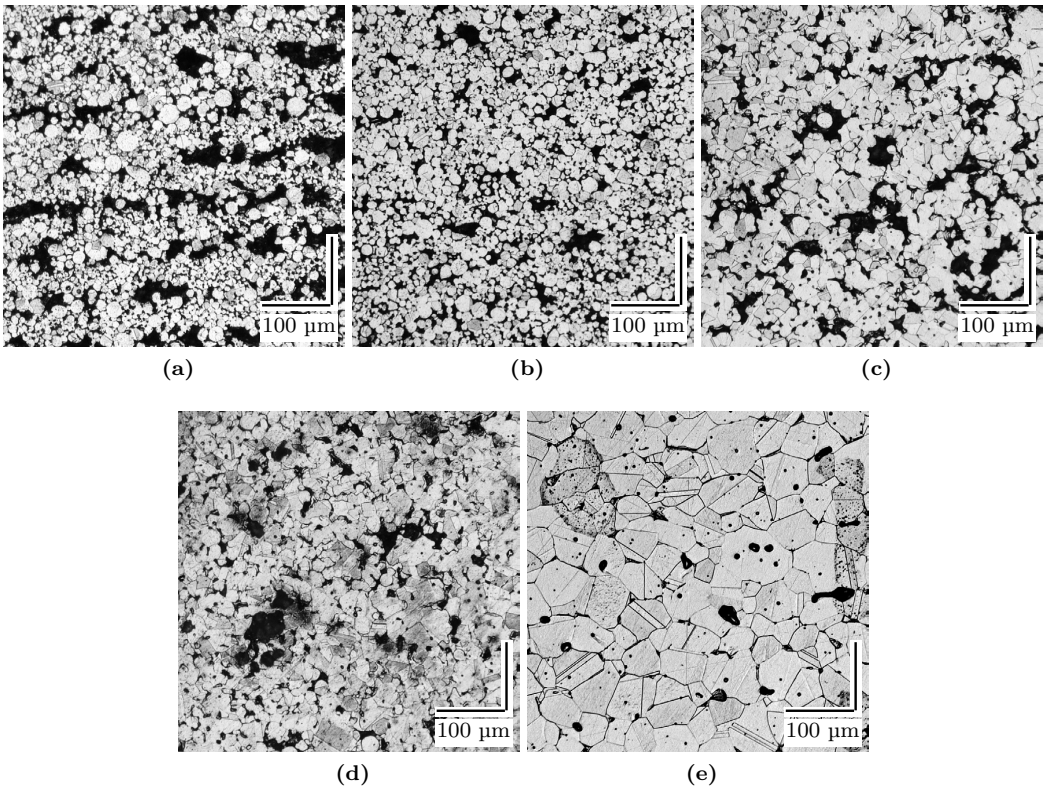

Figure 6.21 The GS and porosity evolution of sintering dilatometry samples for (a): Cycle A, (b): Cycle B, (c): Cycle C, (d): Cycle D, and (e): Cycle E.

It is also worth noticing that determining grain size is still more difficult for lower temperatures since the grains are not perfectly formed in comparison to 1350 °C. The difficulty of measurements explains the higher CoV values for lower temperatures. Furthermore, the specimens sintered at 1050 °C and 1100 °C are still showing an anisotropic structure, resulting in higher uncertainties for porosity measurements (See the higher CoV values for these temperatures in Tab. 6.11).

All presented dilatometry experiments in Fig. 6.20 are also metallographically analyzed. Tab. 6.12 presents each sample's initial length, GPD, Sintered Part Density (SPD), final shrinkage, Sintering Activation Temperature (SAT), and GS. Green density is calculated by the MtV approach, whereas

sinter density is determined by MA, approved by MtV. The standard deviation of SPD values is under 0.5 % for all samples. SAT is specified at the temperature where thermal elongation is at its maximum state, and from this state on, the specimen starts to shrink.

Sinter cycle	Print direction	Initial length	GPD	SPD	SAT	Final shrinkage	Grain size	
							Average	StD
		[mm]	[%]	[%]	[°C]	[%]	[µm]	[µm]
Cycle 1	X	19.99	56.1	94.8	921.8	-16.42	43.7	1.7
	Z	20.36	56.9	95.1	922.5	-18.92	44.1	2.2
Cycle 2	X	19.96	56.2	98.3	924.9	-16.78	47.9	2.4
	Z	20.45	56.4	97.8	928.1	-18.80	49.1	2.0
Cycle 3	X	20.04	58.7	94.5	962.0	-15.49	41.5	1.8
	Z	20.16	57.9	95.9	968.9	-18.11	40.9	1.6
Cycle 4	X	20.06	58.6	98.3	962.3	-16.20	52.7	2.2
	Z	20.03	57.9	98.5	963.0	-19.39	52.3	3.0
Cycle 5	X	20.03	59.5	96.1	964.8	-15.57	45.9	2.9
	Z	20.16	58.5	98.4	970.0	-18.52	47.6	3.4
Cycle 6	X	20.04	58.5	97.2	946.9	-15.86	47.0	1.4
	Z	20.09	59.3	97.7	951.4	-18.33	45.7	4.9
Cycle 7	X	20.02	55.5	98.1	927.6	-17.00	49.3	3.5
	Z	20.55	55.7	98.3	928.0	-19.26	48.9	3.1

Table 6.12 The properties of the sintering dilatometry samples, before and after sintering dilatometry.

Because the samples sintered with the quoted cycles almost reached the full density, no anisotropic structure is seen in the inspections. Therefore, the determined values for each cycle are approximately the same for both specimens printed in X and Z. No correlation is found between GPD and SPD, as also reported by [33]. The determined GS for cycle-1, using the same powder, matches well with the previously reported value by [42]. The average GS of the virgin powder is measured and found to be 4.9 µm. Finally, the average mass change before and after sintering for all dilatometry experiments is 1.4 % of the printed mass, indicating the mass of the removed binder from the green parts.

Apparent Viscosity

To determine the apparent viscosity of the sintering bodies, the cyclic loading approach was employed in Sec. 6.1.1. Although in the cyclic loading, some effects such as densification, shrinkage anisotropy, and microstructure change are minimized compared to constant load sinter-forging [158, 172, 176]; still, these effects contribute to misleading viscosity values. Besides, cyclic loading specimens experience an initial powder rearrangement with even low external forces, leading to a different shrinkage and densification behavior from free-sintering [175]. Furthermore, apparent viscosity is solely determined with respect to temperature, and it is assumed that the densification is integrated into the calculations.

Thus, in this stage the beam deflection test is performed in a thermo-optical graphite furnace to measure the deflection in the middle of a sample. A 5 K/ min heating rate is used to heat the beam to 1400 °C. Fig. 6.22 shows the beam before the measurements. The beam deflection at 1100 °C, 1150 °C, and 1200 °C are shown in Fig. 6.23.

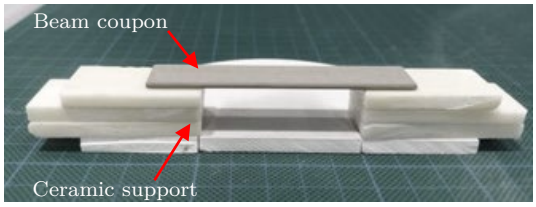

Figure 6.22 The configuration of the beam coupon before the deflection measurements.

(a) **(b)** **(c)**

Figure 6.23 The beam deflection captured with TOM at (a): 1100 °C, (b): 1150 °C, and (c): 1200 °C.

Due to the densification of the porous materials with rising temperature, creep test specimens slip on the supports, and can cause three issues:

- Densification causes dynamic friction between the specimen and the support, leading to lateral forces. The lateral forces can tilt or move the specimens.
- Compression forces generated from the densification process on both sides of the center of gravity overestimate the deflection value.
- The occurrence of specimen slippage, particularly at elevated temperatures, can result in test failures or decreased measurement reproducibility.

The high degree of design flexibility offered by AM technology allows for the resolution of challenges associated with conventional beam deflection tests. By assuming that the deflection behavior of the arm in a cross-shaped geometry displayed in Fig. 6.24 is similar to a cantilever beam and under the premise of satisfying the assumptions outlined in the Euler-Bernoulli beam theory [243], the deflection of the arm (cantilever beam) can be estimated. Apparent viscosity can then be indirectly calculated by determining the deflection rate $\dot{\delta}$ of any of the four arms of the cross-shaped geometry, as given by:

$$\eta_0 = \frac{3 m_a \, g \, L_a^3}{2 b_a \, t_a^3 \, \dot{\delta}_{max}}, \tag{6.9}$$

where m_a, L_a, b_a, and t_a refer to the mass, length, width, and thickness of the arm, respectively.

Determining a material's apparent viscosity on the cross-shaped geometry involves measuring the relevant dimensions over time and temperature. While the maximum deflection δ_{max} can be directly measured at the front arm's tip, the direct measurement of the dimensions L_a, b_a, and t_a is impractical, as TOM relies on analyzing the reflected shadows of geometries.

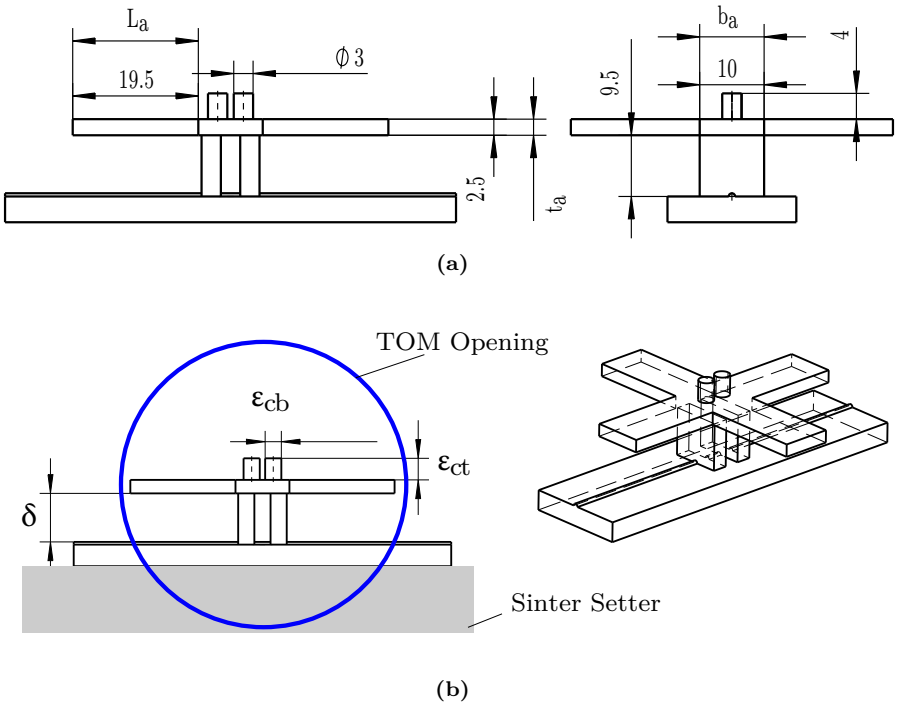

Figure 6.24 (a): The technical drawing of the cross-shape geometry (dimensions in mm) and (b): the schematic and the positioning of the cross-shape geometry in TOM.

The particular shape of the geometry and its deformation obscure these dimensions. To address this challenge, cylinders are designed into the cross-shaped geometry, allowing for indirect and proportional calculation of L_a, b_a, and t_a. This approach involves measuring the shrinkage of the cylinders in diameter and height (denoted by ϵ_{cb} and ϵ_{ct} in Fig. 6.24b), from which L_a, b_a, and t_a can be estimated. The anisotropic shrinkage of the specimen can also be considered by having the shrinkage values in build and one of the other two directions (print head or recoater directions).

To observe the deflection and densification behavior, two thermo-optical furnaces are available: a metal-chamber furnace with N_2 atmosphere and a graphite-chamber furnace with H_2. Considering that the sintering operations in the workshop are performed under H_2, the graphite-chamber furnace is initially selected for the measurements. However, due to the interaction of the graphite-chamber furnace with the specimen at high temperatures (See Appendix A), the metal-chamber furnace with N_2 atmosphere is utilized. Due to the heat transfer mechanisms of the furnace and the anisotropic properties of the sample, an unexpected result is observed. Instead of the arms of the cross-shaped geometry slumping, they rose at the end of the cycle, as illustrated in Fig. 6.25.

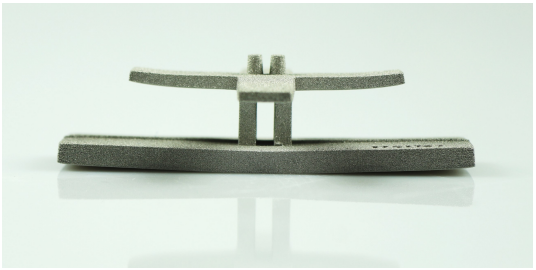

Figure 6.25 The deformation behavior of the cross-shaped sample in the metal-chamber furnace with N_2 atmosphere and a $5\,\mathrm{K/min}$ heating rate: the arms rise instead of slumping at the end of the cycle.

To mitigate undesired heat transfer effects and unknown influences, the heating rate for the subsequent sample is reduced to 2 K/ min in the metal-chamber furnace. Additionally, the sample is subjected to debinding and pre-sintering at 1000 °C in the workshop furnace to minimize any interaction of the binder with the furnace atmosphere during in-situ sintering. The deflections of the specimen at 1050 °C, 1200 °C, 1300 °C, and 1400 °C are displayed in Fig. 6.26.

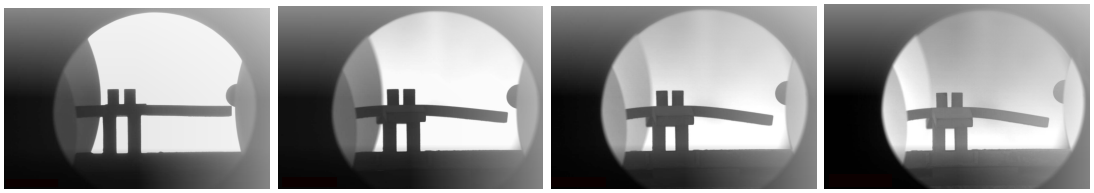

(a) (b) (c) (d)

Figure 6.26 The deflection of the cross-shape sample, sintered with a heating rate of 2 K/ min in the metal-chamber furnace at (a): 1050 °C, (b): 1200 °C, (c): 1300 °C, and (d): 1400 °C.

The change of the indicated dimensions in Fig. 6.24a are measured with respect to temperature and given in the range of 1050 °C to 1400 °C (See Fig. 6.27).

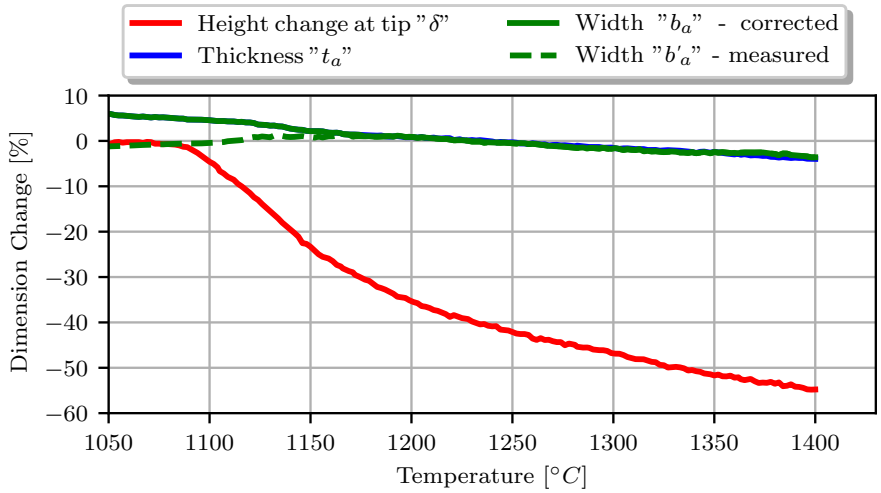

Figure 6.27 The dimensional changes of the cross-shaped geometry as a function of temperature in the range of 1050 °C to 1400 °C.

As expected, the thermal expansion causes a positive change in thickness t_a at 1050 °C, where sintering is still progressing slowly. However, the thickness decreases as sintering continues. The initial size increase is not seen for width b_a. This could be attributed to the measurement points selected on the cylinders and the rigid motion of the furnace and specimen. The cylinders intersect with the cross-shape specimen, causing different shrinkage/expansion rates, resulting in a tapered manner. The dimensional change is measured at the middle height of the cylindrical features, where the borders' width is smaller than the initial configuration. Moreover, the rigid motion of the furnace and the specimen can hinder accurate measurements, particularly in the lateral direction of fine features.

As seen in Fig. 6.27, the dimension changes of the thickness t_a and the width b_a match closely at temperatures above 1180 °C. Thus, it is assumed that the dimension change below this temperature follows this pattern, and the dimension change curve of b'_a is replaced by the corrected curve b_a. On the

contrary, the relative height change δ, which represents the arm deflection, is measured relative to the height change at the root of the arm; therefore, the height solely reduces.

Although the in-situ measurements successfully depict the deflection behavior with respect to temperature, it is still difficult to scale the determined apparent viscosity to other furnaces due to the following reasons:

- The measurements are performed solely with a single GPD. Thus, the influence of initial density on deflection measurements is not investigated.
- In the course of the measurement, it is observed that the sinter furnace and sintering atmosphere impact the deflection behavior significantly. Therefore, the scalability of the measurements to other furnaces is burdensome.

Since the validation and Proof of Concept (PoC) experiments will be done with the workshop furnace in this study, and considering the fact that sintering is mainly performed under H_2, new experiments in the workshop furnace should be designed. The workshop furnace is enclosed, so it does not allow for in-situ process monitoring. Therefore, sequential discontinuous sintering deflection experiments are conducted instead. To simplify the geometry and address depowdering issues, a T-shape sample is used to measure cantilever deflection at the end of the arm. 25 samples are printed with DPC so that the middle pillar is parallel to the X axis, as shown in Fig. 6.28.

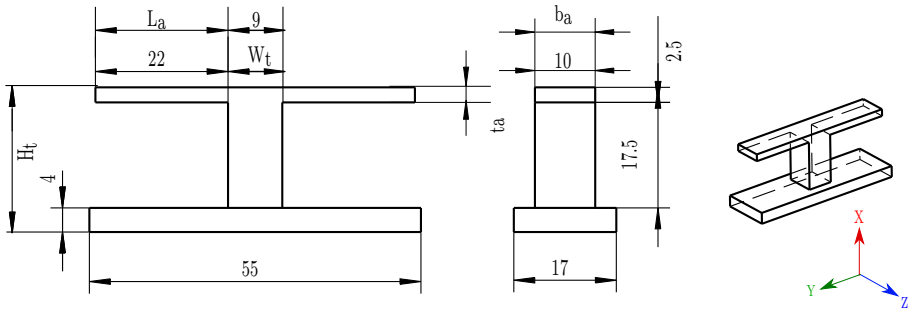

Figure 6.28 The dimensions in mm and the printing orientation of the T-shape sample used for measuring cantilever deflection in sequential discontinuous sintering experiments. The DPC is not shown here.

Despite the geometry's high estimated FI (about 65 % calculated by the failure prediction model), it remains suitable for viscosity determination due to its convenient measurability of deflection. Five different densities are studied to examine the effect of initial density on deflection. The samples are sorted into five groups, each containing five members. To avoid debinding failures, the specimens are firstly debound with live-setters and pre-sintered up to 950 °C with negligible density changes. Live-setters support the arms from below and mitigate the bending stress at the root of the arms. They are placed between the arm and the base, as seen in Fig. 6.29. To avoid sinter joining between the samples and the live-setters, Al_2O_3 powder is applied to the contacting surfaces.

Next, other than a group with the green density (approximately 58 %), the other groups are sintered individually at temperatures of 1050 °C, 1150 °C, 1250 °C, and 1350 °C for two hours to achieve four different Initial Relative Density (IRD) of 67.6 %, 76.2 %, 80.6 %, and 91.9 %, respectively. The densities are achieved solely with the MtV approach and not by destructive MA to preserve the geometries for further measurements. The live-setters are again employed during the density preparations to prevent arm deflection. The live-setters shrink with the samples and support the arms from below.

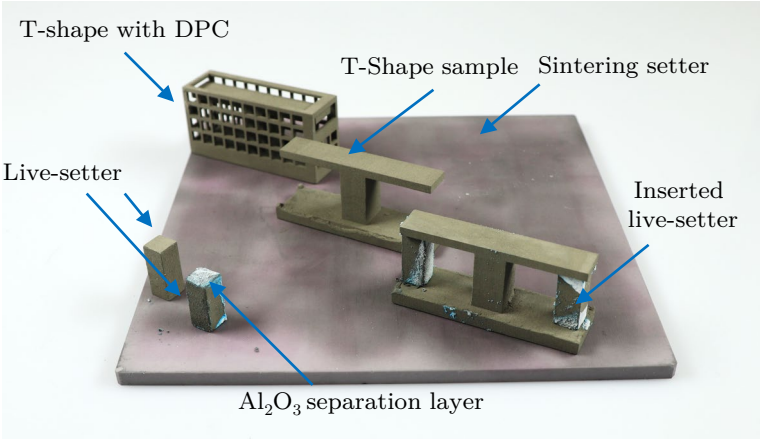

Figure 6.29 A T-shape sample with the DPC, a sample after breaking the cage, and a sample with inserted liver-setters. A DPC is utilized to prevent potential damage to the T-shape objects during depowdering. The DPC will be manually disassembled before placing the T-shape object into the furnace. Live-setters are used to avoid arm deflection during density preparation sintering jobs.

Then, five further sinter cycles are run, with the temperature raised to 1050 °C, 1150 °C, 1250 °C, 1350 °C, and 1380 °C, respectively, held for two hours, and followed by cooling down to RT. In each sinter cycle run, one sample is sintered from each group of different initial densities. Accordingly, five samples with various initial densities are sintered in each cycle. The samples are sintered without any liver-setter to measure the arm deflection. Fig. 6.30 illustrates the deflected geometries of samples with IRD of 58 % at 1050 °C, 1150 °C, 1250 °C, and 1350 °C.

Figure 6.30 Example of the deflected T-shape samples with IRD of 58 % at sintering temperatures of 1050 °C, 1150 °C, 1250 °C, and 1350 °C (from left to right).

The samples are 3D-scanned after the experiments. The beam deflection δ_{max} equals the difference between the top surface of the pillar and the top surface of the arm. Other than deflection, as presented by Eq. 6.9, the length L_a, width b_a, and thickness t_a are measured. The mass of the arm m_a is assumed to be constant and is analytically determined by the average size and density of all the specimens in green state. The determined mass is 2.54 g. The specimen's density after the sintering is determined by the MtV method. By considering the sintering time, the deflection rate with respect to temperature is presented in Fig. 6.31 for the given initial densities. To provide comparison, the deflection rate of the TOM specimen is also given in Fig. 6.31.

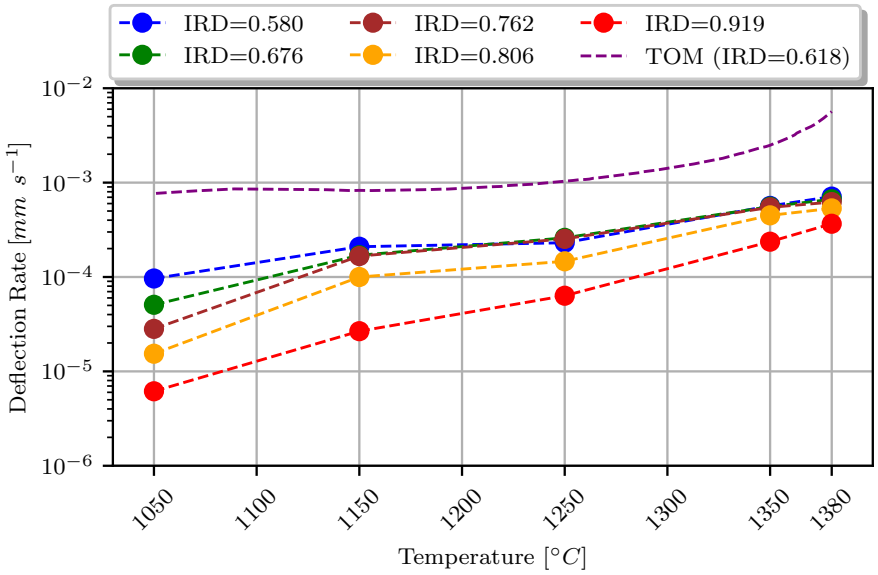

Figure 6.31 The deflection rate with respect to temperature for different IRD of the sintered T-shape samples.

6.2.2 Prediction of Green Part Properties

Green Part Density

The 3D interpolation method introduced in Sec. 4.3.2 is used to find a density field with respect to any given position within the print chamber. This results in the creation of the GPPF for density. Fig. 6.32 shows the green part density distribution for all cubes distributed in the XY, XZ, and YZ planes.

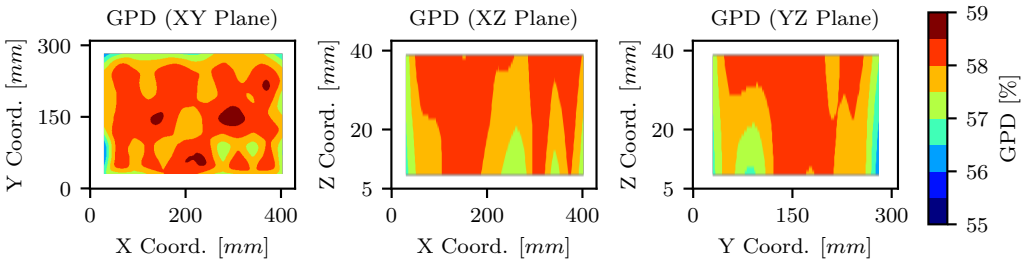

Figure 6.32 Green part density distribution of all cubes shown in the XY, XZ, and YZ planes, obtained by the 3D interpolation method from GPPF.

Green Part Dimensions

Analog to the green part density, the dimensional deviation map function is generated by the 3D interpolation method. Fig. 6.33 shows the deviations interpolated between all the collected cubes for any given coordinate for X, Y, and Z dimensions. Dimensional deviation from the ”target” status in the X, Y, and Z directions are plotted in Fig. 6.33a, 6.33b, and 6.33c, respectively. The figures plot each direction’s deviation in the XY, XZ, and YZ planes. To simplify the process, the center of gravity of desired parts should be given to the GPPF function, and as-print dimensions will be predicted.

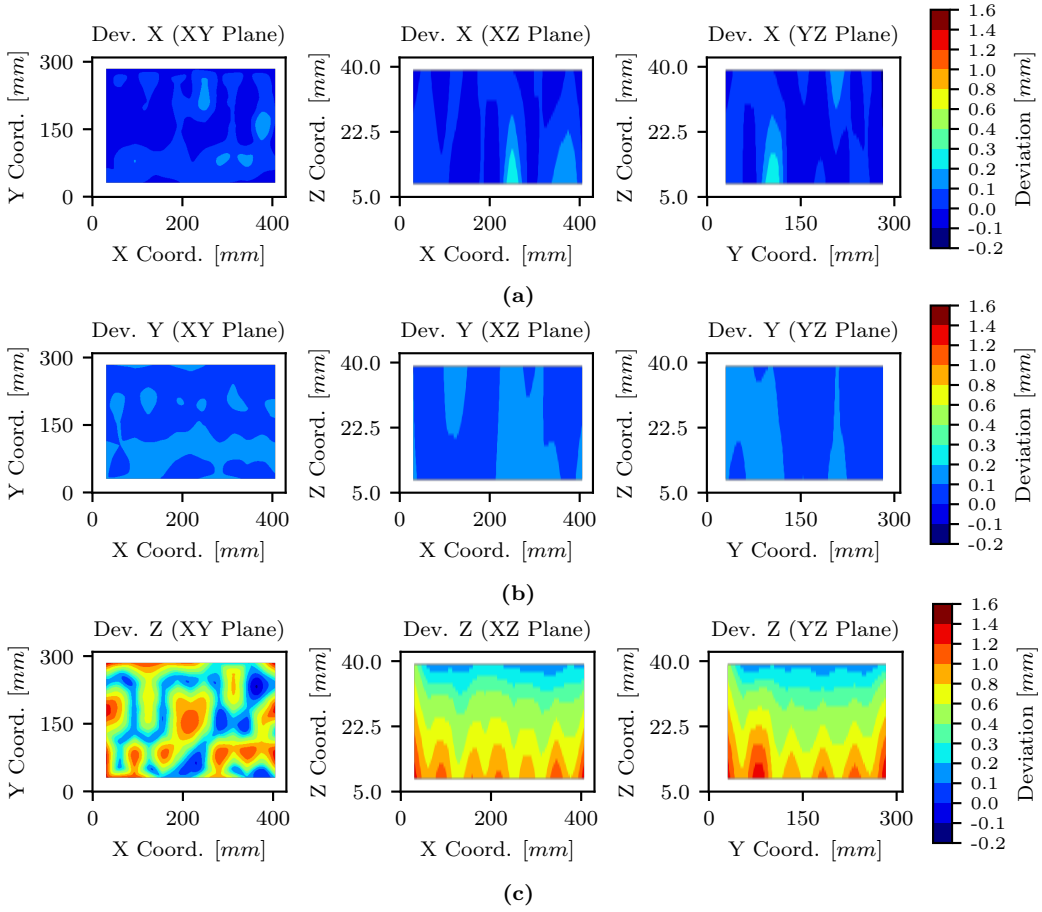

Figure 6.33 The dimensional deviation map for all collected cubes interpolated with respect to any given coordinate for (a): X, (b): Y, and (c): Z dimensions.

6.2.3 Generic Material Model

The required parameters to develop a generic material model for sintering deformation, including TEC, apparent viscosity, sintering anisotropy, GS evolution, and sinter stress, are presented in this section.

Thermal Expansion Coefficient

The introduced dilatometry experiments in Sec. 6.2.1 are used to determine TEC. For this purpose, first, the displacement behavior of the samples is classified into sintering and thermal expansion/shrinkage portion concerning the respective SAT for each cycle. The initial and final density of the samples, before and after the sintering, are assigned to the expansion and shrinkage fragments, respectively. The instantaneous TEC α_{tec} is calculated through Eq. 2.10 and then plotted with respect to temperature. For instance, the TEC values of cycle-1 are shown in Fig. 6.34. Appendix B contains the TEC values of the other cycles.

In the heating phase before the start of sintering, after a sudden TEC change at temperatures up to 160 °C, TEC increases gradually. As soon as densification is completed and during the cooling course, TEC is significantly higher than that of the green parts.

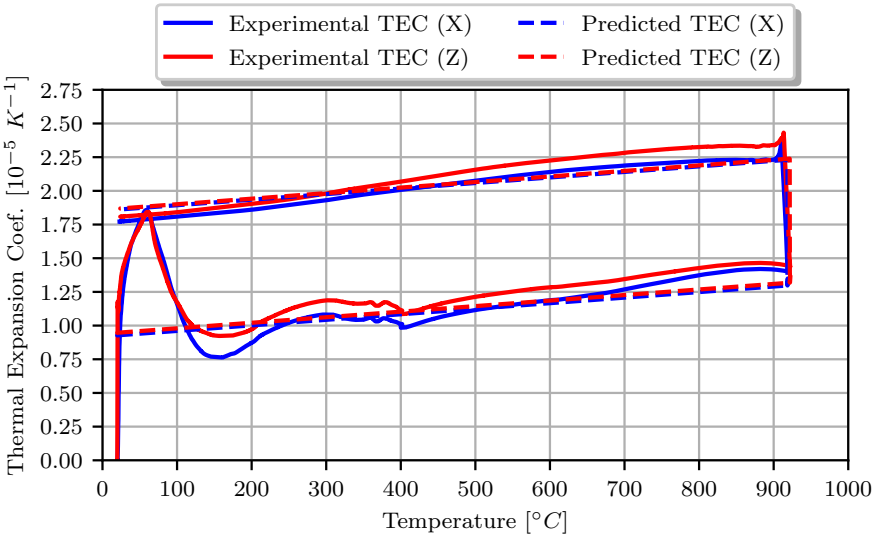

Figure 6.34 The instantaneous and predicted TEC values of X and Z specimens for cycle-1.

TEC can be explained as a function of relative density in percent and temperature as:

$$\alpha = b_{tec}\, T + p_{tec}\, \rho_{rel} + c_{tec}, \tag{6.10}$$

where b_{tec}, c_{tec}, and p_{tec} are material constants. The constants are determined as the average of the fitted values to all TEC curves and are given in Tab. 6.13. For the curve fitting process, the printing direction is irrelevant since no substantial difference is identified between the X and Z samples. The predicted TEC using the mentioned coefficients for cycle-1 is also given in Fig. 6.34.

b_{tec} $[°C^{-2}]$	p_{tec} $[°C^{-1}]$	c_{tec} $[°C^{-1}]$
4.110×10^{-9}	2.410×10^{-5}	-4.330×10^{-6}

Table 6.13 The material constants for the TEC as a function of relative density and temperature.

Apparent Viscosity

Fig. 6.35 displays the calculated apparent viscosity η_0 by Eq. 6.9 from the cross-shapes' deflection tests, exposed in Sec. 6.2.1. The values of apparent viscosity obtained from the cross-shapes' deflection tests are observed to be influenced by the initial density of the specimens. However, as seen in Eq. 2.14 and 2.15, the determination of shear and bulk viscosity of the porous sintering bodies requires the apparent viscosity of a fully dense material.

Hence, for the sake of generality, apparent viscosity should be determined for a fully dense material. Nevertheless, it is found that measuring the deflection of specimens with higher IRDs is more challenging. The reason for this difficulty is the high sensitivity of the viscosity values to deflection for specimens with higher IRDs, which exhibit slight deflection. Yet, a specimen with nearly full density was also tested using this method, and no substantial deflection could be observed. Consequently, the measured values for different IRDs are utilized and scaled to calculate the apparent viscosity.

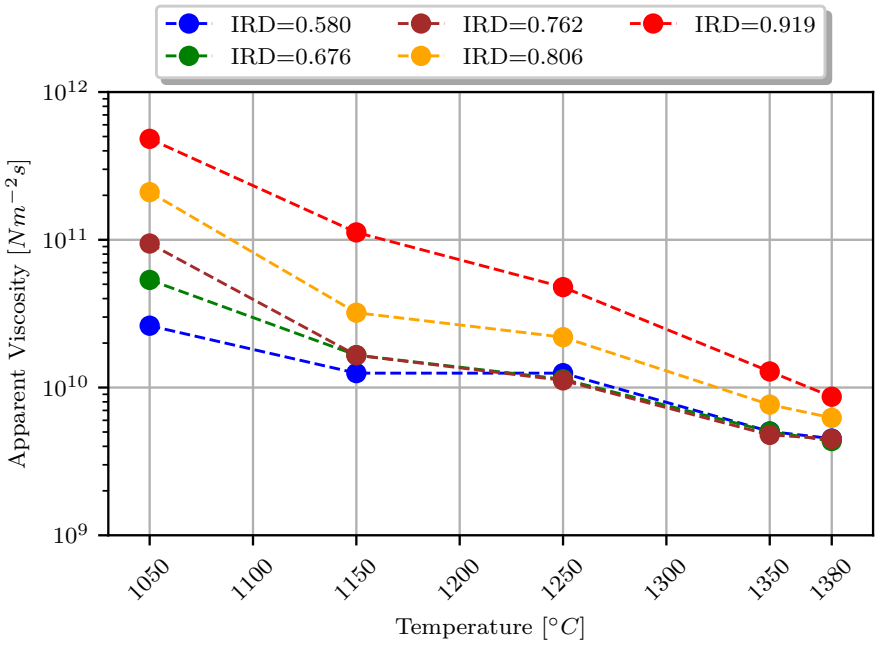

Figure 6.35 The calculated apparent viscosity from the cross-shapes deflection tests with different IRDs.

To mitigate the impact of density on apparent viscosity, a deviation band of 30 % from the average value at each temperature is established. Through a process of curve fitting, it is determined that all the apparent viscosity curves fall within the deviation band if they are divided by the 8^{th} root of the actual relative density, as shown in Fig. 6.36. This division factor helps normalize the viscosity values with respect to the density and ensures that the apparent viscosity remains within the defined deviation band. The resulted curves are named reference apparent viscosity η_{ref} for each IRD. It should be noticed that the unit of reference apparent viscosity η_{ref} is the same as that of the apparent viscosity η_0 since the relative density values are given in percent. In other words, the reference apparent viscosity η_{ref} is equivalent to apparent viscosity η_0 but normalized for all IRD values. The average of η_{ref} curves can be counted as η_0 of the fully dense material (IRD equals 1.0), which is independent of the IRD.

By fitting an exponential function to the experimentally determined η_0 of the fully dense material, apparent viscosity η_0 can be predicted for any temperature in the range of the study. For higher temperatures up to 1400 °C, the function is assumed to be valid in this study. The apparent viscosity function is presented as:

$$\eta_0 = \kappa_\eta \, exp\,[c_\eta T]\,, \tag{6.11}$$

where the values of κ_η and c_η are provided in Tab. 6.14.

κ_η	c_η
$[\mathrm{N\,m^{-2}\,s}]$	$[°\mathrm{C}^{-1}]$
5.580×10^{18}	-1.472×10^{-2}

Table 6.14 The calibrated material model constants to determine apparent viscosity with respect to temperature.

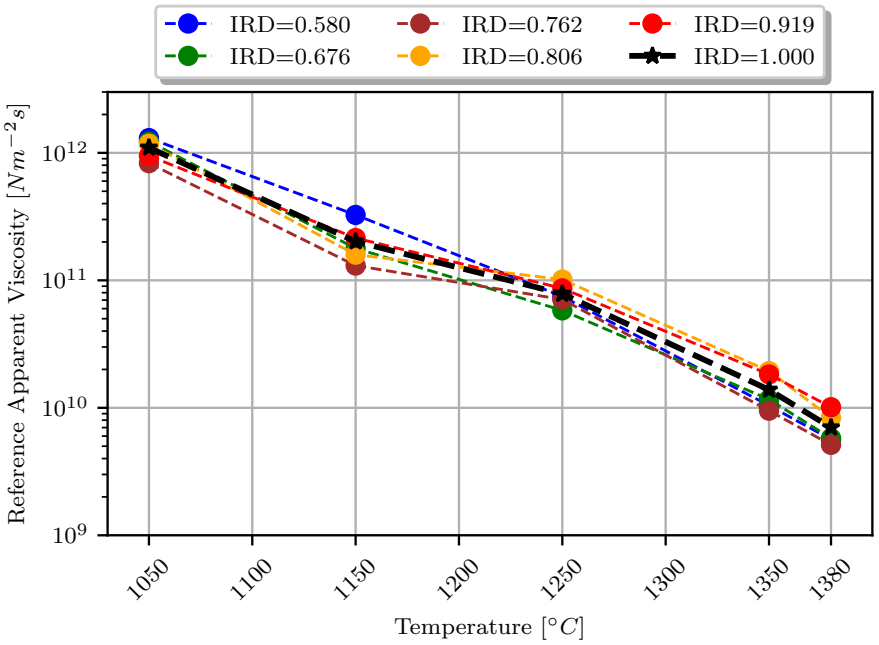

Figure 6.36 The reference apparent viscosity η_{ref} curves for different IRD values calculated through dividing the apparent viscosity η_0 by the 8^{th} root of the actual relative density.

Fig. 6.37 displays the determined apparent viscosity η_0 of fully dense material, along with the measured apparent viscosity of the different IRD values and the apparent viscosity calculated by a fitted exponential function. In addition, the diagram includes the calculated apparent viscosity η_0 with TOM for comparison purposes.

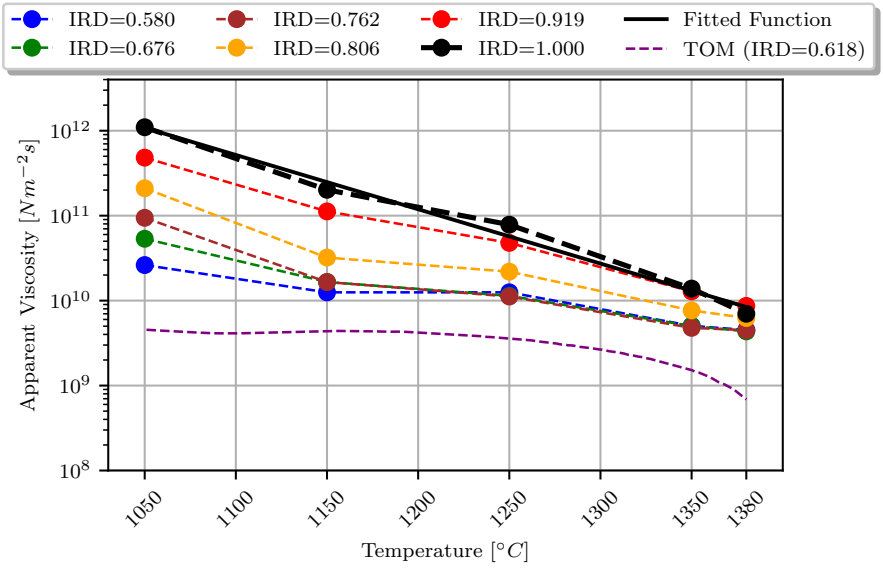

Figure 6.37 The final apparent viscosity η_0 of the fully dense material, the apparent viscosity calculated by a fitted exponential function, and the measured apparent viscosity values for different IRD values.

Sintering Anisotropy

Upon closer examination of the displacement curves of the sintering samples printed in the X and Z directions, as shown in Fig. 6.20, it has been observed that the X samples exhibit a higher shrinkage rate initially. However, as the specimens undergo further densification, the samples printed in Z exhibit a faster rate of shrinkage. This suggests that the anisotropic shrinkage of MBJ parts is a function of their density. By incorporating anisotropy factor W_{ij} into Eq. 6.12, the contribution of each normal component to the total viscoplastic strain rate is defined:

$$\dot{\epsilon}_{ij} = \frac{\sigma^{'}{}_{ij}}{2\eta_s} + W_{ij}\left[\frac{\sigma_m - \sigma_s}{3\eta_b}\right]\delta_{ij}. \tag{6.12}$$

W_{ij} represents the relation between shrinkage behavior in the X, Y, and Z directions. Thus, it is crucial to catch the anisotropy ratio with respect to a reference direction. In this study, the X direction is chosen as the reference, and W_{ij} is defined as below:

$$\begin{cases} W_{11} = \dfrac{\epsilon_{xx}}{\epsilon_{xx}} \\ W_{22} = \dfrac{\epsilon_{yy}}{\epsilon_{xx}} \\ W_{33} = \dfrac{\epsilon_{zz}}{\epsilon_{xx}}. \end{cases} \tag{6.13}$$

Since the displacement behavior in the X and Y directions is very close, W_{11} and W_{22} are assumed to be equal, and evidently, $W_{11} = 1$. To determine W_{33}, the displacement of Z samples is divided by the respective value of X samples in each cycle. The density evolution of samples is calculated purely by considering the shrinkage behavior in both directions to find the actual volume of the samples. That means the radial and axial dimensions of the specimens at any time are derived from the respective shrinkage curves. The anisotropy factor for all the cycles with respect to RD is shown in Fig. 6.38. The resulting curves are filtered to smooth impulse noises or spikes.

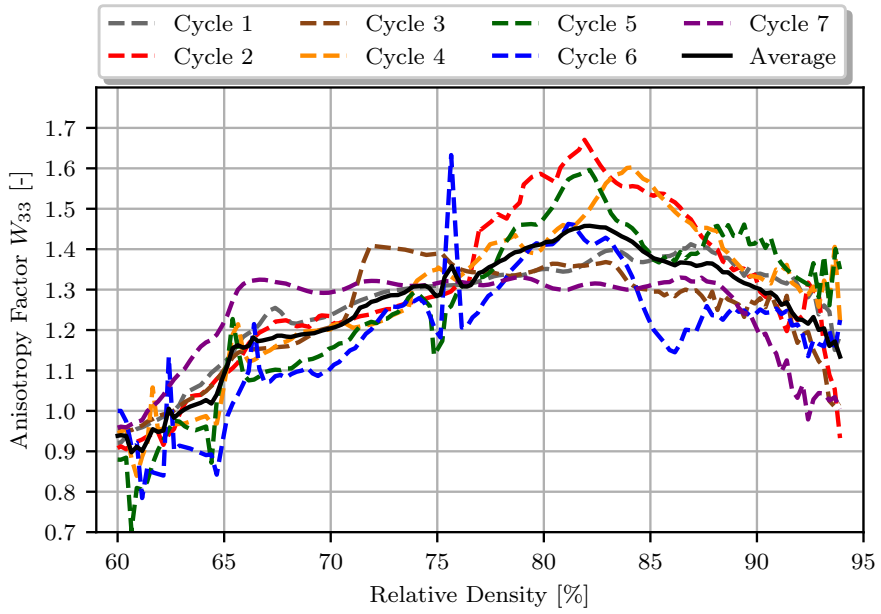

Figure 6.38 The anisotropy factor W_{33} for all the cycles as a function of RD. The curves are filtered to smooth impulse noises or spikes.

As the initial and final relative densities of the samples differ across different cycles, the anisotropy factor is analyzed over a range of 60 % to 94 %, where data is available for all the cycles. The average of the curves is considered as W_{33}, which can be modeled by a second-degree polynomial function of RD as below:

$$W_{33} = a_W \, \rho_{rel}^2 + b_W \, \rho_{rel} + c_W, \tag{6.14}$$

where the material constants a_W, b_W, and c_W are listed in Tab. 6.15.

a_W [−]	b_W [−]	c_W [−]
-11.7	19.0	-6.3

Table 6.15 Calibrated material model constants to determine sintering anisotopy factor W_{33} of MBJ samples with respect to RD.

Grain Size Evolution

The values of GS obtained from the experimental results, as presented in Tab. 6.11 and Tab. 6.12 are utilized to determine the parameters of the grain growth model described by Eq. 2.13. For this purpose, the thermal cycles are given to the equation, and the final GS is predicted. The model parameters are found in such a way that the GSs predicted by the model have the smallest distance from the respective experimental values. By assigning the Square Root of Mean Square Error as the error metric for predictions and by implementing of Response Surface Methodology, the material parameters are identified sequentially in LS-OPT [238]. Tab. 6.16 reveals the calibrated parameters.

Temperature [°C]	Q_g [kJ mol^{-1}]	A_g [10^{-10} m^2 s^{-1}]
$T < 1100$	316	2.28
$T \geq 1100$	108	2.28

Table 6.16 Calibrated parameters for the grain growth model used in the generic material model.

Sinter Stress

The given expressions for sinter stress in equations 2.16 and 6.3 should be calibrated for any new sintering cycle and GPP. To develop a more general expression, which is aligned with the classical theories of sintering, the following factors should be considered in the expression [19, 106, 110–112, 128, 148, 244, 245]:

- at higher temperatures, available surface energy increases,
- the available surface energy is dependent on the density of the material,
- as grains grow, available surface energy decreases,
- sinter stress is dependent on powder morphology and PSD.

According to the given points, a generic expression is developed for sinter stress as below:

$$\sigma_s = \frac{\beta \left(\frac{\rho_{rel}}{\rho_{ref}}\right)^{\Psi_\rho} \left(\frac{T}{T_{SAT}}\right)^{\Psi_T} \left(\frac{G}{G_0}\right)^{\Psi_G}}{G}, \tag{6.15}$$

where β is material constant, Ψ_ρ is the exponential factor for density, Ψ_T is the exponential factor for temperature, and Ψ_G is the exponential factor for GS. T_{SAT} is the average of the measured sintering activation temperatures presented in Tab. 6.12 and equals 946 °C.

The material constants are determined by minimizing the error between the measured and predicted displacement curve and the final density of all seven cycles. This is accomplished by formulating a multi-objective optimization problem and using Response Surface Methodology to identify the optimal material constants. The sintering stress Eq. 6.15 is used to calculate the responses (displacement curve and final density), taking into account the models for TEC, apparent viscosity, sintering anisotropy, and GS. The Square Root of Mean Square Error is used as the error metric, and the optimization process is performed using the LS-OPT software.

To simplify the expression, the material constants are defined in three stages: the initial, intermediate, and final stages of sintering. It should be noticed that the sintering stress is calibrated with the sintering dilatometry experiments of the specimens printed in the Z direction. The calibrated material constants are given in Tab. 6.17.

Relative density [%]	β [$\mathrm{N\,m^{-1}}$]	ρ_{ref} [%]	Ψ_ρ [–]	Ψ_T [–]	Ψ_G [–]
$RD < 65$	1.2	60	3.0	1.5	3.0
$65 \leq RD < 92$	0.3	60	3.0	1.5	1.3
$92 \leq RD$	28.3	60	3.0	1.5	-0.2

Table 6.17 The calibrated material constants for sinter stress in the generic material model of sintering deformation are categorized by the initial, intermediate, and final stages of sintering.

The calculated displacement curves of the cycles with the computed material constants are compared with the experimental results in Fig. 6.39. The debinding phase is excluded from the calculations and omitted from the experimental data to facilitate the comparison. In general, the calibrated generic material model is able to capture the deformation behavior during sintering with reasonable accuracy. However, the experimental data show more rapid densification during the intermediate stage, which may result in more significant deformations during sintering.

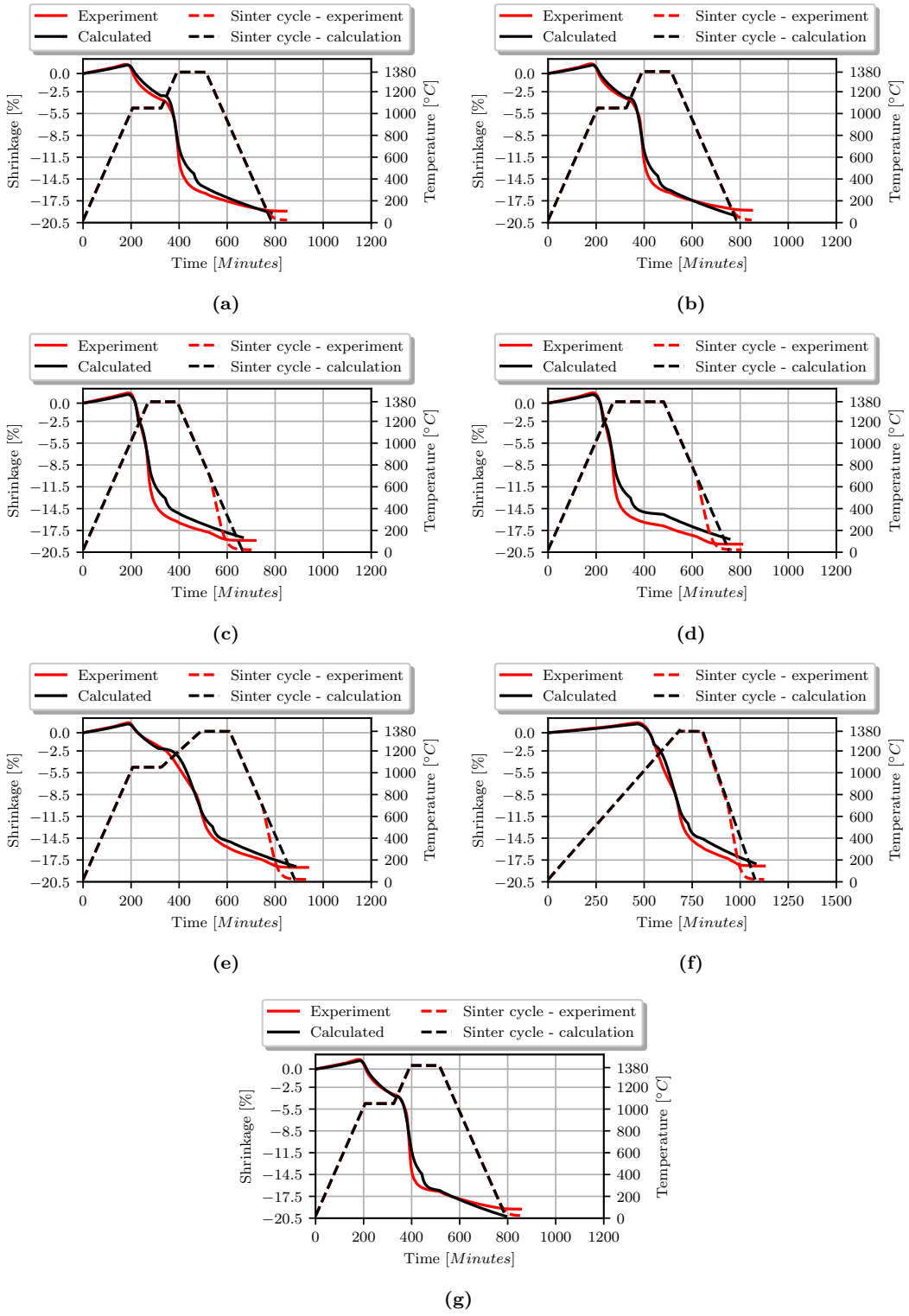

Figure 6.39 Comparison of calculated and experimental displacement curves for all seven cycles.

6.2.4 Material Model Adjustment

The previous subsection introduced a generic material model to calculate sintering displacement. Yet, due to the observed discrepancies in the experimental measurements, model fitting and calibrations, scalability from labor machines to workshop machines, as well as environmental and manufacturing changes, a further calibration step is presented here to increase the predictions' accuracy. According to this step, a T-shape geometry shown in Fig. 6.28 is manufactured with each new set of process parameters. The as-print and as-sinter dimensions of the specimens are measured and used for the final calibration. This approach offers a possibility to avoid time and cost-intensive labor measurements. It uses the proposed generic material model as a base for the final calibration with a simple experiment.

As stated in Sec. 6.1.4, apparent viscosity and sinter stress are two of the most influential parameters on predicted deformation and density. Thus, just these two parameters are modified to achieve higher accuracy. To keep the complexity of final calibration as low as possible, it is assumed that the introduced models in Sec. 6.2.3 maintain their fundamental structure and hold their core characteristics with respect to porosity and temperature. Consequently, by introducing the offset variable for viscosity λov and the offset variable for sinter stress λos, inspired by Eq. 6.7, the final calibration of apparent viscosity and sinter stress can be performed with the following equations:

$$\eta_0 = \lambda_{ov} \ \left[\kappa_\eta \, exp\left[c_\eta T\right]\right], \tag{6.16}$$

$$\sigma_s = \lambda_{os} \ \left[\frac{\beta \left(\frac{\rho_{rel}}{\rho_{ref}}\right)^{\Psi_\rho} \left(\frac{T}{T_{SAT}}\right)^{\Psi_T} \left(\frac{G}{G_0}\right)^{\Psi_G}}{G}\right]. \tag{6.17}$$

To find the values of λ_{ov} and λ_{os}, the T-shape geometry should be modeled with as-print dimensions and simulated with the desired sintering cycle. An iterative optimization algorithm is used to determine the values of λ_{ov} and λ_{os} such that the predicted dimensions and final density converge towards the experimentally measured dimensions, b_a, W_t, H_t, and δ as well as final density ρ.

6.3 Proof of Concept

In this section, the presented DDNS approach is implemented to assess the accuracy of the method in terms of density and dimensional accuracy after printing and sintering. For dimensional accuracy in as-print and as-sinter states, two geometries are chosen: a bracket-like and a reversed-U shape. Fig. 6.40 demonstrates the dimensions and printing direction of the geometries. In the former, warpage as a result of gravity, while in the latter, the effect of anisotropic shrinkage can be expected due to its height [28]. Furthermore, simple cubes are manufactured to assess the accuracy of estimations for GPP statistically. For analyzing the exactness of density predictions, just the cubes are inspected.

6.3.1 Accuracy of Predictions for Green Part Properties

The proposed method is used to find a density or dimensional deviation map within the print chamber for any given geometry. Nonetheless, with the available measuring systems, it is difficult to determine the density distribution of complex green parts. Therefore, the same standard cubes as those used in Sec. 6.2.1 are randomly distributed within 20 different print jobs for validations. Three to seven cubes are randomly placed within each print job based on available space. The densities and dimensional deviations of the validation cubes are then recorded in relation to their position within the print chamber.

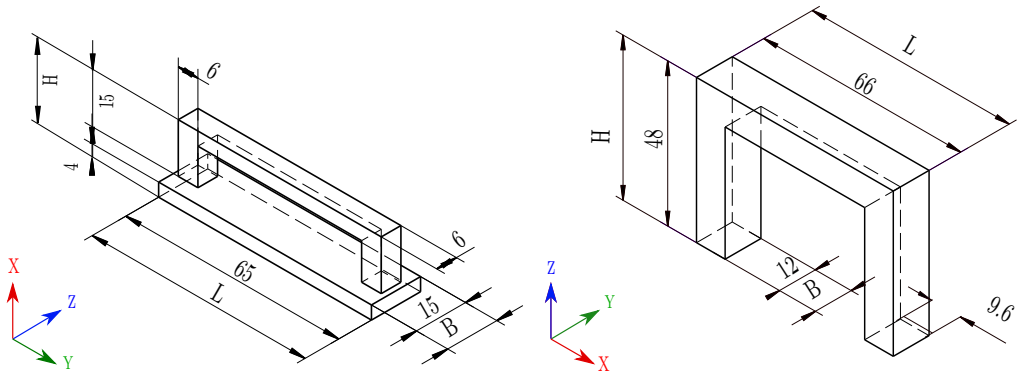

Figure 6.40 Illustration of the two geometries chosen for the assessment of the DDNS approach, (a): bracket-like geometry and (b): reversed-U geometry. The print orientation is detectable through the given coordination system for each geometry.

Density

Fig. 6.41 displays the density distribution of the validation cubes. In order to enable a comparable visualization with the initial data-collection method, the cubes are classified into two categories: level 1 for cubes with a positioning height of less than 30 mm and level 2 for cubes with a height of greater than 30 mm. It should be noted that due to the random positioning of validation cubes, some areas within the print chamber are not covered by the cubes.

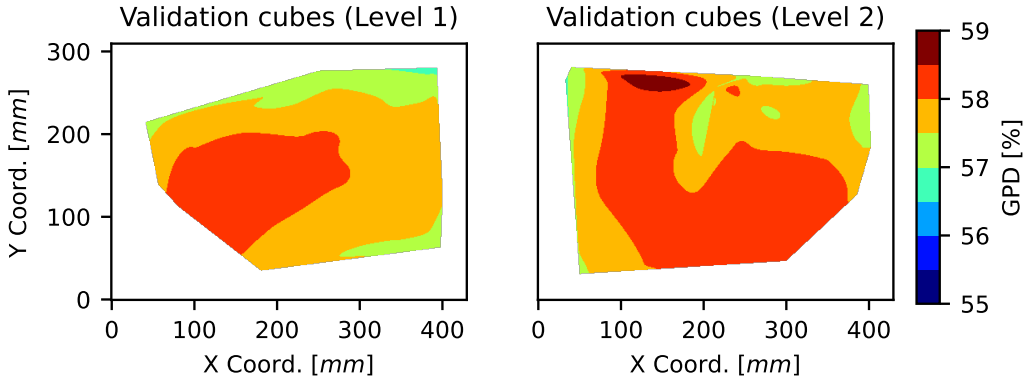

Figure 6.41 The density distribution of validation cubes is classified into two categories, (left): level 1 for cubes with a positioning height of less than 30 mm and (right): level 2 for cubes with a positioning height of greater than 30 mm.

To evaluate the accuracy of the method, a comparison is made between the conventional method and the proposed method in this study. In the conventional method, the average density value of previous experiments is considered GPD. In the data-driven method, not only GPD varies with respect to the part position, but also density variations within each part can be estimated. Fig. 6.42 and Fig. 6.43 enable the comparison between the two methods. In Fig. 6.42, validation cubes are compared with the average density (57.85 %) extracted from the initial data-collection cubes in Sec. 6.2.1. The comparisons are made in the XY, XZ, and YZ planes. The error between the estimated density by GPPF and the validation cubes is shown in Fig. 6.43. It should be noted that the absolute value of the deviations from the validation cubes is considered the error in all figures.

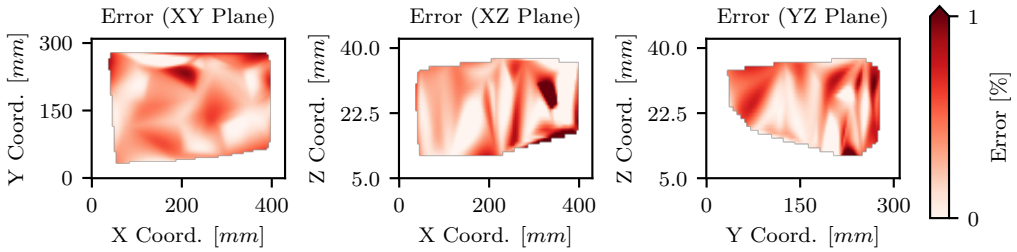

Figure 6.42 Deviation between the measured density of PoC cubes and the conventional method.

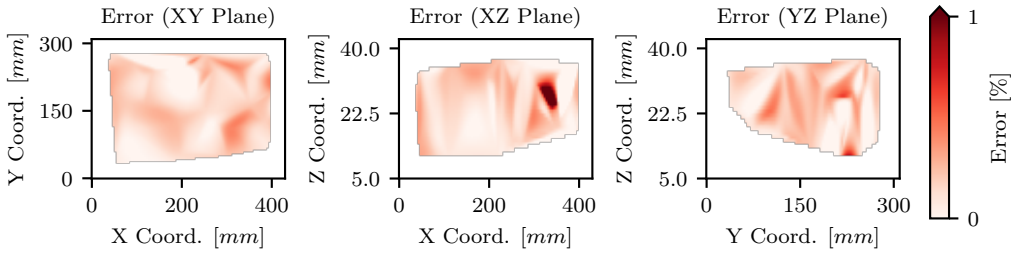

Figure 6.43 Deviation between the measured density of PoC cubes and GPD by GPPF.

The comparison of the error plots shows that the GPD estimation error in the GPPF approach is smaller than that of the conventional method. The average error in the conventional method is 0.35 % with 0.26 % StD, while the error drops to an average of 0.17 % with 0.10 % StD for the data-driven method.

Dimensions

Similar to density distribution plots, dimensional deviations of the validation cubes are represented in two levels. Fig. 6.44 shows the deviations in the X, Y, and Z directions sorted by print height.

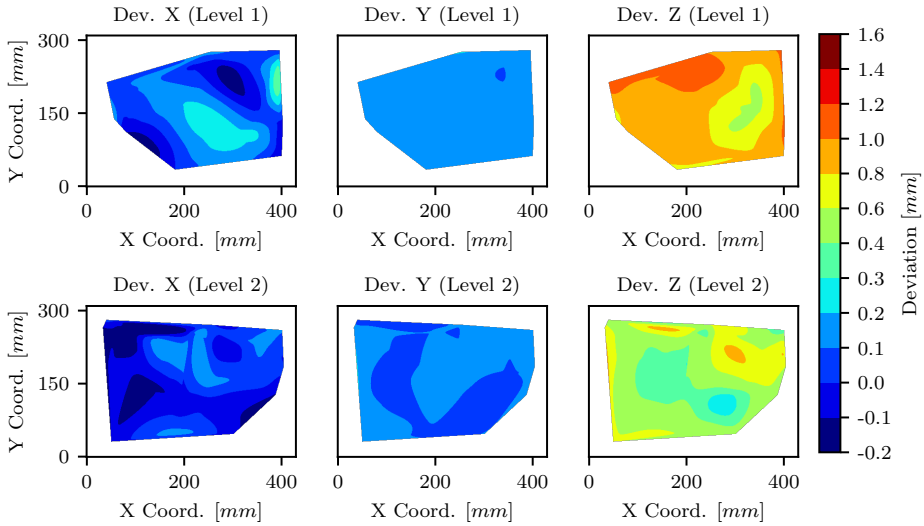

Figure 6.44 Dimensional deviations of the PoC cubes in the X, Y, and Z directions, sorted by print height. The distribution is shown in the XY layout of the printing chamber.

For assessing the accuracy of dimensional deviation predictions, the conventional method and the data-driven method (GPPF) are compared. For the conventional method, the average deviation of the initial data-collection cubes given in Tab. 6.9 is compared with the dimensional deviation values of the validation cubes. The accuracy of the conventional method is seen in Fig. 6.45. The prediction errors with the data-driven method are presented in Fig. 6.46 for the X, Y, and Z directions.

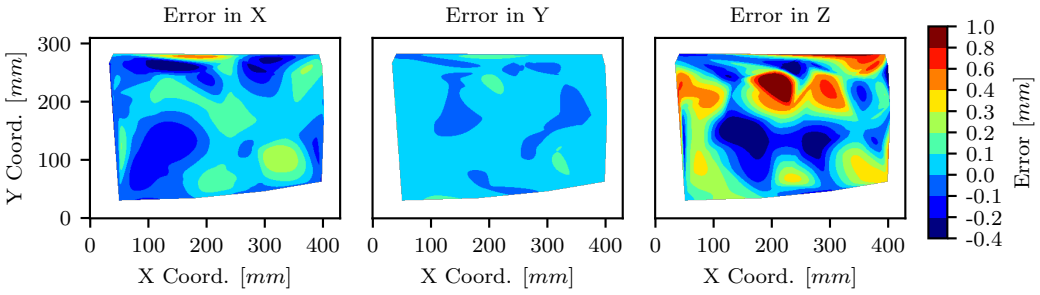

Figure 6.45 The accuracy of the conventional method in predicting the dimensional deviation of PoC cubes in the X, Y, and Z directions.

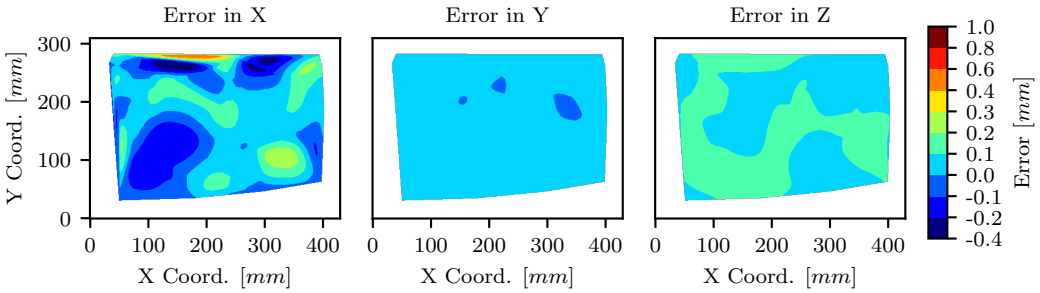

Figure 6.46 The prediction errors of the data-driven method (GPPF) for the X, Y, and Z directions.

Tab. 6.18 reveals the average and standard deviation of estimation errors between the conventional and data-driven methods. The given comparison in the heatmap figures and the standard deviation values explain that the estimation accuracy has been increased by the data-driven method for dimensional deviation in the Z direction. On the contrary, the predictions' accuracy remains unchanged for the X and Y directions.

Direction	**Conventional**		**Data-driven**	
	Average [mm]	StD [mm]	Average [mm]	StD [mm]
X	0.03	0.1	0.04	0.1
Y	0.04	0.03	0.05	0.02
Z	0.1	0.34	0.1	0.01

Table 6.18 The average and standard deviation of estimation errors between the conventional and data-driven (GPPF) methods for dimensional deviation.

Two bracket-like and two reversed-U specimens are printed for further accuracy studies. The bracket-like samples are printed so that the bridge parallels the Y axis, whereas the reversed-U geometries are printed

in a standing position. The printed parts are scanned and compared with the nominal dimensions. A Reference Point System (RPS) is defined for aligning the scanned data on the desired CAD geometries, which eliminates the exaggerated accuracy of the best-fit alignment method. Tab. 6.19 provides data regarding the coordinates of the Center of Gravity (CoG) for each sample within the print chamber, along with the as-print dimensions of the samples and the predicted dimensions obtained through the interpolation method.

Specimen	**CoG Coord.**	**As-print**			**Predicted**		
	[X, Y, Z]	L	B	H	L	B	H
	mm	mm	mm	mm	mm	mm	mm
Bracket-like 1	[297, 124, 37]	65.00	15.06	19.00	64.99	15.18	19.07
Bracket-like 2	[295, 248, 37]	65.01	15.16	19.04	65.01	15.21	19.07
Reversed-U 1	[232, 38, 27]	65.99	12.01	48.39	66.03	12.1	48.50
Reversed-U 2	[354, 200, 27]	66.01	12.04	48.29	66.01	12.08	48.41

Table 6.19 As-print and predicted dimensions of the bracket-like and reversed-U geometries.

Similar to the validation cubes, the deviations in the printhead and recoater directions (X and Y directions, respectively) for both bracket-like and reversed-U geometries are found to be insignificant. Therefore, to evaluate the accuracy of the proposed approach, the deviations in the build direction (Z axis) are considered, specifically the B dimension in the bracket-like geometries and the H dimension in the reversed-U geometries. Despite the fact that the interpolation function (GPPF) overestimates the actual dimensions for both geometries, it demonstrates an improved capability to predict dimensions with greater precision compared to exclusively considering nominal green dimensions.

6.3.2 Accuracy of Sintering Simulations

The DDNS model is incorporated into the FE solver Abaqus/CAE 2020, utilizing a coupled temperature-displacement analysis. To model the viscoplastic portion of the sintering deformation, the user-defined material models CREEP and USDFLD are utilized [227].

Bracket-like and reversed-U geometries are sintered with two different sintering cycles to inspect the ability of the DDNS approach. The first sintering cycle is cycle-1, already introduced in Sec. 6.2.1. The second chosen thermal regime is not identical to any of the previous cycles. To avoid any confusion with the previous cycles, this thermal cycle is called cycle-8. Both cycles are plotted in Fig. 6.47.

In order to apply the DDNS approach, it is necessary to perform a final calibration using T-shape samples for both sintering cycles. Two T-shape samples are printed and sintered using the workshop furnace with each cycle. The necessary dimensions for calibration are obtained by 3D-scanning, and the results are provided in Tab. 6.20.

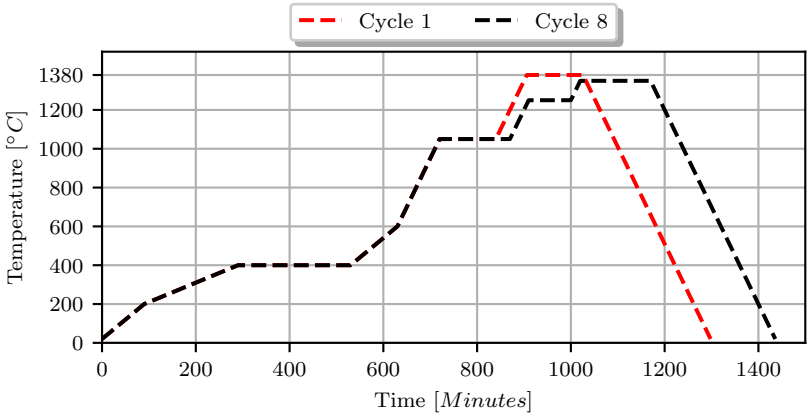

Figure 6.47 The thermal regimes of two different sintering cycles, used for sintering of bracket-like and reversed-U geometries to assess the accuracy of the DDNS approach.

Cycle	As-print					As-sinter				
	b_a [mm]	W_t [mm]	H_t [mm]	δ [mm]	GPD [%]	b_a [mm]	W_t [mm]	H_t [mm]	δ [mm]	SPD [%]
Cycle-1	10.02	9.02	24.18	0.03	58.6	8.49	7.65	19.85	4.9	97.8
Cycle-8	9.99	9.02	24.21	0.02	58.3	8.61	7.9	20.24	3.2	96.1

Table 6.20 The dimensions of the T-shape samples sintered with cycle-1 and cycle-8.

Cycle-8 involves a longer densification time at 1050 °C followed by another densification step at 1250 °C. In contrast, cycle-1 has a maximum sintering temperature of 1380 °C, which is higher than cycle-8's maximum temperature of 1350 °C. The apparent viscosity increases as densification occurs at lower temperatures, as shown in Fig. 6.37, resulting in a smaller arm deflection for the cycle-8 sample. Additionally, there is a noticeable difference in the achieved SPD between the workshop furnace and dilatometry experiments for cycle-1, with the sample exhibiting an SPD of approximately 98 %, which is higher than the 95 % SPD obtained from dilatometry samples.

Using the measured dimensions of the T-shape parts, the offset variables λ_{ov} and λ_{os} in Eq. 6.16 and Eq. 6.17 are determined. The calibrated offset variables are employed to simulate the bracket-like and reversed-U samples with the respective sintering cycles. Based on the CoG coordinates and the enveloped space of the geometries in the print chamber, inhomogeneous density fields are taken from the GPPF and assigned randomly to the input green parts for simulations. The initial dimensions of the green parts are also adjusted with appropriate scaling factors to match the given predicted values in Tab. 6.19. The calibrated values of λ_{ov} and λ_{os} for cycle-1 and cycle-8, as well as the range of GPD for each sample, are provided in Tab. 6.21.

FE models of the samples are prepared with the indicated data. Since the printing and sintering direction of the bracket-shape samples are not identical, anisotropy factors are adjusted accordingly. The generated FE decks are simulated with the respective sintering cycles. Then, the manufactured green parts are sintered with the planned sintering cycles, scanned, and later metallographically analyzed to evaluate the simulation results.

Specimen	GPD range	Sintering cycle	λ_{ov}	λ_{os}
	[%]		[−]	[−]
Bracket-like 1	[58.1, 58.4]	Cycle-1	0.9	1
Bracket-like 2	[57.8, 58.1]	Cycle-8	1.9	2.1
Reversed-U 1	[57.4, 58.3]	Cycle-1	0.9	1
Reversed-U 2	[57.6, 58.2]	Cycle-8	1.9	2.1

Table 6.21 Considered GPD of the samples and the determined values of λ_{ov} and λ_{os} for cycle-1 and cycle-8.

Final Density

According to the results depicted in Fig. 6.48, the cross-sectional analysis of the bracket-like specimens, conducted in the midpoint of the samples, reveals that the sample sintered with cycle-1 reaches an SPD of about 97.9 %, while the one with cycle-8 densifies to 96.0 %. The predicted densities by simulations are 98.4 % and 96.3 % for the cycle-1 sample and the cycle-8 sample, respectively.

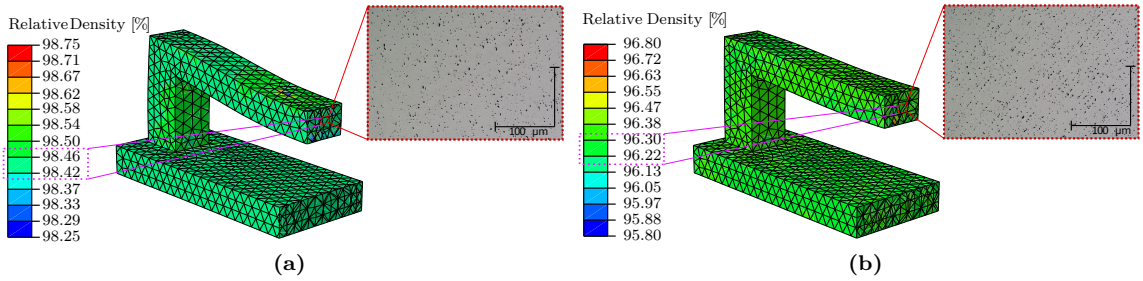

Figure 6.48 Predicted density of the bracket-like geometry compared with metallographic evidence on the displayed cross-section for (a): cycle-1 and (b): cycle-8.

Fig. 6.49 presents the results of the density analysis conducted on the reversed-U samples. The sample sintered with cycle-1 exhibits a mid-section density of approximately 98.5 %, while the cycle-8 sample achieves a density of around 96.6 %. Simulations of the cycle-1 and cycle-8 models predict densities of 98.0 % and 96.3 %, respectively. The simulation results align well with the experimental findings across all the conducted investigations.

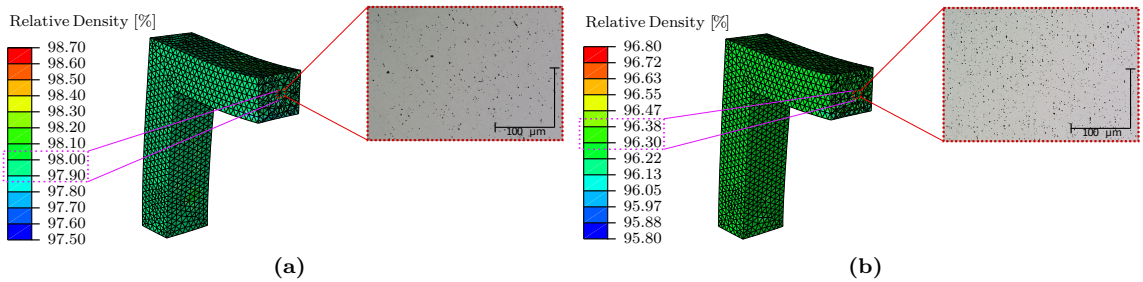

Figure 6.49 Predicted density of the reversed-U geometry compared with metallographic evidence on the displayed cross-section for (a): cycle-1 and (b): cycle-8.

Dimensional Accuracy

The comparison between the predictions by simulations and the sintered samples is presented in Fig. 6.50. A tight tolerance of 0.5 mm is considered for the accuracy analysis. The RPS approach is utilized for aligning the scan data on the simulation predictions.

The results of the surface deviation analysis confirm the accuracy of predictions. All four predictions fulfill the prescribed tolerance. The predicted deformation of the reversed-U samples touches the tolerance limit, particularly near the legs where the specimen is in contact with the sinter-setter. (See Fig. 6.50c and Fig. 6.50d for cycle-1 and cycle-8, respectively.) The complex interaction of friction and gravity causes significant nonlinear deformations in those areas, making the predictions more challenging.

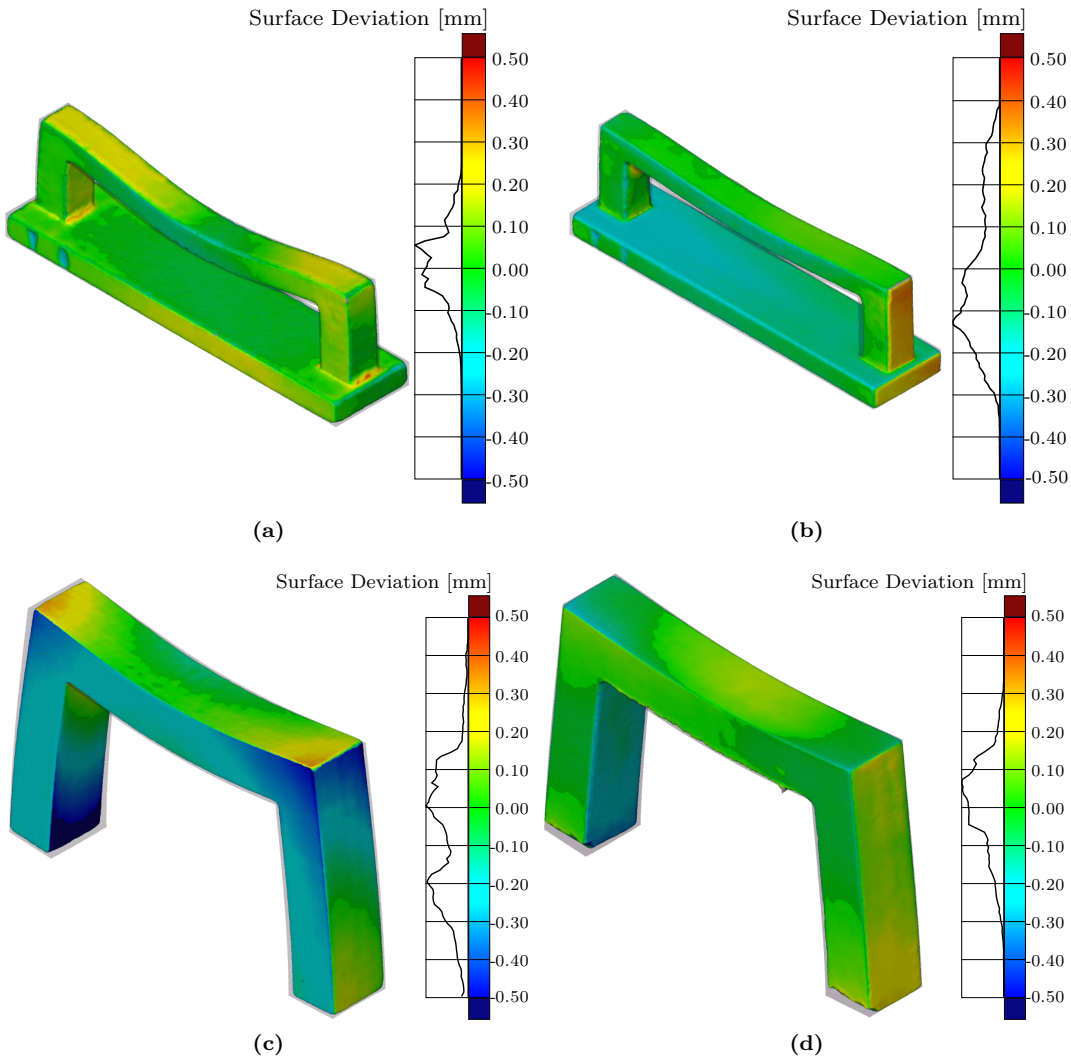

Figure 6.50 Deviation analysis between the predicted deformations and as-sinter samples (a): bracket-like geometry sintered with cycle-1, (b): bracket-like geometry sintered with cycle-8, (c): reversed-U geometry sintered with cycle-1, and (d): reversed-U geometry sintered with cycle-8.

6.4 Conclusion

The SOVS material model was calibrated inclusively for MBJ with various experiments such as thermo-optical cyclic loading, metallographic analyses, and dilatometry experiments. Using the calibrated material model, the sintering deformation of two samples was predicted using FE analysis. However, the accuracy of the predictions did not meet a tolerance of 1 mm, particularly for larger geometries. A sensitivity analysis of the model revealed that GPD, sinter stress, and apparent viscosity are key factors affecting sintering deformation and final density. Additionally, the anisotropic densification of MBJ parts and the dimensional accuracy of green parts can also impact final dimensions.

Based on the results of these analyses, a data-driven material model was constructed to predict sintering deformation using the SOVS model. The model estimates GPD and dimensions through an interpolation function that was established using data collected from multiple printed cubes across the print chamber. This interpolation map was then validated using cubes, a bracket-like geometry, and a reversed-U geometry. Results showed that the accuracy of density estimations for green parts improved when compared with conventional averaging methods. The interpolation function overestimated the dimensions of the bracket-like and reversed-U samples in the build direction; nonetheless, it provided a higher predictive precision than reliance solely on nominal green dimensions.

To propose a more generic model of sintering deformation, multiple dilatometry and sequential discontinuous sintering deflection experiments were conducted. A final tuning method was suggested to improve the accuracy of the model and adjust it for new manufacturing parameters. Both samples used for the validation of the interpolation function were sintered with two different cycles to assess the accuracy of the sintering deformation model. The simulations' predicted deformations were found to be within a tolerance of 0.5 mm from the experimental samples for both geometries.

Chapter 7

Compensation for Sintering Deformation

In the previous chapter, the DDNS approach was presented to capture the deformation of parts during sintering. In this chapter, a procedure is developed to compensate for sintering deformations and achieve dimensionally accurate MBJ parts. For this purpose, in the first section, an algorithm is introduced, which iteratively compensates for the predicted deformations by numerical simulations. In the second section, a compensation scheme is presented, which takes advantage of experimental data to achieve tighter dimensional tolerances. Both approaches are then validated by MBJ samples, and finally, a summary of the chapter is given.

7.1 Numerical-based Compensation

An iterative computational framework is given to compensate for sintering deformations. In the first iteration, sintering geometry S_0 is discretized, and the respective FE model M_0 is passed to the DDNS deformation function Γ. As a result, a corresponding deformation map function δ is given. In the iterative computational framework, δ_i is the resulting deformation map of the i^{th} iteration number of the compensations, which generates the FE model of M_i. For the first iteration, this can be formulated by:

$$\begin{cases} \Gamma(M_0) = M_{0\to1} \\ \delta_1(n_0^j) = n_{0\to1}^j, \end{cases} \tag{7.1}$$

where $M_{0\to1}$ is the first deformed FE model, δ_1 is the first deformation map function, n_0^j is the j^{th} node number of the initial FE model, and $n_{0\to1}^j$ is the j^{th} node of the first deformed FE model $M_{0\to1}$. A displacement field ξ_i^j is extracted from the deformation map function δ_i for each node j. Through reversing the displacement field, the updated node n_{i+1}^j in the FE model M_{i+1}, corresponding to the node n_i^j in the FE model M_i, is obtained by:

$$n_i^j - \xi_{i+1}^j = n_{i+1}^j. \tag{7.2}$$

The updated configuration is simulated again with the same boundary conditions. This iterative process continues until an error or convergence criteria is met. Using the Root Mean Square (RMS) method, the deviation between the target configuration (equivalent to M_0) and the current configuration in iteration i can be computed. The RMS error in the X, Y, and Z directions for each iteration is calculated by:

$$\begin{cases} \overline{err}_x = \dfrac{\sum_{j=1}^{N}(x_i^j - x_0^j)}{N} \\ \overline{err}_y = \dfrac{\sum_{j=1}^{N}(y_i^j - y_0^j)}{N} \\ \overline{err}_z = \dfrac{\sum_{j=1}^{N}(z_i^j - z_0^j)}{N}, \end{cases} \tag{7.3}$$

where N is the number of nodes in the FE model, and the overall RMS error is defined by:

$$err_{RMS} = \sqrt{\frac{(\overline{err}_x^2 + \overline{err}_y^2 + \overline{err}_z^2)}{3}}. \tag{7.4}$$

This process continues until an error criterion is met. A user-defined value is set as the threshold for maximum allowable deviation and is compared at each iteration with RMS error. After achieving the convergence criteria, the FE model resulting from the last iteration is the pre-deformed or compensated model of M_0.

For the implementation of the algorithm, after each simulation run, the displacement vectors are read and reversed by a PYTHON script; consequently, the next FE model is prepared. As soon as the defined deviation threshold is achieved, the compensated vectors are imported into ANSA, and the vectors are mapped to the initial CAD geometry S_0. By using the morphing function in ANSA, the respective compensated geometry S_i^{-1} (also alternatively called CAD^{-1} of S_0) is generated, where i denotes the iteration number of the compensation process. In this stage, the CAD model S_i^{-1} can be printed and consequently sintered. The resulting sintered geometry is expected to lay within an acceptable tolerance range from the target geometry S_0 after undergoing sintering-induced deformations. The procedure of the numerical compensation approach is given in Fig. 7.1.

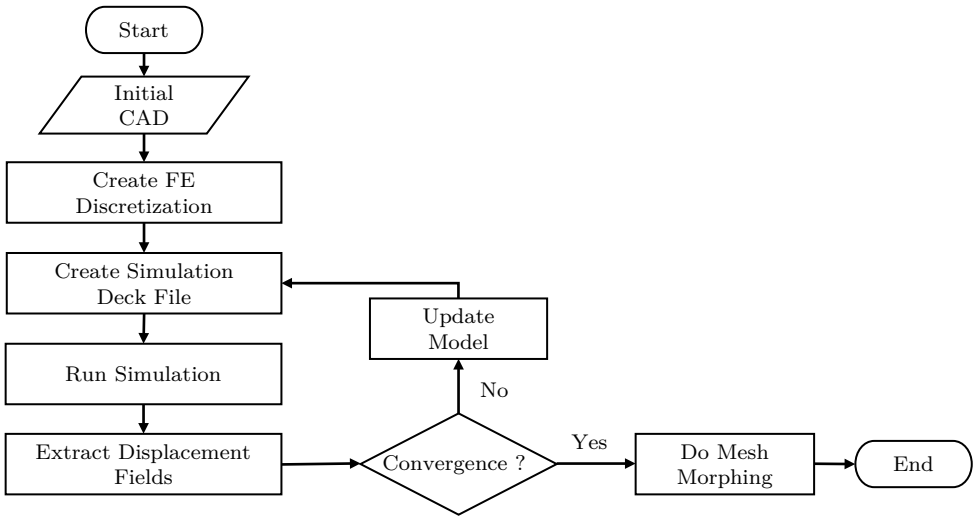

Figure 7.1 The algorithm for the numerical-based compensation.

7.2 Experimental-based Compensation

Followed by a numerically compensated geometry, a further pre-deformation step based on experimental data can be carried out to achieve higher dimensional accuracy. In this connection, the numerically compensated S_i model is manufactured; the as-sinter configuration is scanned and labeled as S_i'.

To prepare an experimental-based compensated model, the as-sinter configuration S_i' is aligned with the target geometry S_0 using the RPS approach. Then, the deviation vectors between the target and as-sinter states are extracted. The deviation vectors are reversed and mapped to the latest compensated model S_i^{-1}, which previously had led to S_i'.

To compute the deviation vectors between the target and as-sinter geometries, a technique that utilizes the ray tracing approach and is a widely-used method in 3D computer graphics can be employed [246, 247]. The underlying principle of the technique is to trace a ray from a point of interest P on surface S_0 and detect its intersection with surface S_i'. The intersected tracing ray can determine the deviation vectors between both geometries. Assume a target surface S_0 and the respective manufactured surface S_i' in Fig. 7.2a.

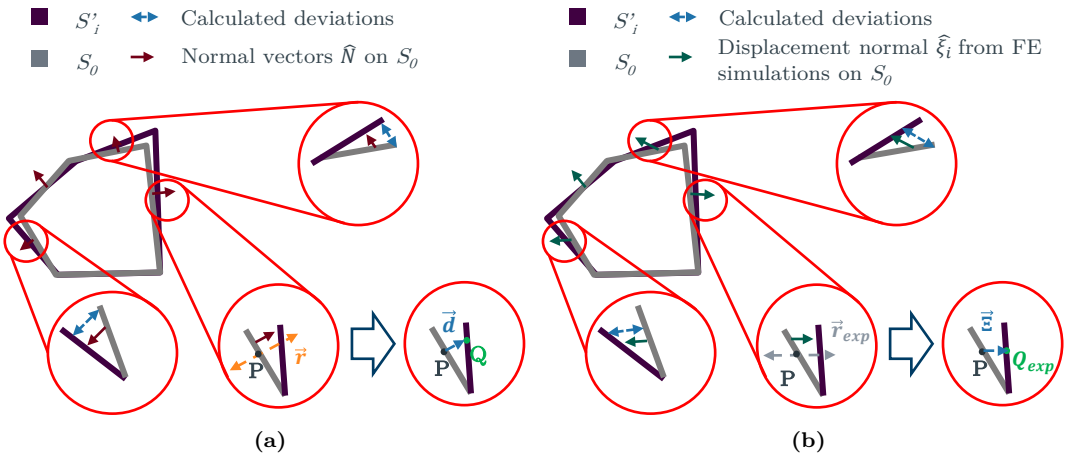

Figure 7.2 Finding deviation between target and as-sinter geometries with (a): the ray tracing approach and (b): with the help of displacement vectors from the numerical simulations.

According to the ray tracing approach, the distance between the point P and surface S_i' equals the length of the emitted ray from the point P to the point of intersection on surface S_i'. To compute the distance, the given steps should be followed:

1. Trace a ray from the point of interest P in the direction of $\hat{N}$ towards surface S_i'. $\hat{N}$ is the normal unit vector of surface S_0 at point P.

$$\vec{r} = P + t\,\hat{N}, \tag{7.5}$$

   where $\vec{r}$ is the ray and t is a parameter that controls the range of the ray.
2. Find the intersection of the ray with S_i' with an intersection algorithm such as those developed by [248–250].
3. If the ray intersects surface S_i' at point Q, the deviation between P and surface S_i' is defined by the vector from P to Q.

$$\vec{d} = Q - P, \tag{7.6}$$

   where $\vec{d}$ is the deviation vector between P and S_i'.

The accuracy of the compensation process can be increased if the deviation vectors are determined in such a way that they replicate the nature of shrinkage and warpage in the sintering process. To enable this, the direction of the tracing rays (unit normal vector $\hat{N}$ of surface S_0 in the original version) is substituted by the normalized displacement vectors $\hat{\xi}_i$ from the last compensation iteration i of numerical simulation (See Fig. 7.2b). Finally, using the unit displacement vectors $\hat{\xi}_i$, Eq. 7.5 and Eq. 7.6 can be respectively rewritten as below:

$$\vec{r}_{exp} = P + t\,\hat{\xi}_i, \tag{7.7}$$

and

$$\vec{\Xi}_{exp} = Q_{exp} - P, \tag{7.8}$$

where $\vec{r}_{exp}$ is the ray in the direction of the unit displacement vector $\hat{\xi}_i$ on point P, Q_{exp} is the resulting point of intersection between the ray $\vec{r}_{exp}$ and S_i', and $\vec{\Xi}_{exp}$ is the determined deviation vector between P and S_i'. The deviation vectors $\vec{\Xi}_{exp}$ are reversed and superimposed with the reversed displacement vectors $\vec{\xi}_i^{-1}$ extracted from the last iteration of the numerically compensated model M_i. The resulting vectors are mapped on the initial CAD geometry S_0, and an experimentally-based compensated CAD model of S_{i-exp}^{-1} is prepared.

7.3 Proof of Concept

In this section, two crash reinforcement parts are considered for the validation study of compensation methods. Part-A and part-B are demonstrated in Fig. 7.3 and Fig. 7.4, respectively.

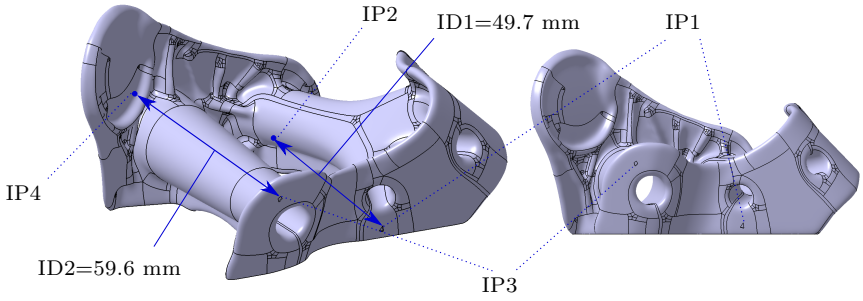

Figure 7.3 Crash reinforcement part-A .

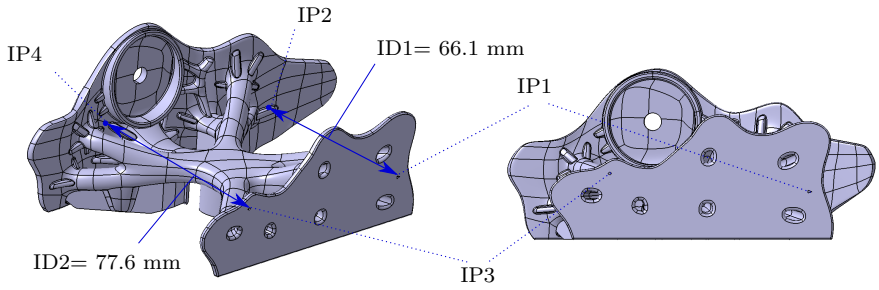

Figure 7.4 Crash reinforcement part-B.

To inspect the dimensional accuracy of the parts and due to the complexity of the geometries, a shape-coining method is used to easily mark any Inspection Point (IP) after printing and sintering. Four IPs are defined on each geometry. The IPs are connected in a pairwise manner via an imaginary line to construct Inspection Dimension (ID). Furthermore, RPS points are defined for the alignment of the parts. The compensated CAD of part-A will be printed at the CoG coordinate of [139, 204, 38] mm, while part-B at [215, 60, 43.5] mm.

At first, both geometries are numerically compensated and the results are compared with the experimental evidence. In the numerical-based compensation section, an International Tolerance (IT) grade of 14 is chosen for deviation analysis [251], which is an acceptable grade in metal AM [252–254]. To achieve tighter tolerances and fulfilling an IT13 grade standard, one of the parts is experimentally compensated, manufactured again, and checked for dimensional accuracy. The tolerance values are found in mm for IT13 and IT14 grades by considering the largest dimension of the parts in the direction of the respective IDs. The dimension of both parts in the ID-direction lies within a range of 50 mm to 80 mm, resulting in allowable tolerance of 0.74 mm in IT14 grade and 0.46 mm in IT13 grade [251].

7.3.1 Numerical-based Compensation

The GPD ranges, as well as the printing scale factors according to the CoG coordinates, are first extracted from GPPF. The corresponding DDNS model, including the λ_{ov} and λ_{os} factors for cycle-1, is used for the simulations. A deviation threshold of 0.01 mm is considered for the compensation algorithm. Fig. 7.5 plots the procedure of the compensations schematically for part-A. For the numerical compensation stage, first, the initial CAD model is discretized, and sintering deformation simulation is performed with given material model constants as well as thermal cycle. The compensation process is performed alliteratively until the desired deviation threshold is achieved. Subsequently, the deformation vectors are morphed on the CAD model, and the part is manufactured. Finally, the manufactured part is scanned, and a deviation analysis is performed.

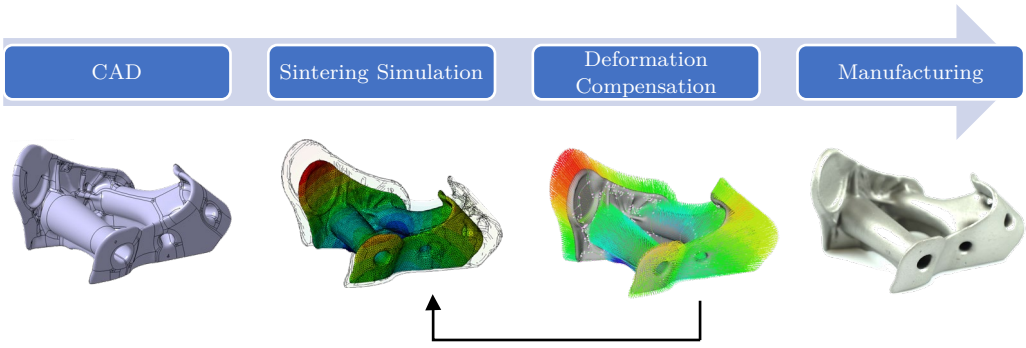

Figure 7.5 Numerical-based compensation workaround on part-A.

Three iterations are required for both geometries to reach the defined deviation threshold, and consequently, the compensated CAD_3^{-1} models are prepared. The subscript 3 refers to the iteration number from which the displacement vectors are extracted. The compensated CAD_3^{-1} models are manufactured, as visible in Fig. 7.6.

(a) **(b)**

Figure 7.6 (a): The manufactured part-A and (b): the manufactured part-B.

The sintered parts are scanned and compared with the target model, as seen in Fig. 7.7 for part-A and in Fig. 7.8 for part-B. Each figure contains an absolute dimension control with the predefined IDs and a surface deviation analysis. The maximum and minimum deviation values on the legends are set to $\pm 0.74\,\text{mm}$, which is equal to the IT14 grade.

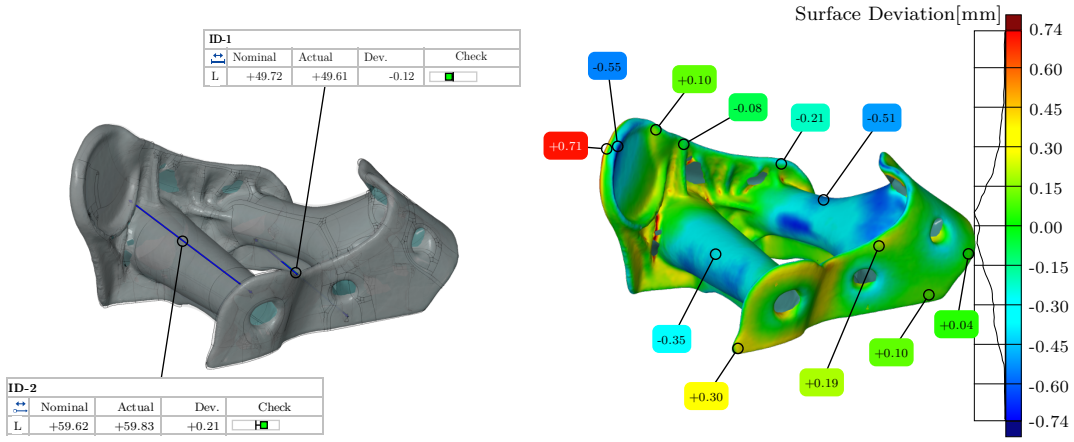

(a) **(b)**

Figure 7.7 Dimensional accuracy control of part-A, compensated by the numerical-based approach; (a): absolute dimension control with the predefined IDs and (b): surface deviation analysis.

The monitoring of surface deviation outcomes and ID controls confirm that the fabricated geometries resulting from the compensated CAD_3^{-1} models are within the prescribed tolerance limits. This demonstrates that the compensation approach based on numerical analysis is capable of compensating for the deformation that occurs during the sintering of industrial parts while ensuring that the resulting dimensions conform to the specified IT14 grade.

Despite meeting the required level of accuracy, a significant deviation persists in part-A near the area with $+0.71\,\text{mm}$ deviation label, which almost touches the tolerance limit. This region experiences substantial deformation due to inadequate support from below and is also susceptible to buckling phenomena arising from the thin walls. The discrepancy between the compensated geometry and the target geometry can be attributed to the inadequacy of the simulations with the given element sizes and material model, as they do not fully capture the aforementioned effects. In the case of part-B, deviation labels with absolute values of about $0.70\,\text{mm}$ are also observed. However, this is related to the surface quality of the scan data and the generated local bulges during the scan-data processing.

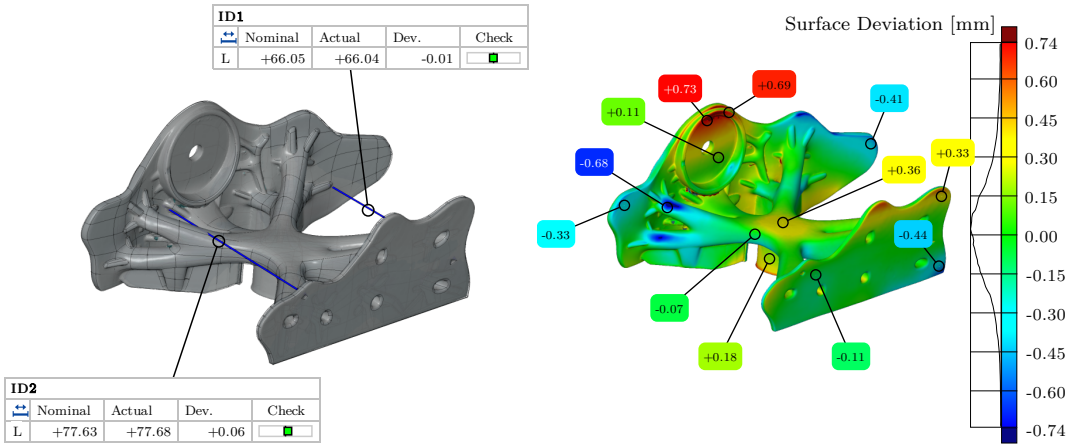

(a) **(b)**

Figure 7.8 Dimensional accuracy control of part-B, compensated by the numerical-based approach; (a): absolute dimension control with the predefined IDs and (b): surface deviation analysis.

7.3.2 Experimental-based Compensation

Part-A is chosen for further optimization in terms of dimensional accuracy. The scanned data in the previous step is compared with the target geometry. As explained in Sec. 7.2, the deviation vectors from the target geometry are calculated and reversed. The reversed vectors are mapped to the CAD_3^{-1} model, and the subsequent CAD_{3-exp}^{-1} is created.

The CAD_{3-exp}^{-1} model is printed in the same position as CAD_3^{-1} and sintered again. The surface deviation comparison between the sintered geometry and the target CAD is made in Fig. 7.9. The figure shows that the manufactured part reaches an IT13 grade.

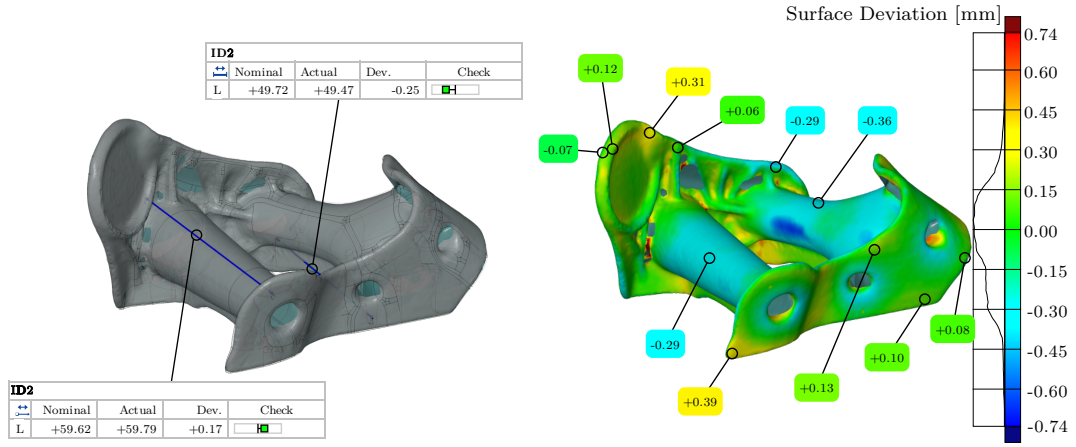

(a) **(b)**

Figure 7.9 Dimensional accuracy control of part-A, compensated by the experimental-based approach; (a): absolute dimension control with the predefined IDs and (b): surface deviation analysis.

To demonstrate the enhancement of dimensional accuracy resulting from an additional fine compensation via the experimental-based approach, a comparison is made between the surface deviation analysis of two configurations: one utilizing the purely numerical-based method and the other utilizing the additional experimental-based approach. The results of this comparison are presented side-by-side in Fig. 7.10 with an IT14 legend. Fig. 7.10a shows the results of the purely numerical-based method, while Fig. 7.10b depicts those with the additional compensation step using the experimental-based approach.

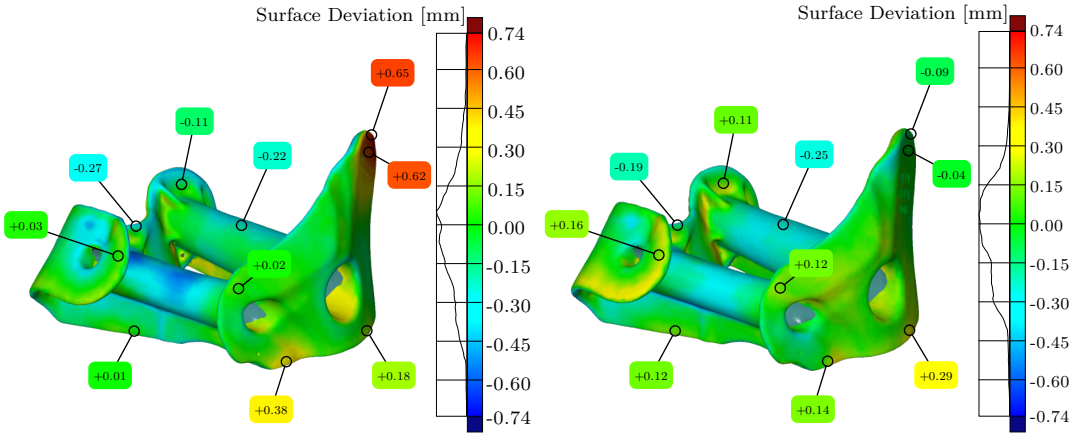

Figure 7.10 Surface deviation analysis of part-A, (a): with numerical-based approach and (b): with experimental-based approach.

7.4 Conclusion

A method was developed to compensate for sintering deformation with two approaches, a numerical-based method and an experimental-based one. The former approach entails discretizing the sintering geometry and passing it to a deformation function calculated by sintering simulations to obtain a deformation map. This map is used to generate a deformed FE model, which is updated iteratively until an error or convergence criteria is met. The RMS method is used to calculate the deviation between the target configuration and the current configuration in each iteration. The process continues until the error is minimized, indicating that the sintering deformations are compensated.

The experimental-based method to achieve higher dimensional accuracy involves a pre-deformation step based on experimental data, which are obtained from a numerical-based compensated geometry. This is done by manufacturing a numerically compensated model and scanning it to attain an as-sinter configuration labeled S_i'. The as-sinter configuration is aligned with the target geometry S_0 using a ray tracing approach to determine deviation vectors between S_i' and S_0. The accuracy of the compensation process is improved by using normalized displacement vectors from the last compensation iteration of numerical simulations instead of the normal unit vector of S_0. The resulting deviation vectors are then superimposed with reversed displacement vectors from the last iteration of the numerically compensated model and mapped onto the initial CAD geometry to prepare an experimentally-based compensated CAD model S_{i-exp}^{-1}.

By validating the methods, an IT14 grade was achieved for MBJ industrial components with the numerical-based method. The dimensional accuracy was increased through the experimental-based method, fulfilling the IT13 grade.

Chapter 8

Summary and outlook

8.1 Summary

The current research has presented physics-based data-driven numerical frameworks as a solution to the challenges encountered in the manufacturing process of intact and precise components using metal binder jetting technology. These challenges are addressed by accomplishing three primary objectives: prediction of debinding failure, developing numerical simulation of sintering deformation, and implementing compensation techniques to counteract sintering deformation.

For **failure prediction of debinding**, experimental analysis utilizing thermo-optical and TGA techniques has revealed that failures predominantly occur during debinding, even at temperatures lower than 400 °C, when the binder is removed. A DoE study involving 853 tensile and bending self-stressing specimens has identified stress and print direction as the crucial parameters contributing to crack formation and failures during the debinding process. A static numerical simulation has been employed to calculate stress values on the self-stressing specimens. The stress values, combined with recorded print direction and failure data from experiments, have been used to develop a Weibull distribution model to predict the failure likelihood in MBJ components.

Validation experiments performed on other self-stressing geometries and a manifold geometry have indicated that while the model tends to overestimate the failure probability of components, it effectively identifies regions prone to failure. The introduced model enables the exploration of components' manufacturability through rapid numerical simulations, eliminating the need for expensive trial-and-error experiments. This model can be utilized to redesign areas susceptible to failure or modify manufacturing parameters in order to mitigate adverse manufacturing issues.

To develop **numerical simulation of sintering deformation**, the SOVS model has been calibrated for MBJ with various experiments. The calibrated SOVS model demonstrates the capability to capture sintering deformation in MBJ. However, when applied in its conventional form, the model falls short of accurately predicting deformations within a 1 mm tolerance for industrial-sized geometries. Moreover, the model needs further development to tackle specific challenges encountered in MBJ, such as heterogeneous density distribution and dimensional accuracy of green parts, as well as anisotropic shrinkage behavior.

A computational framework combining physics-based principles with data-driven approaches has been developed to enhance the accuracy of calculations. A statistical model utilizing interpolation techniques based on previously printed parts has been introduced to predict the dimensions and density of green parts. Proved by validations, the statistical interpolation method outperformed conventional methods in accurately predicting the density and dimensions of green parts. Extensive experiments have been conducted to determine the anisotropic shrinkage behavior, sinter stress, and apparent viscosity of MBJ samples. These findings have been incorporated into the SOVS model, resulting in the development of a generic material model for calculating sintering deformations, effectively addressing the MBJ challenges.

By employing this physics-based data-driven model, the prediction accuracy of sintering deformations in MBJ has been significantly enhanced, achieving a tolerance of 0.5 mm.

Compensation techniques for sintering deformations have been presented by introducing a reversed deformation mapping algorithm. This algorithm employs an iterative approach to calculate and compensate for sintering deformations using the data-driven numerical model, continuing the process until a specified tolerance is attained. The compensated deformations have been then morphed into CAD models for printing. Experimental evidence from two industrial-related parts has demonstrated that the purely numerical-based compensations achieve an IT14 grade, meeting the dimensional accuracy requirements.

Although the proposed data-driven numerical model for sintering deformations demonstrates good accuracy, it does not consider all manufacturing parameters that can affect deformation behavior, such as PSD or powder revision. To address this, an experimental-based compensation method has been presented. This method measures deviation vectors between target and as-sinter configuration of numerically compensated geometries, maps them to previous numerical calculations, and compensates for sintering deformations. Using this method, a tighter IT grade of 13 has been achieved, thereby enabling MBJ to attain a higher technological readiness level.

8.2 Outlook

To further advance the understanding and optimization of MBJ manufacturing, future work could focus on several aspects. Firstly, the presented simulation-based Weibull model for predicting debinding failures should be further validated with experimental evidence. In addition, the effect of influencing factors such as temperature gradient, furnace vibrations, and relative movement of specimens with respect to the sintering set-up should be identified systematically. Deterministic numerical methods could be employed to study the failure likelihood during debinding, which can provide insights into understanding and optimizing the debinding process.

To improve the prediction accuracy of green part properties, numerical approaches that simulate the printing process, including the interaction of powder spreading and binder application, can be employed.

The limitations of the given data-driven numerical simulation approach for sintering deformations should be studied further to spot its application area. Different printing and sintering parameters should be used to evaluate the accuracy of the model. To develop more accurate material models, future work can focus on conducting more precise experiments to determine the viscosity and anisotropy behavior of MBJ powder skeletons using thermo-optical measurements. Moreover, considering other process parameters, such as powder distribution size in the material models, can increase the reliability of the simulations.

Bibliography

[1] I. Bahnini, M. Rivette, A. Rechia, A. Siadat, and A. Elmesbahi. "Additive manufacturing technology: The status, applications, and prospects". In: *The International Journal of Advanced Manufacturing Technology* 97.1-4 (2018), pp. 147–161. DOI: *10.1007/s00170-018-1932-y*.

[2] R. Lachmayer, R.B. Lippert, and S. Kaierle, eds. *Additive Serienfertigung*. Berlin, Heidelberg: Springer Berlin Heidelberg, 2018. ISBN: 978-3-662-56462-2. DOI: *10.1007/978-3-662-56463-9*.

[3] M. Zenou and L. Grainger. "3 - Additive manufacturing of metallic materials". In: *Additive Manufacturing*. Ed. by J. Zhang and Y.G. Jung. Butterworth-Heinemann, 2018, pp. 53–103. ISBN: 978-0-12-812155-9. DOI: *10.1016/B978-0-12-812155-9.00003-7*.

[4] L.J. Kumar, P.M. Pandey, and D.I. Wimpenny, eds. *3D Printing and Additive Manufacturing Technologies*. Singapore: Springer Singapore, 2019. ISBN: 978-981-13-0304-3. DOI: *10.1007/978-981-13-0305-0*.

[5] M. Salmi. "Additive Manufacturing Processes in Medical Applications". In: *Materials* 14.1 (2021). DOI: *10.3390/ma14010191*.

[6] R. Anderhofstadt and M. Disselkamp, eds. *Disruptiver 3D-Druck*. München: Carl Hanser Verlag GmbH & Co. KG, 2022. ISBN: 978-3-446-47020-0. DOI: *10.3139/9783446470217*.

[7] S. Salunkhe and D. Rajamani. "3 - Current trends of metal additive manufacturing in the defense, automobile, and aerospace industries". In: *Advances in Metal Additive Manufacturing*. Ed. by S. Salunkhe, S.T. Amancio-Filho, and J.P. Davim. Woodhead Publishing Reviews: Mechanical Engineering Series. Woodhead Publishing, 2023, pp. 147–160. ISBN: 978-0-323-91230-3. DOI: *10.1016/B978-0-323-91230-3.00004-4*.

[8] R.P.M. Guimarães et al. "1 - Powder bed fusion processes: Main classes of alloys, current status, and technological trends". In: *Advances in Metal Additive Manufacturing*. Ed. by S. Salunkhe, S.T. Amancio-Filho, and J.P. Davim. Woodhead Publishing Reviews: Mechanical Engineering Series. Woodhead Publishing, 2023, pp. 1–104. ISBN: 978-0-323-91230-3. DOI: *10.1016/B978-0-323-91230-3.00003-2*.

[9] S. Goehrke. *Additive Manufacturing Is Driving The Future Of The Automotive Industry*. 2018. URL: *https://www.forbes.com/sites/sarahgoehrke/2018/12/05/additive-manufacturing-is-driving-the-future-of-the-automotive-industry/?sh=72cb50cf75cc* (date accessed: 02/23/2023).

[10] M. Ziaee and N.B. Crane. "Binder jetting: A review of process, materials, and methods". In: *Additive Manufacturing* 28 (2019), pp. 781–801. DOI: *10.1016/j.addma.2019.05.031*.

[11] A. Mostafaei et al. “Binder jet 3D printing – process parameters, materials, properties, and challenges”. In: *Progress in Materials Science* (2020), p. 100707. DOI: *10.1016/j.pmatsci.2020.100707*.

[12] I. Gibson, D. Rosen, B. Stucker, and M. Khorasani. *Additive Manufacturing Technologies*. Cham: Springer International Publishing, 2021. ISBN: 978-3-030-56126-0. DOI: *10.1007/978-3-030-56127-7*.

[13] J.D. Reid. “Avoiding Cracks in the Production of PM Components”. In: *Metal Powder Report* 41.11 (1986), pp. 845–847.

[14] H. Tsuru and T. Nakagawa. “Studies on crack formation in P/M compacting”. In: *Advances in Powder Metallurgy & Particulate Materials–1992* 2 (1992), pp. 291–300.

[15] R.M. German. *Sintering theory and practice*. A Wiley interscience publication. New York: Wiley, 1996. ISBN: 978-0471057864.

[16] D.C. Zenger, H. Cai, J. McNeill, and R. Ludwig. “Classification Strategy to Identify and Classify Common Cracks in Green-State Powdered Metallurgy Compacts”. In: *Review of Progress in Quantitative Nondestructive Evaluation*. Ed. by D.O. Thompson and D.E. Chimenti. Boston, MA: Springer US, 1997, pp. 1443–1450. ISBN: 978-1-4613-7725-2. DOI: *10.1007/978-1-4615-5947-4_188*.

[17] D.C. Zenger and H. Cai. “Common causes of cracks in P/M compacts”. In: *International journal of powder metallurgy (1986)* 34.4 (1998), pp. 33–52.

[18] P. Chen, G. Kim, and J. Ni. “Investigations in the compaction and sintering of large ceramic parts”. In: *Journal of Materials Processing Technology* 190.1-3 (2007), pp. 243–250. DOI: *10.1016/j.jmatprotec.2007.02.039*.

[19] R.M. German. *Sintering: From Empirical Observations to Scientific Principles*. Elsevier Reference Monographs, 2014. ISBN: 978-0-12-401682-8. DOI: *10.1016/C2012-0-00717-X*.

[20] C.H. Hsueh, A.G. Evans, R.M. Cannon, and R.J. Brook. “Viscoelastic stresses and sintering damage in heterogeneous powder compacts”. In: *Acta Metallurgica* 34.5 (1986), pp. 927–936. DOI: *10.1016/0001-6160(86)90066-0*.

[21] E.A. Olevsky and R.M. German. “Effect of gravity on dimensional change during sintering—I. Shrinkage anisotropy”. In: *Acta Materialia* 48.5 (2000), pp. 1153–1166. DOI: *10.1016/S1359-6454(99)00368-7*.

[22] E.A. Olevsky, R.M. German, and A. Upadhyaya. “Effect of gravity on dimensional change during sintering—II. Shape distortion”. In: *Acta Materialia* 48.5 (2000), pp. 1167–1180. DOI: *10.1016/S1359-6454(99)00369-9*.

[23] Y. Bai, G. Wagner, and C.B. Williams. “Effect of Particle Size Distribution on Powder Packing and Sintering in Binder Jetting Additive Manufacturing of Metals”. In: *Journal of Manufacturing Science and Engineering* 139.8 (2017), p. 081019. DOI: *10.1115/1.4036640*.

[24] A. Kumar, Y. Bai, A. Eklund, and C.B. Williams. “Effects of Hot Isostatic Pressing on Copper Parts Fabricated via Binder Jetting”. In: *Procedia Manufacturing* 10 (2017), pp. 935–944. DOI: *10.1016/j.promfg.2017.07.084*.

[25] M. Ziaee, E.M. Tridas, and N.B. Crane. “Binder-Jet Printing of Fine Stainless Steel Powder with Varied Final Density”. In: *JOM* 69.3 (2017), pp. 592–596. DOI: *10.1007/s11837-016-2177-6*.

[26] A. Lores, N. Azurmendi, I. Agote, and E. Zuza. “A review on recent developments in binder jetting metal additive manufacturing: Materials and process characteristics”. In: *Powder Metallurgy* 62.5 (2019), pp. 267–296. DOI: *10.1080/00325899.2019.1669299*.

[27] C. Meier, R. Weissbach, J. Weinberg, W.A. Wall, and A.J. Hart. "Critical influences of particle size and adhesion on the powder layer uniformity in metal additive manufacturing". In: *Journal of Materials Processing Technology* 266 (2019), pp. 484–501. DOI: *10.1016/j.jmatprotec.2018.10.037*.

[28] S. Sadeghi Borujeni, G.S. Saluja, and V. Ploshikhin. "Compensation of sintering deformation for components manufactured by metal binder jetting using numerical simulations". In: *Rapid Prototyping Journal* 29.3 (2023), pp. 612–625. DOI: *10.1108/RPJ-06-2022-0181*.

[29] S. Meteyer, X. Xu, N. Perry, and Y.F. Zhao. "Energy and Material Flow Analysis of Binder-jetting Additive Manufacturing Processes". In: *Procedia CIRP* 15.9 (2014), pp. 19–25. DOI: *10.1016/j.procir.2014.06.030*.

[30] S.M. Gaytan et al. "Fabrication of barium titanate by binder jetting additive manufacturing technology". In: *Ceramics International* 41.5 (2015), pp. 6610–6619. DOI: *10.1016/j.ceramint.2015.01.108*.

[31] A. Gebhardt. *Additive Fertigungsverfahren: Additive Manufacturing und 3D-Drucken für Prototyping - Tooling - Produktion*. 5., neu bearbeitete und erweiterte Auflage. München: Hanser, 2016. ISBN: 978-3-446-44401-0.

[32] T. Dahmen, C.G. Klingaa, S. Baier-Stegmaier, A. Lapina, D.B. Pedersen, and J.H. Hattel. "Characterization of channels made by Laser Powder Bed Fusion and Binder Jetting using X-ray CT and image analysis". In: *Additive Manufacturing* (2020), p. 101445. DOI: *10.1016/j.addma.2020.101445*.

[33] S. Bafaluy Ojea, J. Torrents-Barrena, M.T. Pérez-Prado, R. Muñoz Moreno, and F. Sket. "Binder jet green parts microstructure: Advanced quantitative analysis". In: *Journal of Materials Research and Technology* 23.1 (2023), pp. 3974–3986. DOI: *10.1016/j.jmrt.2023.02.051*.

[34] HP Inc. *HP Metal Jet technology: HP's digital printing technology for metals. Technical white paper*. 2023. URL: *https://h20195.www2.hp.com/v2/GetDocument.aspx?docname=4AA7-3333ENW* (date accessed: 05/04/2023).

[35] N. Kurgan. "Effect of porosity and density on the mechanical and microstructural properties of sintered 316L stainless steel implant materials". In: *Materials & Design* 55 (2014), pp. 235–241. DOI: *10.1016/j.matdes.2013.09.058*.

[36] T. Do, P. Kwon, and C.S. Shin. "Process development toward full-density stainless steel parts with binder jetting printing". In: *International Journal of Machine Tools and Manufacture* 121.2 (2017), pp. 50–60. DOI: *10.1016/j.ijmachtools.2017.04.006*.

[37] S. Mirzababaei and S. Pasebani. "A Review on Binder Jet Additive Manufacturing of 316L Stainless Steel". In: *Journal of Manufacturing and Materials Processing* 3.3 (2019). DOI: *10.3390/jmmp3030082*.

[38] N. Lecis et al. "Effects of process parameters, debinding and sintering on the microstructure of 316L stainless steel produced by binder jetting". In: *Materials Science and Engineering: A* 828.10 (2021), p. 142108. DOI: *10.1016/j.msea.2021.142108*.

[39] Y. Mao, J. Li, W. Li, D. Cai, and Q. Wei. "Binder jetting additive manufacturing of 316L stainless-steel green parts with high strength and low binder content: Binder preparation and process optimization". In: *Journal of Materials Processing Technology* 291 (2021), p. 117020. DOI: *10.1016/j.jmatprotec.2020.117020*.

[40] A. Cabo Rios, E. Hryha, E.A. Olevsky, and P. Harlin. "Sintering anisotropy of binder jetted 316L stainless steel: Part I – sintering anisotropy". In: *Powder Metallurgy* 65.4 (2022), pp. 273–282. DOI: *10.1080/00325899.2021.2020485*.

[41] W. Chen, Z. Chen, L. Chen, D. Zhu, and Z. Fu. "Optimization of Printing Parameters to Achieve High-Density 316L Stainless Steel Manufactured by Binder Jet 3D Printing". In: *Journal of Materials Engineering and Performance* 39 (2022), p. 201. DOI: *10.1007/s11665-022-07368-1*.

[42] A.L. Rütjes. "Untersuchung zur Herstellbarkeit von Binder Jetting-Bauteilverbunden mittels Sinterfügen". Doctoral thesis. Bremen: University of Bremen, 2022. DOI: *10.26092/elib/1963*.

[43] A. Simchi, F. Petzoldt, T. Hartwig, S.B. Hein, B. Barthel, and L. Reineke. "Binder Jet 3d Printing of Biomedical Grade Ti-6al-4v Alloy: The Role of Particle Size, Microstructural Features, and Mechanical Properties". In: *SSRN Electronic Journal* 59 (2022), p. 193. DOI: *10.2139/ssrn.4127679*.

[44] B. Utela, D. Storti, R. Anderson, and M. Ganter. "A review of process development steps for new material systems in three dimensional printing (3DP)". In: *Journal of Manufacturing Processes* 10.2 (2008), pp. 96–104. DOI: *10.1016/j.jmapro.2009.03.002*.

[45] R.K. Enneti, S.J. Park, R.M. German, and S.V. Atre. "Review: Thermal Debinding Process in Particulate Materials Processing". In: *Materials and Manufacturing Processes* 27.2 (2012), pp. 103–118. DOI: *10.1080/10426914.2011.560233*.

[46] I. Rishmawi, M. Salarian, and M. Vlasea. "Tailoring green and sintered density of pure iron parts using binder jetting additive manufacturing". In: *Additive Manufacturing* 24 (2018), pp. 508–520. DOI: *10.1016/j.addma.2018.10.015*.

[47] B. Verlee, T. Dormal, and J. Lecomte-Beckers. "Density and porosity control of sintered 316L stainless steel parts produced by additive manufacturing". In: *Powder Metallurgy* 55.4 (2013), pp. 260–267. DOI: *10.1179/0032589912Z.00000000082*.

[48] Y. Wang and Y.F. Zhao. "Investigation of sintering shrinkage in binder jetting additive manufacturing process". In: *Procedia Manufacturing* 10 (2017), pp. 779–790. DOI: *10.1016/j.promfg.2017.07.077*.

[49] P. Beiss, ed. *Pulvermetallurgische Fertigungstechnik: Kapitel 5: Sintern*. Berlin u.a.: Springer Vieweg, 2013. ISBN: 978-3-642-32031-6. DOI: *10.1007/978-3-642-32032-3*.

[50] A. Mostafaei, E.L. Stevens, E.T. Hughes, S.D. Biery, C. Hilla, and M. Chmielus. "Powder bed binder jet printed alloy 625: Densification, microstructure and mechanical properties". In: *Materials & Design* 108 (2016), pp. 126–135. DOI: *10.1016/j.matdes.2016.06.067*.

[51] O. Andersen et al. "Neue Entwicklungen auf dem Gebiet der nicht-strahlbasierten additiven Fertigungsverfahren - New Developments in the Field of Non-beam Based Methods of Additive Manufacturing". In: *Pulvermetallurgie - neue Herausforderungen und neue Wege*. Ed. by H. Danninger, L. Sigl, and C. Broeckmann. Pulvermetallurgie in Wissenschaft und Praxis. Rheine: Heimdall Verlag, 2018. ISBN: 978-3-946537-54-0.

[52] K. Miyake, Y. Hirata, T. Shimonosono, and S. Sameshima. "The Effect of Particle Shape on Sintering Behavior and Compressive Strength of Porous Alumina". In: *Materials* 11.7 (2018). DOI: *10.3390/ma11071137*.

[53] A. Mostafaei, P. Rodriguez De Vecchis, I. Nettleship, and M. Chmielus. "Effect of powder size distribution on densification and microstructural evolution of binder-jet 3D-printed

alloy 625". In: *Materials & Design* 162 (2019), pp. 375–383. DOI: *10.1016/j.matdes.2018.11.051*.

[54] B. Barthel, F.J. Janas, and S. Wieland. "Powder condition and spreading parameter impact on green and sintered density in metal binder jetting". In: *Powder Metallurgy* 64.5 (2021), pp. 378–386. DOI: *10.1080/00325899.2021.1912923*.

[55] D. Huber, L. Vogel, and A. Fischer. "The Effects of Sintering Temperature and Hold Time on Densification, Mechanical Properties and Microstructural Characteristics of Binder Jet 3D Printed 17-4 PH Stainless Steel". In: *Additive Manufacturing* (2021), p. 102114. DOI: *10.1016/j.addma.2021.102114*.

[56] P. Schwed. "Surface Diffusion in Sintering of Spheres on Planes". In: *JOM* 3.3 (1951), pp. 245–246. DOI: *10.1007/BF03397302*.

[57] W. Schatt, K.P. Wieters, and B. Kieback. *Pulvermetallurgie: Technologien und Werkstoffe*. 1. Aufl. VDI-Buch. s.l.: Springer-Verlag, 2007. ISBN: 978-3-540-68112-0.

[58] H. Djohari, J.I. Martínez-Herrera, and J.J. Derby. "Transport mechanisms and densification during sintering: I. Viscous flow versus vacancy diffusion". In: *Chemical Engineering Science* 64.17 (2009), pp. 3799–3809. DOI: *10.1016/j.ces.2009.05.018*.

[59] R.M. German. "1 - Thermodynamics of sintering". In: *Sintering of Advanced Materials*. Ed. by Z.Z. Fang. Woodhead Publishing Series in Metals and Surface Engineering. Woodhead Publishing, 2010, pp. 3–32. ISBN: 978-1-84569-562-0. DOI: *10.1533/9781845699949.1.3*.

[60] F. Thümmler and W. Thomma. "The sintering process". In: *Metallurgical Reviews* 12.1 (1967), pp. 69–108.

[61] M.F. Ashby. "A first report on sintering diagrams". In: *Acta Metallurgica* 22.3 (1974), pp. 275–289. DOI: *10.1016/0001-6160(74)90167-9*.

[62] M.N. Rahaman. *Sintering of Ceramics*. CRC Press, 2007. ISBN: 9780429128424. DOI: *10.1201/b15869*.

[63] R.M. German. "Chapter Seven - Thermodynamic and Kinetic Treatments". In: *Sintering: from Empirical Observations to Scientific Principles*. Ed. by R.M. German. Boston: Butterworth-Heinemann, 2014, pp. 183–226. ISBN: 978-0-12-401682-8. DOI: *10.1016/B978-0-12-401682-8.00007-0*.

[64] B.P. Kashyap and K. Tangri. "Grain growth behaviour of type 316L stainless steel". In: *Materials Science and Engineering: A* 149.2 (1992), pp. L13–L16. DOI: *10.1016/0921-5093(92)90392-E*.

[65] C.E. Krill et al. "Size-dependent grain-growth kinetics observed in nanocrystalline Fe". In: *Physical review letters* 86.5 (2001), pp. 842–845. DOI: *10.1103/PhysRevLett.86.842*.

[66] R.P. Koseski, P. Suri, N.B. Earhardt, R.M. German, and Y.S. Kwon. "Microstructural evolution of injection molded gas- and water-atomized 316L stainless steel powder during sintering". In: *Materials Science and Engineering: A* 390.1-2 (2005), pp. 171–177. DOI: *10.1016/j.msea.2004.08.002*.

[67] M.N. Rahaman. "2 - Kinetics and mechanisms of densification". In: *Sintering of Advanced Materials*. Ed. by Z.Z. Fang. Woodhead Publishing Series in Metals and Surface Engineering. Woodhead Publishing, 2010, pp. 33–64. ISBN: 978-1-84569-562-0. DOI: *10.1533/9781845699949.1.33*.

[68] R.M. German. "Chapter Eight - Microstructure Coarsening". In: *Sintering: from Empirical Observations to Scientific Principles*. Ed. by R.M. German. Boston: Butterworth-

Heinemann, 2014, pp. 227–246. ISBN: 978-0-12-401682-8. DOI: *10.1016/B978-0-12-401682-8.00008-2*.

[69] J.P. Choi, G.Y. Lee, J.I. Song, W.S. Lee, and J.S. Lee. "Sintering behavior of 316L stainless steel micro–nanopowder compact fabricated by powder injection molding". In: *Powder Technology* 279 (2015), pp. 196–202. DOI: *10.1016/j.powtec.2015.04.014*.

[70] B. Paredes-Goyes, Da. Jauffres, J.M. Missiaen, and C.L. Martin. "Grain growth in sintering: A discrete element model on large packings". In: *Acta Materialia* 218.5 (2021), p. 117182. DOI: *10.1016/j.actamat.2021.117182*.

[71] R.L. Coble. "Sintering Crystalline Solids. I. Intermediate and Final State Diffusion Models". In: *Journal of Applied Physics* 32.5 (1961), pp. 787–792. DOI: *10.1063/1.1736107*.

[72] C.F. YEN and R.L. Coble. "Spheroidization of Tubular Voids in Al2 O3 Crystals at High Temperatures". In: *Journal of the American Ceramic Society* 55.10 (1972), pp. 507–509. DOI: *10.1111/j.1151-2916.1972.tb13417.x*.

[73] H. Tanaka, A. Yamamoto, J Shimoyama, H. Ogino, and K. Kishio. "Strongly connected ex situ MgB 2 polycrystalline bulks fabricated by solid-state self-sintering". In: *Superconductor Science and Technology* 25.11 (2012), p. 115022. DOI: *10.1088/0953-2048/25/11/115022*.

[74] P. Jonsén. "Fracture and stress in powder compacts". PhD thesis. SE-97187 Luleå, Sweden: Luleå tekniska universitet, 2006.

[75] R. Sachanandani and S. Lombardo. "Effect of Green Body Size and Heating Rate on Failure During Thermal Debinding and on Debinding Cycle Time". In: *Journal of Ceramic Processing Research* 12 (2011), pp. 115–121.

[76] C. Kukla, S. Cano, D. Kaylani, S. Schuschnigg, C. Holzer, and J. Gonzalez-Gutierrez. "Debinding behaviour of feedstock for material extrusion additive manufacturing of zirconia". In: *Powder Metallurgy* 62.3 (2019), pp. 196–204. DOI: *10.1080/00325899.2019.1616139*.

[77] A. Tatarinov, V. Kurtenoks, and V. Mironovs. "Detection of cracks in green products of powder metallurgy by means of laser vibrometry". In: *IOP Conference Series: Materials Science and Engineering* 1140.1 (2021), p. 012045. DOI: *10.1088/1757-899X/1140/1/012045*.

[78] Z. Lotfizarei, A. Mostafapour, A. Barari, A. Jalili, and A.E. Patterson. "Overview of debinding methods for parts manufactured using powder material extrusion". In: *Additive Manufacturing* 61.1 (2023), p. 103335. DOI: *10.1016/j.addma.2022.103335*.

[79] B.W. Kabore and B. Peters. "Micromechanical model for sintering and damage in viscoelastic porous ice and snow. Part I: Model and calibration". In: *International Journal of Solids and Structures* 185-186.43 (2020), pp. 324–333. DOI: *10.1016/j.ijsolstr.2019.08.038*.

[80] B.W. Kabore and B. Peters. "Micromechanical model for sintering and damage in viscoelastic porous ice and snow. Part II: Validation". In: *International Journal of Solids and Structures* 185-186.43 (2020), pp. 281–291. DOI: *10.1016/j.ijsolstr.2019.08.036*.

[81] J. Jeong, H. Adib-Ramezani, and G.A. Pluvinage. "Tensile strength of the brittle materials, probabilistic or deterministic approach?" In: *Strength of Materials* 38.1 (2006), pp. 72–83. DOI: *10.1007/s11223-006-0018-5*.

[82] G.Z. Voyiadjis. *Handbook of Damage Mechanics*. New York, NY: Springer New York, 2015. ISBN: 978-1-4614-5588-2. DOI: *10.1007/978-1-4614-5589-9*.

[83] BASF. *Debinding Simulation Guidelines for 3D Printed Parts using Ultrafuse® 316L*. BASF, 2021. URL: *https://forward-am.com/wp-content/uploads/2021/01/Debinding-and-Simulation-Guidelines.pdf* (date accessed: 12/05/2022).

[84] T. Rosnitschek, J. Glamsch, C. Lange, B. Alber-Laukant, and F. Rieg. "An Automated Open-Source Approach for Debinding Simulation in Metal Extrusion Additive Manufacturing". In: *Designs* 5.1 (2021), p. 2. DOI: *10.3390/designs5010002*.

[85] C. Lu, R. Danzer, and F.D. Fischer. "Influence of Threshold Stress on the Estimation of the Weibull Statistics". In: *Journal of the American Ceramic Society* 85.6 (2002), pp. 1640–1642. DOI: *10.1111/j.1151-2916.2002.tb00330.x*.

[86] O.M. Jadaan, N.N. Nemeth, J. Bagdahn, and W.N. Sharpe. "Probabilistic Weibull Behavior and Mechanical Properties of MEMS Brittle Materials". In: *Journal of Materials Science* 38.20 (2003), pp. 4087–4113. DOI: *10.1023/A:1026317303377*.

[87] W. Weibull. "A Statistical Distribution Function of Wide Applicability". In: *Journal of Applied Mechanics* 18.3 (1951), pp. 293–297. DOI: *10.1115/1.4010337*.

[88] W. Weibull. "The phenomenon of rupture in solids". In: 1939.

[89] A.C. Rufin, D.R. Samos, and R.J.H. Bollard. "Statistical Failure Prediction Models for Brittle Materials". In: *AIAA Journal* 22.1 (1984), pp. 135–140. DOI: *10.2514/3.48426*.

[90] F.W. Zok. "On weakest link theory and Weibull statistics". In: *Journal of the American Ceramic Society* 100.4 (2017), pp. 1265–1268. DOI: *10.1111/jace.14665*.

[91] J. Margetson. "Failure Probability Evaluation of an Anisotropic Brittle Structure Derived from a Thermal Stress Solution". In: *Thermal Stresses in Severe Environments*. Ed. by D.P.H. Hasselman and R.A. Heller. Boston, MA: Springer US, 1980, pp. 503–519. ISBN: 978-1-4613-3156-8. DOI: *10.1007/978-1-4613-3156-8_32*.

[92] R. Danzer, T. Lube, P. Supancic, and R. Damani. "Fracture of Ceramics". In: *Advanced Engineering Materials* 10.4 (2008), pp. 275–298. DOI: *10.1002/adem.200700347*.

[93] F. Yang, H. Ren, and Z. Hu. "Maximum Likelihood Estimation for Three-Parameter Weibull Distribution Using Evolutionary Strategy". In: *Mathematical Problems in Engineering* 2019 (2019), pp. 1–8. DOI: *10.1155/2019/6281781*.

[94] M. Zago, N.F. Maria Lecis, M. Vedani, and I. Cristofolini. "Dimensional and geometrical precision of parts produced by binder jetting process as affected by the anisotropic shrinkage on sintering". In: *Additive Manufacturing* 43 (2021), p. 102007. DOI: *10.1016/j.addma.2021.102007*.

[95] J. Marczyk, K. Ostrowska, and M. Hebda. "Influence of binder jet 3D printing process parameters from irregular feedstock powder on final properties of Al parts". In: *Advanced Powder Technology* 33.11 (2022), p. 103768. DOI: *10.1016/j.apt.2022.103768*.

[96] Z. Chen, W. Chen, L. Chen, D. Zhu, Q. Chen, and Z. Fu. "Influence of initial relative densities on the sintering behavior and mechanical behavior of 316 L stainless steel fabricated by binder jet 3D printing". In: *Materials Today Communications* 31 (2022), p. 103369. DOI: *10.1016/j.mtcomm.2022.103369*.

[97] S.E. Schoenberg, D.J. Green, A.E. Segall, G.L. Messing, A.S. Grader, and P.M. Halleck. "Stresses and Distortion Due to Green Density Gradients During Densification". In: *Journal of the American Ceramic Society* 89.10 (2006), pp. 3027–3033. DOI: *10.1111/j.1551-2916.2006.01182.x*.

[98] G. Gagg, E. Ghassemieh, and F.E. Wiria. "Effects of sintering temperature on morphology and mechanical characteristics of 3D printed porous titanium used as dental implant".

In: *Materials science & engineering. C, Materials for biological applications* 33.7 (2013), pp. 3858–3864. DOI: *10.1016/j.msec.2013.05.021*.

[99] E. Torresani et al. "Anisotropy of Mass Transfer During Sintering of Powder Materials with Pore–Particle Structure Orientation". In: *Metallurgical and Materials Transactions A* 50.2 (2019), pp. 1033–1049. DOI: *10.1007/s11661-018-5037-x*.

[100] D.L. Bourell, W. Frazier, H. Kuhn, and M. Seifi, eds. *Additive Manufacturing Processes*. ASM International, 2020. DOI: *10.31399/asm.hb.v24.9781627082907*.

[101] E. Torresani, R.M. German, R. Huff, and E.A. Olevsky. "Influence of gravity on sintering of 3D–printed powder components". In: *Journal of the American Ceramic Society* 105.1 (2022), pp. 131–146. DOI: *10.1111/jace.18056*.

[102] T. Kraft and H. Riedel. "Numerical simulation of solid state sintering; model and application". In: *Journal of the European Ceramic Society* 24.2 (2004), pp. 345–361. DOI: *10.1016/S0955-2219(03)00222-X*.

[103] J. Song, J.C. Gelin, T. Barrière, and B. Liu. "Experiments and numerical modelling of solid state sintering for 316L stainless steel components". In: *Journal of materials processing technology* 177.1-3 (2006), pp. 352–355. DOI: *10.1016/j.jmatprotec.2006.04.111*.

[104] S. Kiani, J. Pan, J.A. Yeomans, M. Barriere, and P. Blanchart. "Finite element analysis of sintering deformation using densification data instead of a constitutive law". In: *Journal of the European Ceramic Society* 27.6 (2007), pp. 2377–2383. DOI: *10.1016/j.jeurceramsoc.2006.08.019*.

[105] D.U. Furrer and S.L. Semiatin. *Metals process simulation*. Vol. prepared under the direction of the ASM International Handbook Committee ; Vol. 22B. ASM handbook. Materials Park, Ohio: ASM International, 2010. ISBN: 978-1-61503-005-7.

[106] J. Song, T. Barriere, B. Liu, J.C. Gelin, and G. Michel. "Experimental and numerical analysis on sintering behaviours of injection moulded components in 316L stainless steel powder". In: *Powder Metallurgy* 53.4 (2010), pp. 295–304. DOI: *10.1179/003258908X334212*.

[107] I.U. Mohsin, D. Lager, W. Hohenauer, C. Gierl, and H. Danninger. "Finite element sintering analysis of metal injection molded copper brown body using thermo-physical data and kinetics". In: *Computational Materials Science* 53.1 (2012), pp. 6–11. DOI: *10.1016/j.commatsci.2011.08.028*.

[108] H. Xin, W. Sun, and J. Fish. "Discrete element simulations of powder-bed sintering-based additive manufacturing". In: *International Journal of Mechanical Sciences* 149 (2018), pp. 373–392. DOI: *10.1016/j.ijmecsci.2017.11.028*.

[109] Z. Chen, F. Li, W. Chen, D. Zhu, and Z. Fu. "Numerical Simulation of Particle Size Influence on the Sintering Behavior of 316L Stainless Steel Powders Fabricated by Binder Jet 3D Printing". In: *Journal of Materials Engineering and Performance* 30.5 (2021), pp. 3705–3717. DOI: *10.1007/s11665-021-05709-0*.

[110] E.A. Olevsky. "Theory of sintering: from discrete to continuum". In: *Materials Science and Engineering: R: Reports* 23.2 (1998), pp. 41–100. DOI: *10.1016/S0927-796X(98)00009-6*.

[111] M. Braginsky, V. Tikare, and E.A. Olevsky. "Numerical simulation of solid state sintering". In: *International Journal of Solids and Structures* 42.2 (2005), pp. 621–636. DOI: *10.1016/j.ijsolstr.2004.06.022*.

[112] E.A. Olevsky, V. Tikare, and T. Garino. "Multi-Scale Study of Sintering: A Review". In: *Journal of the American Ceramic Society* 89.6 (2006), pp. 1914–1922. DOI: *10.1111/j.1551-2916.2006.01054.x*.

[113] V. Tikare, M.V. Braginsky, D. Bouvard, and A. Vagnon. "An Experimental Validation of a 3D Kinetic, Monte Carlo Model for Microstructural Evolution during Sintering". In: Advances in Science and Technology. Trans Tech Publications LtdSwitzerland, 2006, pp. 522–529. DOI: *10.4028/www.scientific.net/AST.45.522*.

[114] F. Wakai. "Modeling and Simulation of Elementary Processes in Ideal Sintering". In: *Journal of the American Ceramic Society* 89.5 (2006), pp. 1471–1484. DOI: *10.1111/J.1551-2916.2006.01001.X*.

[115] M.W. Reiterer and K.G. Ewsuk. "An Analysis of Four Different Approaches to Predict and Control Sintering". In: *Journal of the American Ceramic Society* 92.7 (2009), pp. 1419–1427. DOI: *10.1111/j.1551-2916.2009.03009.x*.

[116] V. Tikare, M. Braginsky, D. Bouvard, and A. Vagnon. "Numerical simulation of microstructural evolution during sintering at the mesoscale in a 3D powder compact". In: *Computational Materials Science* 48.2 (2010), pp. 317–325. DOI: *10.1016/j.commatsci.2010.01.013*.

[117] F. Wakai and K.A. Brakke. "Mechanics of sintering for coupled grain boundary and surface diffusion". In: *Acta Materialia* 59.14 (2011), pp. 5379–5387. DOI: *10.1016/j.actamat.2011.05.006*.

[118] J. Pan. "Modelling sintering at different length scales". In: *International Materials Reviews* 48.2 (2013), pp. 69–85. DOI: *10.1179/095066002225010209*.

[119] Y. Liu et al. "Monte Carlo simulation of polycrystalline microstructures and finite element stress analysis". In: *Materials & Design* 55 (2014), pp. 740–746. DOI: *10.1016/j.matdes.2013.10.047*.

[120] R. Bjørk, H.L. Frandsen, N. Pryds, and E.A. Olevsky. "Modeling the Microstructural Evolution During Constrained Sintering". In: *Journal of the American Ceramic Society* 98.11 (2015), pp. 3490–3495. DOI: *10.1111/jace.13701*.

[121] S. Hara, A. Ohi, and N. Shikazono. "Sintering analysis of sub-micron-sized nickel powders: Kinetic Monte Carlo simulation verified by FIB–SEM reconstruction". In: *Journal of Power Sources* 276 (2015), pp. 105–112. DOI: *10.1016/j.jpowsour.2014.11.110*.

[122] T. Gu, M. Gu, H. Du, and B. Zhao. "Simulation of microstructure evolution and prediction of mechanical properties of material of alumina ceramic cutting tools". In: *2017 IEEE International Conference on Mechatronics and Automation (ICMA)*. 2017, pp. 270–274. DOI: *10.1109/ICMA.2017.8015826*.

[123] J. Rojek, S. Nosewicz, M. Maździarz, P. Kowalczyk, K. Wawrzyk, and D. Lumelskyj. "Modeling of a Sintering Process at Various Scales". In: *Procedia Engineering* 177 (2017), pp. 263–270. DOI: *10.1016/j.proeng.2017.02.210*.

[124] S. Nosewicz, J. Rojek, K. Wawrzyk, P. Kowalczyk, G. Maciejewski, and M. Maździarz. "Multiscale modeling of pressure-assisted sintering". In: *Computational Materials Science* 156 (2019), pp. 385–395. DOI: *10.1016/j.commatsci.2018.10.001*.

[125] T. Kraft, H. Riedel, P. Stingl, and F. Witting. "Finite element simulation of die pressing and sintering". In: *Advanced Engineering Materials* 1.2 (1999), p. 107. DOI: *10.1002/(SICI)1527-2648(199910)1:2<107::AID-ADEM107>3.0.CO;2-E*.

[126] M. Gasik and B. Zhang. "A constitutive model and FE simulation for the sintering process of powder compacts". In: *Computational Materials Science* 18.1 (2000), pp. 93–101. DOI: *10.1016/S0927-0256(00)00090-2*.

[127] S. Bordère. "Original Monte Carlo Methodology Devoted to the Study of Sintering Processes". In: *Journal of the American Ceramic Society* 85.7 (2002), pp. 1845–1852. DOI: *10.1111/J.1151-2916.2002.TB00363.X*.

[128] J.Z. Pan and R.Y. Huang. "Multi-Scale Modelling of Sintering". In: *Key Engineering Materials* 368-372 (2008), pp. 1668–1672. DOI: *10.4028/www.scientific.net/KEM.368-372.1668*.

[129] T.T. Molla, R. Bjørk, E.A. Olevsky, N. Pryds, and H.L. Frandsen. "Multi-scale modeling of shape distortions during sintering of bi-layers". In: *Computational Materials Science* 88.8 (2014), pp. 28–36. DOI: *10.1016/j.commatsci.2014.02.041*.

[130] F. Raether and G. Seifert. "Modeling Inherently Homogeneous Sintering Processes". In: *Advanced Theory and Simulations* 1.5 (2018), p. 1800022. DOI: *10.1002/adts.201800022*.

[131] Y. Zhang, X. Xiao, and J. Zhang. "Kinetic Monte Carlo simulation of sintering behavior of additively manufactured stainless steel powder particles using reconstructed microstructures from synchrotron X-ray microtomography". In: *Results in Physics* 13 (2019), p. 102336. DOI: *10.1016/j.rinp.2019.102336*.

[132] E. Stevens, S. Schloder, E. Bono, D. Schmidt, and M. Chmielus. "Density variation in binder jetting 3D-printed and sintered Ti-6Al-4V". In: *Additive Manufacturing* 22 (2018), pp. 746–752. DOI: *10.1016/j.addma.2018.06.017*.

[133] P. Koehnen, ed. *Metal Binder Jetting in der Serienfertigung: Potentiale und Herausforderungen*. 2022.

[134] E.J.R. Parteli. "DEM simulation of particles of complex shapes using the multisphere method: Application for additive manufacturing". In: *AIP Conference Proceedings* 1542.1 (2013), pp. 185–188. DOI: *10.1063/1.4811898*.

[135] S. Haeri, Y. Wang, O.R. Ghita, and J. Sun. "Discrete element simulation and experimental study of powder spreading process in additive manufacturing". In: *Powder Technology* 306 (2017), pp. 45–54. DOI: *10.1016/j.powtec.2016.11.002*.

[136] G. Miao, W. Du, Z. Pei, and C. Ma. "Binder jetting additive manufacturing of ceramics: analytical and numerical models for powder spreading process". In: *ASME 2019 14th International Manufacturing Science and Engineering Conference*. American Society of Mechanical Engineers Digital Collection. 2019.

[137] J. Gan and A. Yu. "DEM simulation of the packing of cylindrical particles". In: *Granular Matter* 22.1 (2020), p. 5852. DOI: *10.1007/s10035-019-0993-4*.

[138] A.L. Maximenko, I.D. Olumor, A.P. Maidaniuk, and E.A. Olevsky. "Modeling of effect of powder spreading on green body dimensional accuracy in additive manufacturing by binder jetting". In: *Powder Technology* 385 (2021), pp. 60–68. DOI: *10.1016/j.powtec.2021.02.070*.

[139] J.J. Wagner and C. Fred Higgs , III. "Computation of Hydrodynamic and Capillary Phenomena in Binder Jet Three-Dimensional Printing". In: *Journal of Tribology* 143.5 (May 2021). DOI: *10.1115/1.4050942*.

[140] Y. Lee, P. Nandwana, and S. Simunovic. "Powder spreading, densification, and part deformation in binder jetting additive manufacturing". In: *Progress in Additive Manufacturing* 7.1 (2022), pp. 111–125. DOI: *10.1007/s40964-021-00214-1*.

[141] M. Abouaf, J.L. Chenot, G. Raisson, and P. Bauduin. "Finite element simulation of hot isostatic pressing of metal powders". In: *International Journal for Numerical Methods in Engineering* 25.1 (1988), pp. 191–212. DOI: *10.1002/nme.1620250116*.

[142] V.V. Skorokhod, E.A. Olevsky., and M.B. Shtern. "Continuum theory of sintering. I. Phenomenological model. Analysis of the effect of external forces on the kinetics of sintering". In: *Powder Metallurgy and Metal Ceramics* 32.1 (1993), pp. 21–26. DOI: *10.1007/BF00559728*.

[143] G.H. Paulino and Z.H. Jin. "Correspondence Principle in Viscoelastic Functionally Graded Materials". In: *Journal of Applied Mechanics* 68.1 (2001), pp. 129–132. DOI: *10.1115/1.1331286*.

[144] R. Zhang, R.S. Engel, N.J. Salamon, and R.M. German. "Finite element analysis on the sintering of stainless steel 316L powder compacts". In: *Advances in powder metallurgy and particulate materials* 9 (2002), pp. 9–60. URL: *http://www.cavs.msstate.edu/publications/docs/2002/07/2002-26.pdf* (date accessed: 07/04/2023).

[145] H. Riedel and B. Blug, eds. *A Comprehensive Model for Solid State Sintering and Its Application to Silicon Carbide: In: Chuang, T.J., Rudnicki, J.W. (eds). Multiscale Deformation and Fracture in Materials and Structures: The James R. Rice 60th Anniversary Volume*. Dordrecht: Springer Netherlands, 2002. ISBN: 978-0-306-46952-7. DOI: *10.1007/0-306-46952-9_4*.

[146] T.T. Molla. "Modeling Macroscopic Shape Distortions during Sintering of Multi-layers". PhD thesis. 2014.

[147] C. Quinard, T. Barriere, and J.C. Gelin. "Development and property identification of 316L stainless steel feedstock for PIM and µPIM". In: *Powder Technology* 190.1-2 (2009), pp. 123–128. DOI: *10.1016/j.powtec.2008.04.044*.

[148] M. Sahli, A. Lebied, J.C. Gelin, T. Barrière, and B. Necib. "Numerical simulation and experimental analysis of solid-state sintering response of 316 L stainless steel micro-parts manufactured by metal injection molding". In: *The International Journal of Advanced Manufacturing Technology* 79.9-12 (2015), pp. 2079–2092. DOI: *10.1007/s00170-015-6983-8*.

[149] Z.Y. Liu, N.H. Loh, K.A. Khor, and S.B. Tor. "Sintering activation energy of powder injection molded 316L stainless steel". In: *Scripta Materialia* 44.7 (2001), pp. 1131–1137. DOI: *10.1016/S1359-6462(01)00664-9*.

[150] H. Riedel. "A constitutive model for the finite-element simulation of sintering–Distortions and stresses". In: *Ceramic powder science III* (1990), pp. 619–630.

[151] J.D. Hansen, R.P. Rusin, M.H. Teng, and D.L. Johnson. "Combined-Stage Sintering Model". In: *Journal of the American Ceramic Society* 75.5 (1992), pp. 1129–1135. DOI: *10.1111/j.1151-2916.1992.tb05549.x*.

[152] J. Song. "Experiments, modelling and numerical simulation of the sintering process for metallic or ceramic powders". PhD thesis. Besançon, 2007.

[153] F. Wakai, Y. Shinoda, and T. Akatsu. "Methods to calculate sintering stress of porous materials in equilibrium". In: *Acta Materialia* 52.19 (2004), pp. 5621–5631. DOI: *10.1016/j.actamat.2004.08.021*.

[154] G. Okuma, J. Gonzalez-Julian, O. Guillon, and F. Wakai. "Comparison between sinter forging and X-ray microtomography methods for determining sintering stress and bulk viscosity". In: *Journal of the European Ceramic Society* 38.4 (2018), pp. 2053–2058. DOI: *10.1016/j.jeurceramsoc.2017.12.028*.

[155] C.B. Carter and M.G. Norton. "Sintering and Grain Growth". In: *Ceramic Materials: Science and Engineering*. New York, NY: Springer New York, 2013, pp. 439–456. ISBN: 978-1-4614-3523-5. DOI: *10.1007/978-1-4614-3523-5_24*.

[156] P.Z. Cai, G.L. Messing, and D.J. Green. "Determination of the Mechanical Response of Sintering Compacts by Cyclic Loading Dilatometry". In: *Journal of the American Ceramic Society* 80.2 (1997), pp. 445–452. DOI: *10.1111/j.1151-2916.1997.tb02850.x*.

[157] S.H. Lee, G.L. Messing, and D. Green. "Bending Creep Test to Measure the Viscosity of Porous Materials during Sintering". In: *Journal of the American Ceramic Society* 86.6 (2003), pp. 877–882. DOI: *10.1111/j.1151-2916.2003.tb03391.x*.

[158] R. Zuo, E. Aulbach, and J. Rödel. "Experimental determination of sintering stresses and sintering viscosities". In: *Acta Materialia* 51.15 (2003), pp. 4563–4574. DOI: *10.1016/S1359-6454(03)00293-3*.

[159] O. Guillon, J. Rödel, and R.K. Bordia. "Effect of Green-State Processing on the Sintering Stress and Viscosity of Alumina Compacts". In: *Journal of the American Ceramic Society* 90.5 (2007), pp. 1637–1640. DOI: *10.1111/j.1551-2916.2007.01572.x*.

[160] J. Baber, A. Klimera, and F. Raether. "In situ measurement of dimensional changes and temperature fields during sintering with a novel thermooptical measuring device". In: *Journal of the European Ceramic Society* 27.2 (2007), pp. 701–705. DOI: *10.1016/j.jeurceramsoc.2006.04.043*.

[161] K. Zhang et al. "Numerical simulation and experimental measurement of pressureless sintering of stainless steel part printed by Binder Jetting Additive Manufacturing". In: *Additive Manufacturing* 47.3 (2021), p. 102330. DOI: *10.1016/j.addma.2021.102330*.

[162] A.C.F. Cocks. "Inelastic deformation of porous materials". In: *Journal of the Mechanics and Physics of Solids* 37.6 (1989), pp. 693–715. DOI: *10.1016/0022-5096(89)90014-8*.

[163] Z.Z. Du and A.C.F. Cocks. "Constitutive models for the sintering of ceramic components—I. Material models". In: *Acta Metallurgica et Materialia* 40.8 (1992), pp. 1969–1979. DOI: *10.1016/0956-7151(92)90183-F*.

[164] J.K. Mackenzie and R. Shuttleworth. "A phenomenological theory of sintering". In: *Proceedings of the Physical Society. Section B* 62.12 (1949), p. 833.

[165] J.M. Duva and P.D. Crow. "The densification of powders by power-law creep during hot isostatic pressing". In: *Acta Metallurgica et Materialia* 40.1 (1992), pp. 31–35. DOI: *10.1016/0956-7151(92)90196-L*.

[166] P. Sofronis and R.M. McMeeking. "Creep of Power-Law Material Containing Spherical Voids". In: *Journal of Applied Mechanics* 59.2S (1992), S88–S95. DOI: *10.1115/1.2899512*.

[167] D.S. Wilkinson and M.F. Ashby. "Pressure sintering by power law creep". In: *Acta Metallurgica* 23.11 (1975), pp. 1277–1285. DOI: *10.1016/0001-6160(75)90136-4*.

[168] R.M. McMeeking and L.T. Kuhn. "A diffusional creep law for powder compacts". In: *Acta Metallurgica et Materialia* 40.5 (1992), pp. 961–969. DOI: *10.1016/0956-7151(92)90073-N*.

[169] M.F. Ashby. "Hip 6.0 Background Reading And Operator Manual". In: *Engineering Department, Cambridge, UK* (1990).

[170] Y.S. Kwon, G. Son, J. Suh, and K.T. Kim. "Densification and Grain Growth of Porous Alumina Compacts". In: *Journal of the American Ceramic Society* 77.12 (1994), pp. 3137–3141. DOI: *10.1111/j.1151-2916.1994.tb04561.x*.

[171] P.P. Castañeda. “The effective mechanical properties of nonlinear isotropic composites”. In: *Journal of the Mechanics and Physics of Solids* 39.1 (1991), pp. 45–71. DOI: *10.1016/0022-5096(91)90030-R*.

[172] M.N. Rahaman, L.C. Jonghe, G.W. Scherer, and R.J. Brook. “Creep and Densification During Sintering of Glass Powder Compacts”. In: *Journal of the American Ceramic Society* 70.10 (1987), pp. 766–774. DOI: *10.1111/J.1151-2916.1987.TB04877.X*.

[173] V.V. Skorohod. “Rheological basis of the theory of sintering”. In: *Kiev: Naukova Dumka* (1972), p. 1972.

[174] K.R. Venkatachari and R. Raj. “Shear Deformation and Densification of Powder Compacts”. In: *Journal of the American Ceramic Society* 69.6 (1986), pp. 499–506. DOI: *10.1111/j.1151-2916.1986.tb07452.x*.

[175] A. Mohanram, G.L. Messing, and D.J. Green. “Measurement of Viscosity of Densifying Glass-Based Systems by Isothermal Cyclic Loading Dilatometry”. In: *Journal of the American Ceramic Society* 87.2 (2004), pp. 192–196. DOI: *10.1111/j.1551-2916.2004.00192.x*.

[176] J.B. Ollagnier, O. Guillon, and J. Rödel. “Viscosity of LTCC Determined by Discontinuous Sinter-Forging”. In: *International Journal of Applied Ceramic Technology* 3.6 (2006), pp. 437–441. DOI: *10.1111/j.1744-7402.2006.02112.x*.

[177] H. Riedel, V. Kozák, and J. Svoboda. “Densification and creep in the final stage of sintering”. In: *Acta Metallurgica et Materialia* 42.9 (1994), pp. 3093–3103. DOI: *10.1016/0956-7151(94)90407-3*.

[178] H. Riedel, H. Zipse, and J. Svoboda. “Equilibrium pore surfaces, sintering stresses and constitutive equations for the intermediate and late stages of sintering—II. Diffusional densification and creep”. In: *Acta Metallurgica et Materialia* 42.2 (1994), pp. 445–452. DOI: *10.1016/0956-7151(94)90499-5*.

[179] J. Svoboda and H. Riedel. “Pore-boundary interactions and evolution equations for the porosity and the grain size during sintering”. In: *Acta Metallurgica et Materialia* 40.11 (1992), pp. 2829–2840. DOI: *10.1016/0956-7151(92)90448-N*.

[180] P. Grootenhuis, R.W. Powell, and R.P. Tye. “Thermal and Electrical Conductivity of Porous Metals made by Powder Metallurgy Methods”. In: *Proceedings of the Physical Society. Section B* 65.7 (1952), pp. 502–511. DOI: *10.1088/0370-1301/65/7/305*.

[181] T.H. Bauer. “A general analytical approach toward the thermal conductivity of porous media”. In: *International Journal of Heat and Mass Transfer* 36.17 (1993), pp. 4181–4191. DOI: *10.1016/0017-9310(93)90080-P*.

[182] V.I. Kononenko, V.M. Baranovskii, and V.P. Dushchenko. “Thermal conductivity of porous sintered iron”. In: *Powder Metallurgy and Metal Ceramics* 7.3 (1968), pp. 175–177. DOI: *10.1007/BF00774147*.

[183] E.A. Olevsky and A. Molinari. “Instability of sintering of porous bodies”. In: *International Journal of Plasticity* 16.1 (2000), pp. 1–37. DOI: *10.1016/S0749-6419(99)00032-7*.

[184] D.S. Smith et al. “Thermal conductivity of porous materials”. In: *Journal of Materials Research* 28.17 (2013), pp. 2260–2272. DOI: *10.1557/jmr.2013.179*.

[185] D.Z. Sun and H. Riedel. “Prediction of shape distortions of hard metal parts by numerical simulation of pressing and sintering”. In: *Simulation of Materials Processing: Theory, Methods and Applications, Numiform* 95 (1995), pp. 881–886.

[186] T. Kraft. "Optimizing press tool shapes by numerical simulation of compaction and sintering application to a hard metal cutting insert". In: *Modelling and Simulation in Materials Science and Engineering* 11.3 (2003), pp. 381–400. DOI: *10.1088/0965-0393/11/3/310*.

[187] C. Hartmann, P. Lechner, B. Himmel, Y. Krieger, T.C. Lueth, and W. Volk. "Compensation for Geometrical Deviations in Additive Manufacturing". In: *Technologies* 7.4 (2019), p. 83. DOI: *10.3390/technologies7040083*.

[188] S. Sadeghi Borujeni, A. Shad, K. Abburi Venkata, N. Günther, and V. Ploshikhin. "Numerical simulation of shrinkage and deformation during sintering in metal binder jetting with experimental validation". In: *Materials & Design* 216.5 (2022), p. 110490. DOI: *10.1016/j.matdes.2022.110490*.

[189] I. Gibson, D. Rosen, and B. Stucker. "Binder Jetting". In: *Additive Manufacturing Technologies: 3D Printing, Rapid Prototyping, and Direct Digital Manufacturing*. New York, NY: Springer New York, 2015, pp. 205–218. ISBN: 978-1-4939-2113-3. DOI: *10.1007/978-1-4939-2113-3_8*.

[190] I. Cristofolini et al. "Design for Powder Metallurgy: Predicting Anisotropic Dimensional Change on Sintering of Real Parts". In: *International Journal of Precision Engineering and Manufacturing* 16.1 (2019), p. 27. DOI: *10.1007/s12541-019-00030-2*. (Date accessed: 03/11/2019).

[191] AMPOWER. *Design guideline for sinter-based Additive Manufacturing*. Ed. by AMPOWER. 2020. URL: *https://ampower.eu/insights/design-guideline-for-sinter-based-additive-manufacturing/* (date accessed: 02/23/2023).

[192] L.O. Grant, M.B. Alameen, J.R. Carazzone, C.F. Higgs III, and Z.C. Cordero. "Mitigating distortion during sintering of binder jet printed ceramics". In: *2018 International Solid Freeform Fabrication Symposium*. University of Texas at Austin. 2018.

[193] S. Ha, K. Ransikarbum, H. Han, D. Kwon, H. Kim, and N. Kim. "A dimensional compensation algorithm for vertical bending deformation of 3D printed parts in selective laser sintering". In: *Rapid Prototyping Journal* 24.6 (2018), pp. 955–963. DOI: *10.1108/RPJ-12-2016-0202*.

[194] S. Afazov et al. "A methodology for precision additive manufacturing through compensation". In: *Precision Engineering* 50.1 (2017), pp. 269–274. DOI: *10.1016/j.precisioneng.2017.05.014*.

[195] S. Afazov, W.A.D. Denmark, B. Lazaro Toralles, A. Holloway, and A. Yaghi. "Distortion prediction and compensation in selective laser melting". In: *Additive Manufacturing* 17.12 (2017), pp. 15–22. DOI: *10.1016/j.addma.2017.07.005*.

[196] A. Yaghi, S. Ayvar-Soberanis, S. Moturu, R. Bilkhu, and S. Afazov. "Design against distortion for additive manufacturing". In: *Additive Manufacturing* 27 (2019), pp. 224–235. DOI: *10.1016/j.addma.2019.03.010*.

[197] M. Biegler, B.A.M. Elsner, B. Graf, and M. Rethmeier. "Geometric distortion-compensation via transient numerical simulation for directed energy deposition additive manufacturing". In: *Science and Technology of Welding and Joining* 25.6 (2020), pp. 468–475. DOI: *10.1080/13621718.2020.1743927*.

[198] H. Danninger and C. Gierl-Mayer. "7 - Advanced powder metallurgy steel alloys". In: *Advances in Powder Metallurgy*. Ed. by I. Chang and Y. Zhao. Woodhead Publishing Series in Metals and Surface Engineering. Woodhead Publishing, 2013, pp. 149–201. ISBN: 978-0-85709-420-9. DOI: *10.1533/9780857098900.2.149*.

[199] D.F. Heaney. "2 - Designing for metal injection molding (MIM)". In: *Handbook of Metal Injection Molding*. Ed. by D.F. Heaney. Woodhead Publishing Series in Metals and Surface Engineering. Woodhead Publishing, 2012, pp. 29–49. ISBN: 978-0-85709-066-9. DOI: *10.1533/9780857096234.1.29*.

[200] H. Fayazfar et al. "A critical review of powder-based additive manufacturing of ferrous alloys: Process parameters, microstructure and mechanical properties". In: *Materials & Design* 144 (2018), pp. 98–128. DOI: *10.1016/j.matdes.2018.02.018*.

[201] S. Kuschmitz, D. Fuchs, and T. Vietor. "Customer Benefit Oriented Approach on the Application of Additive Manufacturing Potentials Based on Product Property Trade-Off's". In: *Innovative Product Development by Additive Manufacturing 2021*. Ed. by R. Lachmayer, B. Bode, and S. Kaierle. Cham: Springer International Publishing, 2023, pp. 305–317. ISBN: 978-3-031-05918-6.

[202] J.W. Oh, S. Nahm, B. Kim, and H. Choi. "Anisotropy in Green Body Bending Strength due to Additive Direction in the Binder-Jetting Additive Manufacturing Process". In: *Korean Journal of Metals and Materials* 57.4 (2019), pp. 227–235. DOI: *10.3365/KJMM.2019.57.4.227*.

[203] A. Cabo Rios, E. Hryha, E.A. Olevsky, and P. Harlin. "Sintering anisotropy of binder jetted 316L stainless steel: Part II – microstructure evolution during sintering". In: *Powder Metallurgy* 65.4 (2022), pp. 283–295. DOI: *10.1080/00325899.2021.2020486*.

[204] *ISO 13322-2:2006-11 Particle size analysis — Image analysis methods — Part 2: Dynamic image analysis methods*.

[205] Keyence Corp. *3D Scanner CMM Stage VL-550*. URL: *https://www.keyence.com/products/measure-sys/3d-scanner/vl/models/vl-550/* (date accessed: 06/04/2023).

[206] Keyence Corp. *Digital Microscope VHX-5000*. URL: *https://www.keyence.com/products/microscope/digital-microscope/vhx-5000/models/vhx-5000/* (date accessed: 06/04/2023).

[207] Linseis Messgeräte GmbH. *DIL L75 PT Horizontal*. URL: *https://www.linseis.com/en/products/dilatometer/dil-l75-pt-horizontal/* (date accessed: 06/04/2023).

[208] Netzsch GmbH. *DSC404C Pegasus calorimeter*. URL: *https://analyzing-testing.netzsch.com/_Resources/Persistent/6/7/b/f/67bfbf591e8508902a8a5d76b3027b72121498c5/Key_Technical_Data_en_DSC_404_F1_F3_Pegasus.pdf* (date accessed: 06/04/2023).

[209] Netzsch GmbH. *LFA 427 Laser Flash Apparatus*. URL: *https://analyzing-testing.netzsch.com/_Resources/Persistent/5/a/8/5/5a85f97292e2aba6c44ce01e8e786e322d64dc37/Technical_Specifications_en_LFA_427.pdf* (date accessed: 06/04/2023).

[210] HP Inc. *HP Metal Jet technology: HP's digital printing technology for metals. Technical white paper*. 2018.

[211] *DIN EN 10088-1: Nichtrostende Stähle - Teil 1: Verzeichnis der nichtrostenden Stähle; Deutsche Fassung EN 10088-1:2014*.

[212] Nabertherm. *Thermprozesstechnik II: Öfen und Wärmebehandlungsanlagen für Prozesse unter Schutzgasen, Reaktionsgasen oder im Vakuum*. 2021. URL: *https://nabertherm.com/sites/default/files/2021-01/thermalprocesstechnology2_german.pdf* (date accessed: 12/04/2022).

[213] T. Apel, U. Langer, A. Meyer, and O. Steinbach. *Advanced Finite Element Methods with Applications*. Vol. 128. Cham: Springer International Publishing, 2019. ISBN: 978-3-030-14243-8. DOI: *10.1007/978-3-030-14244-5*.

[214] M.S. Shunmugam and M. Kanthababu. *Advances in Simulation, Product Design and Development*. Singapore: Springer Singapore, 2020. ISBN: 978-981-32-9486-8. DOI: *10.1007/978-981-32-9487-5*.

[215] M. Trunec and J. Cihlář. "Thermal debinding of injection moulded ceramics". In: *Journal of the European Ceramic Society* 17.2-3 (1997), pp. 203–209. DOI: *10.1016/S0955-2219(96)00108-2*.

[216] A. Bandyopadhyay, S.C. Danforth, and A. Safari. "Effects of processing history on thermal debinding". In: *Journal of Materials Science* 35.16 (2000), pp. 3983–3988. DOI: *10.1023/A:1004865716615*.

[217] F.P. Beer, E.R. Johnston, and J.T. DeWolf. *Mechanics of materials*. 2nd ed. in SI units. 1992. ISBN: 0-07-112939-1.

[218] G. K. Meenashisundaram, Z. Xu, M.L.S. Nai, S. Lu, J.S. Ten, and J. Wei. "Binder Jetting Additive Manufacturing of High Porosity 316L Stainless Steel Metal Foams". In: *Materials* 13.17 (2020). DOI: *10.3390/ma13173744*.

[219] S. Sadeghi Borujeni, A. Rütjes, and A. Shad. "Verfahren und Einrichtung zur generativen Herstellung eines Bauteils, sowie Kraftfahrzeug". DE102020213285A1. 2022.

[220] ASM Handbook Committee. *Fractography*. ASM International, 1987. ISBN: 978-1-62708-181-8. DOI: *10.31399/asm.hb.v12.9781627081818*.

[221] E. Dudrova and M. Kabátova. "A review of failure of sintered steels: Fractography of static and dynamic crack nucleation, coalescence, growth and propagation". In: *Powder Metallurgy* 59.2 (2016), pp. 148–167. DOI: *10.1080/00325899.2016.1145786*.

[222] A.D. Zwiren and T.F. Murphy. "Comparison of SS-316L PM Material Processed via Binder Jetting with SS-316L Powder processed by Pressing and Sintering". In: *International Journal of Powder Metallurgy* 54.4 (2018), pp. 39–50.

[223] Y. Xiong et al. "Data-Driven Design Space Exploration and Exploitation for Design for Additive Manufacturing". In: *Journal of Mechanical Design* 141.10 (2019), p. 225. DOI: *10.1115/1.4043587*.

[224] G. Liu, Y. Xiong, and D.W. Rosen. "Multidisciplinary design optimization in design for additive manufacturing". In: *Journal of Computational Design and Engineering* 9.1 (2022), pp. 128–143. DOI: *10.1093/jcde/qwab073*.

[225] F.M. Alam, K.R. McNaught, and T.J. Ringrose. "Using Morris' Randomized Oat Design as a Factor Screening Method for Developing Simulation Metamodels". In: *Proceedings of the 2004 Winter Simulation Conference, 2004*. IEEE, 2004, pp. 930–938. ISBN: 0-7803-8786-4. DOI: *10.1109/WSC.2004.1371413*.

[226] M.D. Morris. "Factorial Sampling Plans for Preliminary Computational Experiments". In: *Technometrics* 33.2 (1991), p. 161. DOI: *10.2307/1269043*.

[227] Dassault Systemes Simulia Corporation. *Abaqus 6.14 Documentation*. Dassault Systemes Simulia Corporation, 2014.

[228] Dassault Systemes Simulia Corporation. *ABAQUS/Standard*. Dassault Systemes Simulia Corporation, 2020.

[229] D. Sarkar, R. Bali, and T. Sharma. *Practical machine learning with Python: A Problem-Solver's Guide to Building Real-World Intelligent Systems*. Berkeley, CA: Apress, 2018. ISBN: 978-1-4842-3207-1. DOI: *10.1007/978-1-4842-3207-1*.

[230] P. Virtanen et al. "SciPy 1.0: fundamental algorithms for scientific computing in Python". In: *Nature methods* 17.3 (2020), pp. 261–272. DOI: *10.1038/s41592-019-0686-2*.

[231] E04 Committee. *Test Methods for Determining Average Grain Size*. West Conshohocken, PA, 2010. DOI: *10.1520/E0112-10*.

[232] F.G. Raether. "Current state of in situ measuring methods for the control of firing processes". In: *Journal of the American Ceramic Society* 92.s1 (2009), pp. 146–152. DOI: *10.1111/j.1551-2916.2008.02683.x*.

[233] ISO 2738:1999. *Sintermetalle, ausgenommen Hartmetalle / durchlässige Sintermetalle / Sintermetalle, ausgenommen Hartmetalle - Durchlässige Sintermetalle - Bestimmung der Dichte, des Tränkstoffgehaltes und der offenen Porosität (ISO 2738:1999)*. 2000-02. DOI: *10.31030/8529066*.

[234] MSC. Software Corporation. *MSC. Marc® and Mentat® 2014.2 User's Guide*. MSC. Software Corporation. 2014.

[235] MSC. Software Corporation. *MSC. Marc® and Mentat® 2014.2 Volume D: User Subroutines and Special Routines*. MSC. Software Corporation. 2014.

[236] A. Shad, R. Stache, and A. Rütjes. "Effects of fumed silica flow aids on flowability and packing of metal powders used in Binder-Jetting additive manufacturing process". In: *Materials & Design* 212.11 (2021), p. 110253. DOI: *10.1016/j.matdes.2021.110253*.

[237] I.M. Sobol. "Sensitivity analysis for non-linear mathematical models". In: *Mathematical modelling and computational experiment* 1 (1993), pp. 407–417.

[238] N. Stander et al. *LS OPT: A design optimization and probabilistic analysis tool for the engineering analyst*. 2019.

[239] P. Virtanen et al. "SciPy 1.0: Fundamental Algorithms for Scientific Computing in Python". In: *Nature Methods* 17 (2020), pp. 261–272. DOI: *10.1038/s41592-019-0686-2*.

[240] M. Cima, M. Oliveira, H.R. Wang, E. Sachs, and R. Holman. "Slurry-Based 3DP and Fine Ceramic Components". In: *Proceedings of Solid Freeform Fabrication Symposium, Austin, TX, USA* (2001).

[241] S. Stopp, T. Wolff, F. Irlinger, and T. Lueth. "A new method for printer calibration and contour accuracy manufacturing with 3D–print technology". In: *Rapid Prototyping Journal* 14.3 (2008), pp. 167–172. DOI: *10.1108/13552540810878030*.

[242] H. Miyanaji, M. Orth, J.M. Akbar, and L. Yang. "Process development for green part printing using binder jetting additive manufacturing". In: *Frontiers of Mechanical Engineering* 13.4 (2018), pp. 504–512. DOI: *10.1007/s11465-018-0508-8*.

[243] S. Timoshenko. *Strength of materials*. 3rd ed. Malabar, Fla.: Krieger Pub. Co, 1983. ISBN: 978-0898746211.

[244] C. Bient, K.L. Lencoski, D.F. Heaney, and R.M. German. "Modeling of distortion after densification during liquid-phase sintering". In: *Metallurgical and Materials Transactions A* 35.12 (2004), pp. 3833–3841. DOI: *10.1007/s11661-004-0289-z*.

[245] S. Nosewicz, J. Rojek, and M. Chmielewski. "Discrete Element Framework for Determination of Sintering and Postsintering Residual Stresses of Particle Reinforced Composites". In: *Materials* 13.18 (2020). DOI: *10.3390/ma13184015*.

[246] A.S. Glassner. *An introduction to ray tracing*. Morgan Kaufmann, 1989.

[247] P. Shirley and R.K. Morley. *Realistic ray tracing*. AK Peters, Ltd, 2008.

[248] T. Möller. "A Fast Triangle-Triangle Intersection Test". In: *Journal of Graphics Tools* 2.2 (1997), pp. 25–30. DOI: *10.1080/10867651.1997.10487472*.

[249] T. Möller and B. Trumbore. “Fast, minimum storage ray/triangle intersection”. In: *ACM SIGGRAPH 2005 Courses on - SIGGRAPH ’05*. Ed. by J. Fujii. New York, New York, USA: ACM Press, 2005, p. 7. DOI: *10.1145/1198555.1198746*.

[250] A. Lagae and P. Dutré. “An Efficient Ray-Quadrilateral Intersection Test”. In: *Journal of Graphics Tools* 10.4 (2011), pp. 23–32. DOI: *10.1080/2151237X.2005.10129208*.

[251] *DIN EN ISO 286-1: 2019-09, Geometrische Produktspezifikation (GPS) -ISO-Toleranzsystem für Längenmaße- Teil 1: Grundlagen für Toleranzen, Abmaße und Passungen (ISO 286-1:2010 + Cor 1:2013); Deutsche Fassung EN ISO 286-1:2010 + AC:2013*. Berlin, 2019. DOI: *10.31030/3056514*.

[252] M. Galati and P. Minetola. “Analysis of Density, Roughness, and Accuracy of the Atomic Diffusion Additive Manufacturing (ADAM) Process for Metal Parts”. In: *Materials* 12.24 (2019). DOI: *10.3390/ma12244122*.

[253] P. Minetola, M. Galati, F. Calignano, L. Iuliano, G. Rizza, and L. Fontana. “Comparison of dimensional tolerance grades for metal AM processes”. In: *Procedia CIRP* 88 (2020), pp. 399–404. DOI: *10.1016/j.procir.2020.05.069*.

[254] GKN Additive. *Metal Binder Jetting (MBJ): From detailed features to massive structures*. URL: *https://www.forecast3d.com/wp-content/uploads/2023/02/GKN-AM-F3D-SaleSheet-MBJ_02072023vX.pdf* (date accessed: 06/14/2023).

[255] LECO. *Leco C Analysator C744*. 2022. URL: *https://eu.leco.com/product/744-series* (date accessed: 12/31/2022).

Additional References

The current work includes results that are studied in the following master thesis, supervised by the author:

H. Lin. "Failure Prediction during Debinding/Sintering in Metal Binder Jetting Using Data-Driven Numerical Simulations". Master thesis. Bochum: Ruhr University Bochum, 2022.

Publications of the Author

S. Sadeghi Borujeni, G.S. Saluja, and V. Ploshikhin. “Compensation of sintering deformation for components manufactured by metal binder jetting using numerical simulations”. In: Rapid Prototyping Journal 29.3 (2023), pp. 612–625. ISSN:1355-2546. DOI: 10.1108/RPJ-06-2022-0181.

S. Sadeghi Borujeni, A. Shad, K.A. Venkata, N. Günther, and V. Ploshikhin. “Numerical simulation of shrinkage and deformation during sintering in metal binder jetting with experimental validation”. In: Materials & Design 216.5 (2022), p. 110490. ISSN: 02641275. DOI: 10.1016/j.matdes.2022.110490.

List of Figures

List of Tables

Appendices

A Appendix A

To monitor the deflection behavior in the graphite-chamber furnace with H_2, the manufactured green part is heated up to 1400 °C with a 5 K/ min heating rate. Unexpectedly, it was observed at 1380 °C that the arms of the sample melted onto the base, as shown in Fig. A.1.

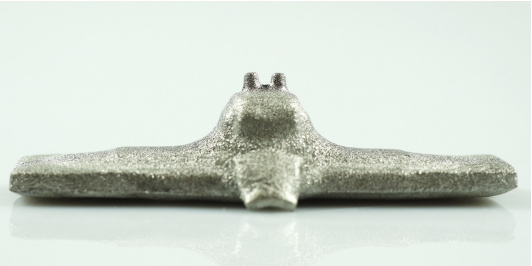

Figure A.1 The melted cross-shape geometry in the graphite-chamber furnace.

To investigate the reason, the carbon content of the sample is analyzed with a C-LECO C Analysator C744 manufactured by LECO Corporation [255]. It is found that the carbon content increased to 1.27 %, which differs significantly from the carbon content of the parts sintered in the workshop furnaces (0.0262 %). Consequently, it can be inferred that the material properties, including the melting temperature [45, 46], differ from that of the sintered SS316L in the workshop furnace. The graphite-chamber furnace appears to react with the sample at higher temperatures.

B Appendix B

The TEC values of cycles 2-7 are shown in Fig. B.2.

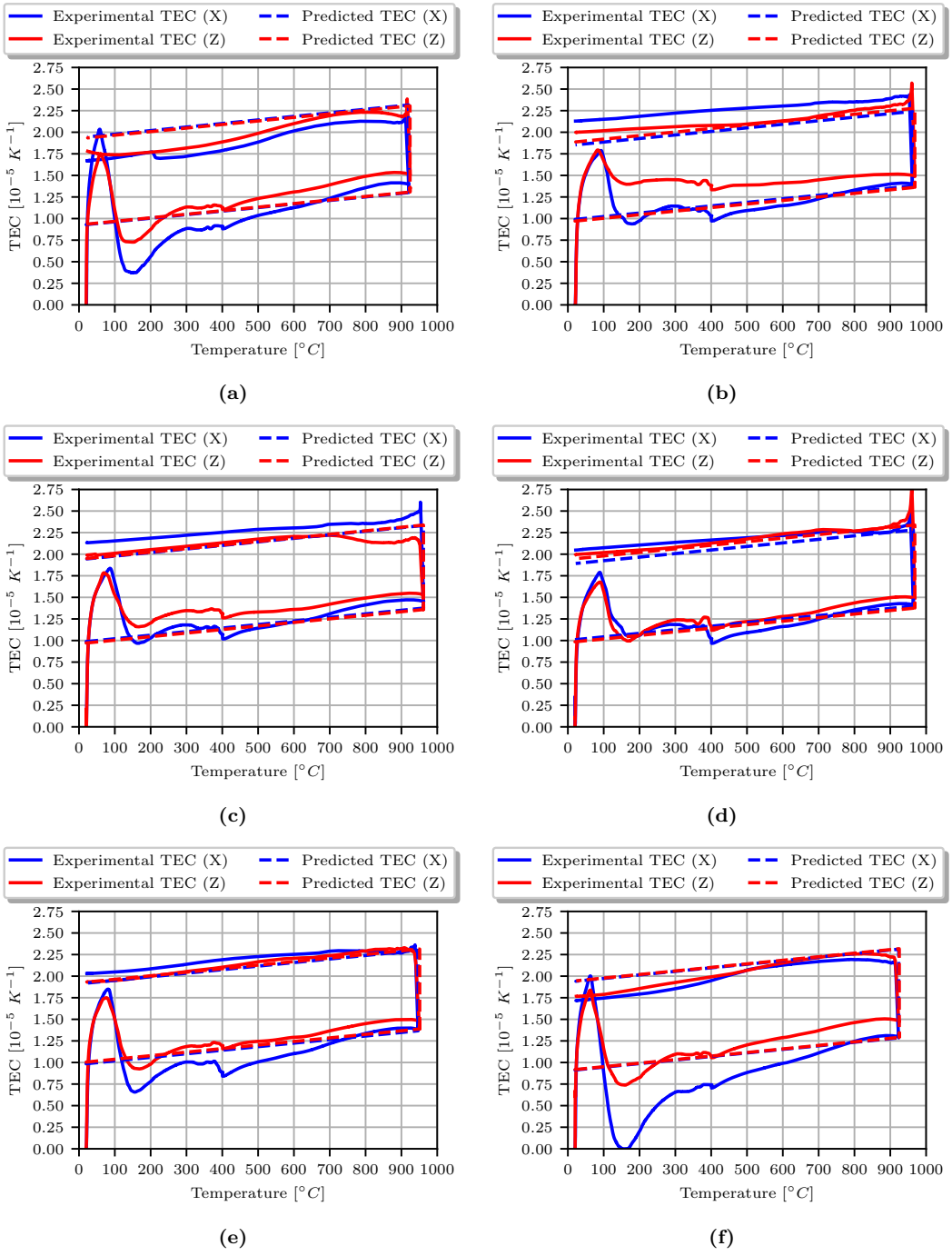

Figure B.2 The instantaneous and predicted TEC values for X and Z specimens sintered with (a): cycle-2, (b): cycle-3, (c): cycle-4, (d): cycle-5, (e): cycle-6, and (f): cycle-7.